

DESIGN, FABRICATION, AND CHARACTERIZATION OF LAMINATED  
HYDROXYAPATITE-POLYSULFONE COMPOSITES

By

CLIFFORD ADAMS WILSON II

A DISSERTATION PRESENTED TO THE GRADUATE SCHOOL  
OF THE UNIVERSITY OF FLORIDA IN PARTIAL FULFILLMENT  
OF THE REQUIREMENTS FOR THE DEGREE OF  
DOCTOR OF PHILOSOPHY

UNIVERSITY OF FLORIDA

2005

Copyright 2005

By

Clifford Adams Wilson II

To my wife, Leslie, and my parents, Cliff and Marilyn, for your love and encouragement  
throughout this entire process

## ACKNOWLEDGMENTS

I would especially like to thank Dr. John Mecholsky Jr. for his guidance and for always having his door open for students.

I would also like to thank the other members of my supervisory committee, Dr. Anthony Brennan, Dr. Kenneth Anusavice, Dr. Wolfgang Sigmund, and Dr. Bhavani Sankar, for their input and advice, which helped guide me through this project.

I need to acknowledge the contributions to this work made by Leslie Wilson, of the Department of Materials Science and Engineering, who prepared the initial PSu solutions used for solvent casting, Dr. Sukjoo Choi of the Department of Mechanical and Aerospace Engineering, who performed the finite element analysis presented in this study, and Gil Brubaker of the Particle Engineering Research Center, who performed the particle size analysis.

I want to thank Allyson Barrett and Ben Lee of the Department of Dental Biomaterials for their assistance. Finally, I would like to thank the all other graduate students who helped made coming to lab everyday a pleasure, but especially, Dr. Tom Hill, and Dr. Alvaro Della Bona who helped to become acclimated when I first arrived at the University of Florida.

## TABLE OF CONTENTS

	<u>Page</u>
ACKNOWLEDGMENTS .....	iv
LIST OF TABLES .....	viii
LIST OF FIGURES .....	x
ABSTRACT .....	xviii
CHAPTERS	
1 BACKGROUND AND RATIONALE.....	1
Requirements for an Ideal Hard Tissue Regeneration Device.....	1
Materials Selection .....	4
Research Rationale and Objective.....	10
2 HYDROXYAPATITE.....	12
Background on Processing of Hydroxyapatite .....	12
Starting Materials.....	13
Processing Methods.....	13
Tape Casting .....	13
Cold Pressing.....	14
Organic Burnout and Densification .....	14
Sintering.....	17
Specimen Refinement.....	18
HA Characterization Methods.....	18
Particle Size Analysis .....	18
X-Ray Diffraction.....	18
Density and Porosity.....	18
Elastic Modulus and Poisson's Ratio.....	19
Optical Microscopy and Lighting Effects.....	20
Scanning Electron Microscopy.....	20
Mechanical Testing Methods.....	20
Establishing Baseline Properties for Monolithic Hydroxyapatite .....	20
Indentation .....	21
Biaxial Flexure.....	22
Work of Fracture and Toughness.....	22
Fracture Toughness.....	23

Finite Element Analysis.....	25
Statistical Analysis.....	26
Results and Discussion.....	26
Starting Powder Characterization.....	26
Development of a Tape Casting Method for Hydroxylapatite.....	28
Burnout and Sintering Process.....	35
Characterization and Mechanical Properties of Post-Burnout Hydroxyapatite.....	36
Problems with Specimens Fired to 1000°C.....	38
Mechanical Properties of 1000°C Specimens.....	38
Constant Fracture Toughness.....	41
Firing Study.....	43
Sintering Temperature Effect on Hardness.....	44
Sintering Temperature Effect on Biaxial Flexure Strength.....	44
Sintering Temperature Effect on Density.....	44
Qualitative Determination of Hydroxyapatite Decomposition.....	46
Sintering Temperature Selection.....	47
Optimization of Sintering.....	48
Density and Elastic Modulus of 1200°C Specimens.....	49
Hardness of 1200°C Specimens.....	51
Biaxial Flexure Strength of 1200°C Specimens.....	52
Work of Fracture and Toughness.....	53
Fracture Toughness of 1200°C Specimens.....	54
Monolithic Hydroxyapatite Specimens.....	55
 3 LAMINATE FABRICATION.....	 59
Design and Nomenclature.....	59
Laminate Design.....	59
Laminate Geometry and Nomenclature.....	59
Solvent Casting of Polysulfone.....	60
Materials.....	61
Methods.....	62
Solvent Casting of Polysulfone.....	62
Specimen Preparation.....	64
Characterization of PSu Films and Laminates.....	71
Results and Discussion.....	72
Problems With the Solvent Casting Methods.....	72
Thermal Analysis of Polysulfone Layers.....	79
 4 LAMINATE THEORY.....	 91
Background.....	91
Methods.....	92
Laminate Theory.....	92
Finite Element Analysis (FEA).....	95
Material Modeling Parameters.....	95
Results and Discussion.....	97

Comparison of FEA and Laminate Theory Models .....	97
Predicting Laminate Behavior .....	102
5 LAMINATE BEHAVIOR .....	111
Methods .....	111
Mechanical Testing and Characterization of Laminates .....	111
Laminate Testing Variables .....	112
Results and Discussion .....	114
Comparison of Laminates to Monoliths .....	114
Testing of Laminate Parameters .....	118
Determination of Failure Mechanisms .....	135
Fracture Analysis of 400-200-800 Laminates .....	139
Failure Mechanism of Laminates with Outer HA Layers < 400 $\mu\text{m}$ .....	155
6 CONCLUSIONS .....	162
LIST OF REFERENCES .....	170
BIOGRAPHICAL SKETCH .....	175

## LIST OF TABLES

<u>Table</u>	<u>Page</u>
2.1 Mechanical data and fractography measurements for HA specimens fired to 1000°C .....	42
2.2 Biaxial flexure strength data for specimens sintered at 1200°C.....	52
2.3 Work of fracture values for specimens sintered at 1200°C.....	54
2.4 Fracture toughness values for 1200°C hydroxyapatite specimens .....	55
3.1 Hardness of laminates made through the matching halves method.....	76
3.2 Weight percent solvent retained results for PSu layers fabricated at all three drying temperatures. ....	79
3.3 Comparison of laminates fabricated with polymer layers composed of both PSu and sPSu .....	90
4.1 Initial comparison of laminate models to FEA for monolithic HA. ....	98
4.2 Comparison of corrected laminate models to FEA for monolithic HA.....	98
4.3 Comparison of maximum principal stress calculated through FEA and Laminate Theory for various laminate geometries. ....	99
4.4 Contact stress field radii for each laminate geometry that yields the same results as the FEA .....	100
4.5 Maximum stresses on the tensile surface of each layer for all laminate geometries experimentally tested in this study. ....	106
5.1 Comparison of the average mechanical property values for the monolithic HA versus the 400-200-800 laminates.....	116
5.2 Hardness data for initial flaw size laminates. ....	118
5.3 Mechanical property data versus indent loads.....	119
5.4 Hardness data for the laminates with different PSu layer thicknesses.....	122

5.5	Apparent toughness values versus increasing PSu layer thicknesses .....	125
5.6	Hardness data for laminates with different outer HA layer thicknesses. ....	127
5.7	Apparent fracture toughness comparison for different outer HA layers.....	131
5.8	Hardness data for the four laminate groups prepared with thicker middle HA layers. ....	131
5.9	Comparison of flaw sizes for monolithic HA and the outer HA layer for 400-200-800 laminates.....	139
5.10	Middle HA layer failure stress calculations for the 400-200-800 laminates. ....	144
5.11	Failure stress calculations for laminates with outer HA layers < 400 $\mu\text{m}$ .....	161

## LIST OF FIGURES

<u>Figure</u>	<u>Page</u>
1.1 A plot of fracture toughness versus Young's modulus of biomaterials being developed for bone replacement adapted from Suchanek and Yoshimura [6].	6
2.1 Weight % of each constituent in the tape casting slurry.	15
2.2 Green tape processing, shown are punched green discs (top left), the 25 mm (1") knife edge punch (middle), and scrap tape (top right). The section of tape processed (bottom) is 30 cm (12") x 11 cm (4.5") and produced 36 green discs.	15
2.3 Organic burnout cycle performed on the consolidated discs produced by cold pressing hydroxyapatite green tape.	16
2.4 Oblique allowed surface features to be seen (bottom) in greater detail than with overhead lighting (top).	21
2.5 Schematic representation of fracture markings that result from a brittle fracture adapted from Mecholsky, et al [53].	24
2.6 Particle size distribution for the starting hydroxylapatite powder.	26
2.7 XRD spectrum for the as-received hydroxylapatite powder.	27
2.8 Effects of applied pressure (top) and hold time (bottom) on the reduction in thickness of stacked green tapes during cold pressing.	31
2.9 Optical micrographs of post-cold pressing edge delamination (top left), delamination at the center (bottom left), full consolidation (top right), and post-sintering center delamination.	32
2.10 The reduction in thickness of the stacked green tapes is plotted versus wt% binder in the tape casting slurries (top), and binder:plasticizer ratio (bottom).	34
2.11 TG/DTA data curves for a pre-burnout green tape sample (top) and a post-burnout hydroxyapatite specimen.	37

2.12	XRD spectrum for HA specimens burned out at 1000°C (top) and specimens sintered at 1200°C (bottom) .....	39
2.13	XRD spectrum for HA specimen fired to 1200°C (top) and for naturally occurring HA (bottom) [8]. Circles (●) indicate peaks found on both spectra, the square (■) indicates the peak that is unique to the 1200°C spectrum.....	40
2.14	Optical micrographs of a Vickers indent for a 1000°C specimen (left) and crack propagation through a Vickers indent. ....	42
2.15	Log-log plot of failure stress versus indent load for HA specimens fired to 1000°C .....	43
2.16	A plot of hardness versus sintering temperature for the hydroxyapatite specimens. ....	45
2.17	A plot of failure stress versus sintering temperature for the hydroxyapatite specimens.....	45
2.18	Plot of density versus sintering temperature for hydroxyapatite specimens.....	46
2.19	Color comparison of specimens sintered at five different temperatures. Each row of specimens was fired at the temperature indicated to the right. ....	47
2.20	Plot of failure stress versus hold times at 1200°C .....	50
2.21	Plot of failure stress versus ramp rate sintering temperature of 1200°C. ....	50
2.22	SEM micrograph of the microstructure of the hydroxyapatite specimens sintered at 1200°C.....	51
2.23	Comparison of stress-strain curves for indented and non-indented HA specimens.....	53
2.24	All specimens tested in biaxial flexure fractured into either two (left) or three (right) pieces. ....	54
2.25	Plot of $K_C$ versus $K_{SI}$ for the hydroxyapatite specimens sintered at 1200°C.....	56
2.26	SEM micrograph of the initial flaw caused by an indent (black bar) for a 1200°C HA specimen. The outer boundary of the initial flaw (white arrows) and a twist-hackle marking (black arrow) are shown.....	56
2.27	Optical micrographs of an entire fracture surface (top) and initial flaw (bottom) of a 1200°C specimen indented with a 3.35 kg indent. The white arrows indicate the outer edge of the critical flaw.....	57
3.1	Schematic diagram of HA/PSu laminate .....	60

3.2	Polysulfone .....	61
3.3	Sulfonated Polysulfone .....	62
3.4	Step-by-step schematic of laminate fabrication method 1: The Matching Halves Method .....	68
3.5	Step-by-step schematic of laminate fabrication method 2: The Bottom Up Method .....	69
3.6	Step-by-step schematic of laminate fabrication method 3: The Pre-Fabricated PSu Layer Method .....	70
3.7	Optical micrographs of (left) a large surface bubble formed during laminate fabrication, and (right) a small bubble (black arrow) within a PSu layer that caused a HA layer to fracture (white arrows). .....	73
3.8	Left: Optical micrograph of a PSu layer that peeled from the HA disc during drying. Right: Higher magnification image of the PSu layer (white arrow) that peeled due to fracture of the HA layer (black arrows) which is still bonded to the PSu layer. ....	73
3.9	Optical micrographs of a large hole that formed during indentation (left), and of a laminate with a defective PSu layer containing a large open cavity (right) .....	76
3.10	SEM image of bubbles (black arrows) which formed during laminate fabrication using the bottom up technique.....	77
3.11	Schematic drawing of chipping failures that occur when fabricating thick PSu layers through the bottom up method.....	78
3.12	Complete TG curve for an as received PSu pellet.....	81
3.13	A comparison of TG curves PSu films dried at the three different temperatures.....	81
3.14	TG curves for six different PSu films dried at 70°C.....	82
3.15	TG curve for a PSu sample taken from a delaminated region of a laminate fracture surface.....	82
3.16	DSC curves generated through three heating-cooling cycles for an as received PSu pellet.....	85
3.17	DSC curves generated through three heating-cooling cycles for a PSu film dried at 70°C. ....	85
3.18	A plot of elastic modulus vs. drying temperature for PSu layers. ....	86

3.19	A plot of break stress vs. drying temperature for PSu layers.....	86
3.20	A plot of elongation at break vs. drying temperature for the PSu layers.....	87
3.21	A plot of failure loads and stresses vs. laminate fabrication method and drying temperature. Units of the y-axis are different for each series.....	87
3.22	A plot of laminate failure loads and stresses vs. surface polishing medium. The ordinate axis has units are unique to each series plotted. ....	89
4.1	A schematic representation of a laminate indicating the mathematical variables required for laminate theory calculations. ....	93
4.2	The Microsoft Excel spreadsheet designed to calculate the laminate stress distribution for the 400-200-800 laminate .....	96
4.3	Graphical representation of the stress field resulting from a 1 N applied load on a 400-400-800 HA/PSu laminate. ....	97
4.4	Stress distribution calculated using laminate theory resulting from a 1N load applied to a 400-200-800 laminate. Laminate layers are drawn to scale, with the 2.00 thickness representing the outer HA layer tensile surface. ....	102
4.5	Maximum stresses for the 400-200-800 laminate as (a) a plot of individual points and (b) a graphed smoothed curve. ....	104
4.6	Maximum stress curves for laminates as a function of varying polymer layer thickness.....	107
4.7	Maximum stress curves for laminates as a function of varying outer HA layer thickness.....	107
4.8	Maximum stress curves for laminates as a function of varying middle HA layer thickness.....	108
4.9	Maximum stress curves for various laminate geometries having a total laminate thickness of 2.0 mm. ....	108
4.10	A plot of maximum tensile stress values versus the ratio between the thicknesses of the outer HA and PSu layers. ....	109
4.11	A plot of maximum tensile stress versus the ratio of thicknesses between the PSu and middle HA layers.....	109
4.12	A plot of maximum tensile stress versus the ratio of thickness between the outer and middle HA layers. ....	110

5.1	Comparison of load displacement curves for the 400-200-800 laminates compared with monolithic HA.....	116
5.2	Comparison of mechanical properties measured for monolithic HA as the 400-200-800 laminates. The units of the ordinate axis vary for each property listed with units designated in the column headings. ....	117
5.3	Comparison of failure stress for 400-200-800 laminates versus both indented and non-indented monolithic HA specimens. ....	117
5.4	Lateral cracking seen during indentation using a 9.35 kg load (left), and the resulting chip-out that occurs during loading (right). ....	119
5.5	A plot of failure stress versus loading rate.....	121
5.6	A plot of absorbed energy at failure (toughness) versus loading rate for 400-200-800 laminates.....	121
5.7	A plot of failure loads versus PSu layer thickness. Monolithic HA failure load is plotted as a PSu layer thickness of 0. ....	123
5.8	A plot of failure stress vs. PSu layer thickness. Monolithic HA is plotted as a PSu thickness of 0.....	124
5.9	A plot of stress vs. outer HA/PSu layer thickness ratio for a comparison of experimental values to laminate theory predictions.....	124
5.10	A plot of work of fracture vs. PSu layer thickness .....	125
5.11	A plot of absorbed energy at fracture (toughness) vs. PSu layer thickness.....	126
5.12	A plot of failure loads versus outer HA layer thickness. The total thickness of the specimens is shown in parenthesis.....	128
5.13	A plot of failure stresses versus outer HA layer thickness. Monolithic HA is plotted as a 2000 $\mu\text{m}$ thick HA layer.....	129
5.14	A plot of work of fracture versus outer HA layer thickness. ....	130
5.15	A plot of toughness versus outer HA thickness.....	130
5.16	Failure loads for laminates with thicker middle HA layers. ....	134
5.17	Failure stresses for laminates with thicker middle HA layers .....	134
5.18	Experimental failure loads for all the laminate geometries having a total laminate thickness of 2.0 mm .....	135

5.19	An optical micrograph of 400-200-800 laminate fracture surface. The locations of the initial indent flaw (white arrow), middle layer flaw (black arrow), and loading piston contact are all indicated. ....	136
5.20	Optical micrographs of a laminate still intact after being loaded to failure in biaxial flexure. Left: Failure occurred from the initial indent (indicated by the arrows) in the outer HA surface, Right: Examination of the edge of the specimen shows failure of the outer HA layer, delamination along the interface, and failure of the middle HA layer. ....	137
5.21	SEM image of punch through failure of a 400-400-800 laminate. The remnants of the indented outer HA layer are indicted by the black arrows, failure of the PSu layer were the loading piston breached all five layers is indicated by the white arrow. ....	138
5.22	Optical micrograph of the initial flaw size (black arrows) produced by a 3.35 kg indent (white arrow) in a 400-50-800 laminate ....	140
5.23	SEM image of the initial flaw produced in a 400-100-800 laminate produced by a 3.35 kg indent load. ....	140
5.24	Load-displacement curves for two non-indented laminates. Outer HA layer failure loads are calculated either from the initial drop (top) or by extrapolating the initial slope (dashed line) and estimating when the slope change begins (bottom). ....	142
5.25	Failure stresses of the outer HA layer calculated for three different initial flaw sizes. ....	143
5.26	Failure stresses of the outer HA a layer for laminates built with different PSu layer thicknesses. ....	143
5.27	Optical micrograph of the fracture oringin of a 400-200-800 laminate. The center of the flaw is indicated by the white arrow. ....	145
5.28	Optical micrograph of a middle layer fracture origin a 400-100-800 laminate. The specimen has been sputter coated to make the surface marking stand out. ....	145
5.29	SEM image of the middle HA layer fracture origin ....	146
5.30	SEM image of a 400-100-800 laminate showing contact damage (white arrows) from the loading piston which occurred <b>prior</b> to propagation of the primary fracture (black arrows) which was reinitiated near the HA/PSu interface (dashed arrow). ....	148
5.31	Optical micrograph of secondary cracks (arrows) which occurred through punch failure after primary failure from bending. ....	148

5.32	Optical micrograph of a PSu layer of a 400-200-800 laminate fractured at a crosshead displacement rate of 0.25 mm/min. The specimen was sputter coated prior to analysis. ....	149
5.33	Optical micrograph of a PSu layer of a 400-200-800 laminate fractured at a crosshead displacement rate of 25 mm/min. ....	149
5.34	Optical micrographs of the PSu layer features through overhead (top) and oblique lighting (bottom) .....	150
5.35	SEM images of brittle failure of the PSu layer, the pore (indicated by the arrow in the left image) shows a twist hackle marking (arrow in the right image) characteristic of brittle fracture.....	150
5.36	SEM image of ductile deformation of the PSu layer prior to failure at the center of the feature (black arrow).....	151
5.37	SEM image of two side-by-side features within the PSu layer that failed in different manners, a twist hackle marking (solid arrow) indicates the left feature failed in a brittle manner, while the pullout deformation (dashed arrow) of the right feature indicates ductile failure. ....	151
5.38	Optical micrograph of a sPSu/HA laminate showing the depth of penetration of the casting solution during solvent casting.....	154
5.39	SEM images showing the penetration depth of PSu into the middle HA layer. The fracture surface is shown top left, the box indicates the area where the top right picture was taken, the bottom picture showing PSu pullout was taken from the area indicated by the box in the top right image. ....	156
5.40	SEM images of PSu bridging of small cracks in the HA layers. These images were taken of the secondary interface crack shown in Figure 5.31.....	157
5.41	SEM images showing PSu bridging of the HA/PSu interface. PSu fibrils are indicated by the arrow.....	157
5.42	SEM image of PSu bridging of the HA/PSu interface.....	158
5.43	Optical micrographs showing the pullout of the PSu layers during fracture of the laminates. ....	158
5.44	SEM images of brittle PSu layer originating from the HA/PSu interface. The arrow indicates the location of the origin. ....	159
5.45	SEM images of a PSu layer fracture origin. The location of the origin is indicated by the arrows on both images, failure occurred within the PSu layer and not from the interface. ....	159

5.46	Optical micrograph of the fracture origin (solid white arrows) of a 100-100-1600 laminate, the large damaged area is caused by the indent (dashed arrow).....	161
6.1	Addition of the HA/PSu laminates designed in this study to the graph of available biomaterials for bone replacement developed by Suchanek and Yoshimura [6].....	163

Abstract of Dissertation Presented to the Graduate School  
of the University of Florida in Partial Fulfillment of the  
Requirements for the Degree of Doctor of Philosophy

DESIGN, FABRICATION, AND CHARACTERIZATION OF LAMINATED  
HYDROXYAPATITE-POLYSULFONE COMPOSITES

By

Clifford Adams Wilson II

August 2005

Chair: John J. Mecholsky Jr.

Major Department: Materials Science and Engineering

There exists a need to develop devices that can be used to replace hard tissues, such as bone, in load-bearing areas of the body. An ideal hard tissue replacement device is one that stimulates growth of natural tissues, and is slowly resorbed by the body. The implant is also required to have elastic modulus, strength, and toughness values similar to the tissues being replaced.

Hydroxyapatite (HA) is the primary mineral phase of bone and has the potential for use in biomedical applications because it stimulates cell growth and is resorbable. Unfortunately, HA is a relatively low strength, low toughness material, which limits its application to only low load-bearing regions of the body. In order to apply HA to greater load-bearing areas of the body, strength and toughness must be improved through the formation of a composite structure.

The goal of this study to show that a composite structure formed from HA and a biocompatible polymer can be fabricated with strength and toughness values that are

within the range necessary for load-bearing biomedical applications. Therefore, Polysulfone-HA composites were developed and tested. Polysulfone (PSu) is a hard, glassy polymer that has been shown to be biocompatible. Composites were fabricated through a combination of tape casting, solvent casting, and lamination. Monolithic HA and laminate specimens were tested in biaxial flexure. A unique laminate theory solution was developed to characterize stress distributions for laminates. Failure loads, failure stress, work of fracture, and apparent toughness were compared for the laminates against monolithic HA specimens.

Initial testing results showed that laminates had a failure stress of  $60 \pm 10$ , which is a 170% improvement over the  $22 \pm 2$  MPa failure stress for monolithic HA. The work of fracture was improved by 5500% from  $11 \pm 2$  for the monolithic HA to  $612 \pm 240$  for the laminates. Work of fracture values gave the laminates an apparent fracture toughness of  $7.2 \text{ MPa}\cdot\text{m}^{1/2}$  compared to  $0.6 \text{ MPa}\cdot\text{m}^{1/2}$  for the monolithic HA.

Laminates with different geometries were built and tested in an attempt to optimize the strength and toughness of the composites. Laminate behavior was characterized as a function of initial flaw size, HA layer thickness, PSu layer thickness, and stressing rate. The failure stress of the laminates was maximized at a value of  $108 \pm 14$  MPa, which is a 400% improvement over monolithic HA, and close to the 120 – 160 MPa range reported for bone. The work of fracture of laminates was maximized at  $724 \pm 206 \text{ J/m}^2$ , which is a 6400% improvement over monolithic HA, and yields an apparent fracture toughness value of  $7.5 \text{ MPa}\cdot\text{m}^{1/2}$ . This apparent toughness value is within the 2-12  $\text{MPa}\cdot\text{m}^{1/2}$  range for bone, and an 1100% improvement over the fracture toughness of monolithic HA.

## CHAPTER 1 BACKGROUND AND RATIONALE

### **Requirements for an Ideal Hard Tissue Regeneration Device**

#### **Tissue Response to Implanted Materials**

Any material implanted in the body will illicit a response from the surrounding tissues. Bioceramics, when implanted in the body will elicit one of four potential tissue responses [8]. If the material is toxic, the surrounding tissues will die. If the material is nontoxic and biologically inactive, the body will surround the material with a fibrous capsule but not experience any negative consequences due to the presence of the implanted materials. A material that elicits this type of tissue response is called biocompatible.

A third tissue response occurs when an implanted material is nontoxic and biologically active. These materials are called bioactive because they form an interfacial bond with surrounding tissues. The final tissue response occurs when a nontoxic implanted material dissolves in the body. These materials are called bioresorbable [8].

#### **Definition of the Gold Standard**

In order for successful use of a material or composite for hard tissue regeneration, the material or composite must fulfill some basic requirements. These requirements are not explicit rules that govern research and development; rather they are ideals that have been set for the eventual gold standard. Through the study of hard tissues and hard tissue replacements by Hench [1-3], Bonfield [4], and others [5-7], the gold standard has been defined as a material, which will possess a few basic traits. The ideal hard tissue implant

must be biocompatible, bioactive, and mechanically identical to the tissue being replaced. Additionally, the ideal hard tissue replacement would be resorbed and replaced by the surrounding natural tissue.

### **Biocompatibility**

Biocompatibility will be defined as the ability of a material to perform a desired function in the body without causing any adverse effect upon natural tissue with which it comes into contact [8]. A material is required that will not cause any type of inflammatory or destructive response in the body. No matter how well a material performs the required mechanical functions, if there is an adverse response to the material within the body, the material is unacceptable for use. Biocompatibility is the greatest limiting factor in biomaterial design. If the entire spectrum of known materials was available for use, artificial bones and hard tissues replacement devices would probably already exist. However, materials that are toxic or reactive in the natural environment (for example, corrosion of metals over time when implanted in the body) cannot be used due to adverse effects on surrounding tissues. Therefore, research is limited to materials that are biocompatible.

Biocompatible materials currently used for biomedical applications include metals, such as titanium, stainless steel and cobalt chromium, bioinert ceramics, such as alumina, zirconia, calcium phosphates and inorganic glasses, and a polymers like polymethyl methacrylate (PMMA), polyethylene (PE) , polylactic acid (PLA), and polysulfone (PSu) [8]. These are just a few examples of biocompatible materials used in the body and should not be considered a comprehensive list since new materials are continually being developed and approved for use in the body.

### **Bioactivity and Bioresorbtion**

Bioactivity refers to the ability of a material to promote regeneration of the natural tissues [9]. Regeneration is favored over replacement due to the long-term degradation of replacement materials, which causes a need for repetitive procedures over the life of a patient. Another reason for bioactivity is that it can be a useful tool in the implantation of a hard tissue device. The conclusion on the biochemical reactions occurring at the tissue/implant interface of research by Hench [1-3] and Suchanek [6] is that activation of natural tissue generation and the subsequent growth in and around the implant will aid in anchoring the implant into place. Furthermore, if bioactive materials are broken down by the surrounding environment, the body may then resorb it. Bioresorbable materials are designed to degrade gradually over a period of time, and be replaced by the natural host tissue [1]. There is a very narrow range of materials that are both biocompatible, bioactive, and bioresorbable and can be used for hard tissue replacement. This range of materials is currently limited to bioceramics such as calcium phosphates and bioactive glasses [2].

### **Matching Mechanical Properties**

The third major requirement of these materials is that they have mechanical properties that are similar to those of the natural tissue in which they are in contact. Problems arise from stress shielding when there is a mismatch in properties from one material to the next [8]. For example, replacing bone with a higher modulus material leads to a lower strength healed bone around the implant due to the implant carrying more of the load than the surrounding bone. Since bone remodeling is a continuous process that the body uses it to adapt to changes in stresses. For example, if a normally,

inactive person were to start exercising on a regular basis, the body would remodel bones to compensate for the greater stresses felt during exercise. In the case of a higher modulus material being implanted to replace bone, the body would lay down weaker bone in the areas surrounding a higher modulus implant because the implant would bear most of the applied loads.

There is also a need for implanted materials to have toughness values greater than those of the surrounding tissues, such that mechanical failures will not occur within the implanted materials before they occur in the surrounding tissue. A failure of the implant would lead to increased loading of the weakened, surrounding tissue and compound the problems that are being resolved.

## **Materials Selection**

### **Hydroxyapatite**

Tissue regeneration is the most limiting factor in materials selection as there are few materials capable of inducing bone growth. One of the better-studied materials is hydroxyapatite (HA). Hydroxyapatite is the primary inorganic component of all calcified tissues existing in the human body [8].

Synthetic HA powders can be prepared in a number of different ways. Processes like sol-gel [6], precipitation [10], and solid-state reactions [11] have all been used to produce HA powder. HA powder fabrication is a common process such that HA is readily available through a number of commercial supply companies. Numerous studies have shown that synthetic HA is bioactive and can be used as a bone replacement [1, 6].

HA containing a Ca:P ratio of 1.67 is bioactive [2, 6] and theoretically can be used for bone tissue replacement. Unfortunately, characterization of synthetically made HA shows that it has mechanical properties that are inferior to the necessary properties to sustain load-bearing applications in the body. Dense forms of HA have been fabricated, and a wide range of mechanical data have been reported. Bending strengths from 38-250 MPa, tensile strengths from 38-300 MPa, and fracture toughness values in the range of 0.8-1.2 MPa•m<sup>1/2</sup> have been reported [6]. Young's Modulus values have been reported in the range of 10-30 GPa [5, 6]. Porous versions of HA have mechanical properties that are much lower [12, 13]. Bending and tensile strengths for these materials have been reported in range of 2-11 MPa and around 3 MPa, respectively [6]. Fracture toughness values have been shown to decrease with increasing porosity [13]. These materials are capable of matching the bending and tensile strengths of compact human bone, which have been reported to be as great as 160 MPa and 124-170 MPa, respectively [6]. However, the fracture toughness of HA is well below that reported for compact bone, which is in the range of 2-12 MPa•m<sup>1/2</sup> [1, 13] HA, on its own, lacks adequate mechanical properties to be applied to major load bearing applications.

### **HA Composites**

Since monolithic HA lacks mechanical properties sufficient to withstand load-bearing applications within the body, HA must be combined into composite structures with other materials in order to meet the load-bearing requirements for bone replacement. The goal of forming the composite is to increase both the strength and toughness of HA to levels more consistent with that of natural bone.

HA was been formed into a composite with titanium, zirconia, and alumina [6], as well as being reinforced through the addition of particles [14], whiskers [15], and fibers [6]. All of these materials have significant limitations, which limit their usefulness. The greatest problem is the modulus mismatch with bone. Figure 1.1, recreated from literature [6], shows the relationship of the mechanical properties of these materials to the mechanical properties of dense HA and to bone. Clearly these materials will need to be further refined for use as a hard tissue replacement.

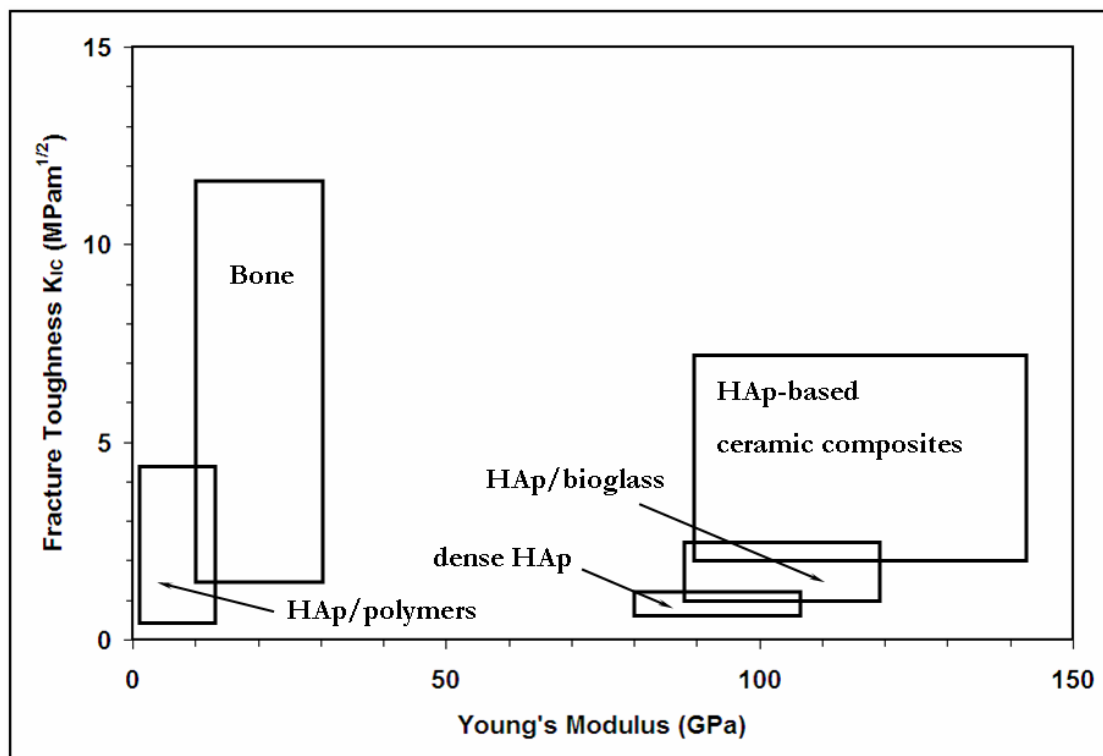


Figure 1.1 A plot of fracture toughness versus Young's modulus of biomaterials being developed for bone replacement adapted from Suchanek and Yoshimura [6].

The only other materials incorporated with HA to form composite materials with modulus and toughness values similar to bone are polymers. A few of the polymers that have been incorporated successfully into the HA matrix include polyethylene, poly(L-

lactide), polysulfone as well as some biopolymers such as collagen [6, 8, 9]. Bonfield and his group have reported extensive work on PE/HA composites [4, 16-18].

HAPEX™ is an HA/PE composite that is FDA approved for use in the inner ear. HAPEX™ and other HA/polymer composites are produced by adding HA as the reinforcement to the polymers. HA/PE composites have an elastic modulus in the range of 1-8 GPa [6] and fracture toughness values that overlap that of bone, see Figure 1.1. Since polymers cannot withstand the temperature required to strengthen HA through sintering, HA/polymer composites are confined to forming through addition of HA particles into the polymer matrix. The resulting composites have greatly improved toughness values over monolithic HA but the high polymer content lowers the strength below that required for load-bearing applications. Clearly, another composite structure composed of HA and polymer is required.

### **Biological Structures**

Fabrication of strong, tough materials has already been achieved many times over. Nature, in many ways, has taken materials that on their own might seem useless and combined them to create structures with extraordinary mechanical properties. Structures like mollusk shells [19], arthropod cuticles [20], and bone [5] are fabricated starting at the atomic level and built up to the macroscopic level. There are orientations within orientations, and levels of organization within level of organization. While science cannot yet make these materials on the same molecular size scale as nature, the development of materials on the nanometer scale may lead to the development of biomaterials that closely mimic mechanical structures found in nature.

Nature produces strong composites through the incorporation of polymers in the form of proteins into composite structure with ordinarily brittle materials. Much research is being done to develop materials, which mimic the structure and behavior of natural materials [21]. Work has been done with conch shells [19], which are composed of  $\text{CaCO}_3$ , and proteins, have strength and toughness values that are orders of magnitude greater than monolithic  $\text{CaCO}_3$ . Conch shell achieves its superior strength, and toughness through a hierarchical structure composed of a macroscopic three layer laminate structure, with each layer having a second and third order hierarchy.

Bone itself is composed of a complex hierarchical structure [5] that could be compared to a laminate with a thin cortical bone layer at the outer surface, and spongy trabecular bone in the middle. Bone consists of collagen molecules mineralized with hydroxyapatite crystals, which are grouped into fibrils, which are grouped into fibers, which then form lamellar structures called osteons. Osteons align themselves parallel to the long axis of bones. Looking at each osteon as an individual layer, bone can be described as a laminate structure. While it is not currently plausible to build composites with the same degree of sophistication as conch shell and bone, it is possible to incorporate the premise of a laminate composite.

### **Laminate Composites**

Lamination is an effective method of combining materials into composite structures. Common ways of creating laminate structures are pressing at room or elevated temperatures, using an adhesive to bond the lamina together or combining materials that are mutually reactive to form chemical bonds. The resulting composites

will have laminas joined either by a chemical bond or by a mechanical interlocking of the lamina surfaces.

Past studies deal with combining ductile and brittle materials together through lamination [22-24]. It has been shown that through the lamination of brittle ceramics with ductile metals the toughness of the brittle ceramic can be increased [22, 25]. Some systems that have been developed with laminate structures are Bioglass/Copper [22], and Alumina/Nickel [24].

The mechanical properties of laminates are directly determined by the interface that is formed between the laminated materials [25]. If there is a weak interface between the constituents of the ductile-brittle laminate, then in the case of crack propagation, there will be evidence of delamination along the interface between the two materials. The result will be an unusable, low strength composite. A ductile-brittle laminate that has a strong interface will have a significant increase in toughness resulting from crack bridging or cracks arrest at the interface between the two materials.

### **Strength and Biocompatibility of Polysulfone**

Polysulfone (PSu) is a tough, thermoplastic. PSu is used extensively for engineering applications because it has good thermal stability with degradation temperatures in excess of 450°C. PSu has greater strength and elastic modulus than PE, which has facilitated research into replacing PE with PSu as the matrix material of HA/polymer particulate composites [9].

PSu films have been used as reinforcements of carbon-fiber-reinforced epoxies [26], as well as for filtration membranes. PSu films are made through solvent casting, or through phase inversion techniques.

Polysulfone has been shown to be biocompatible as it is used as for blood filtration membranes [8]. PSu has been combined with bioactive glasses for a bone fixation study [27] and with epoxy fibers implanted into rabbits [28]. Both studies demonstrated good long-term stability of the PSu composites *in vivo*. *In vitro* studies of polysulfone have show negligible cellular response to implanted polysulfone [52].

### **Research Rationale and Objective**

The goal of this study is to develop a composite structure composed of hydroxyapatite and polysulfone with modulus, strength, and toughness values similar to those reported for bone. Reaching this goal will require the achievement of three specific objectives.

The first objective is to design a fabrication technique for combining hydroxyapatite and polysulfone into a laminate structure. Achieving this objective requires first producing monolithic hydroxyapatite layers through a combination of tape casting, burnout, and sintering of a starting hydroxyapatite powder, followed by lamination with polysulfone through solvent casting, stacking, and lamination. Chapter 2 of this document covers development and optimization of a tape casting, burnout, and sintering methodology for hydroxyapatite, as well as characterization and mechanical testing of the monolithic HA. Chapter 3 covers procedures for fabrication of HA/PSu laminates, as well as characterization and optimization of these laminate fabrication procedures. Strength and toughness of the laminates will be characterized through loading in biaxial flexure, which leads to the second objective.

The second objective of this study is to derive a mathematical model for describing stresses resulting from applied loads during biaxial flexure of laminated circular discs. Such a solution exists to describe the flexural behavior of laminated beams, but not for

circular discs. The derivation will be validated through a comparison with finite element analysis of the HA/PSu laminates before being applied to calculation of laminate strengths. Derivation of the laminate theory solution, along with a comparison to finite element modeling is the subject of Chapter 4.

The final objective will be the characterization of the strength and toughness of the laminates. The strength and toughness will be tested as a function of flaw sizes and individual layer thicknesses. Fractography will be performed on fractured laminates to determine the failure mechanisms. The strength and toughness of the laminates will be compared with monolithic HA as well as to the reported values for bone to gauge the success of the project in terms of producing a composite with properties similar to bone. Mechanical testing data and failure analysis of the laminates is presented in Chapter 5.

## CHAPTER 2 HYDROXYAPATITE

### **Background on Processing of Hydroxyapatite**

A number of important factors must be taken into consideration when working with hydroxyapatite. The most important factor is the stoichiometric ratio of calcium to phosphorus. The correct Ca:P ratio for bioactive hydroxyapatite is 1.67:1 [2, 6]. Ratios less than 1.67 can lead to the formation of secondary calcium phosphate phases, while ratios exceeding 1.67 can lead to CaO formation [13]. The presence of CaO and Ca(OH)<sub>2</sub> leads to cracking during cooling due to differences in the coefficients of thermal contraction. There is also an accompanying decrease in mechanical strength.

Sintering temperatures for hydroxyapatite must be closely controlled because hydroxyapatite is susceptible to undergoing a decomposition reaction at temperature, which is only slightly higher than the sintering temperatures. Sintering temperatures for HA range from between 1000-1250°C [13]. Hydroxyapatite undergoes dehydroxylation at ~800°C, which leads to a deficiency of OH<sup>-</sup> ions within the crystal structure, which is remedied through rehydration during cooling. Hydroxyapatite is best sintered between 1000-1200°C to achieve the highest densities, with density and porosity being highly dependent upon starting particle sizes [13, 29, 30]. Decomposition of hydroxyapatite occurs at a temperature between 1250-1450°C and results predominantly in the formation of tricalcium phosphate (TCP), tetracalcium phosphates (TTCP), or calcium oxide (CaO) [13, 41]. A significant loss in strength accompanies the decomposition reaction.

## Starting Materials

All hydroxyapatite specimens used in this study were fabricated from the same commercially available hydroxylapatite (Alfa Aesar, Ward Hill, MA) starting powder. The MSDS accompanying the hydroxylapatite gives it a molecular formula of  $\text{Ca}_{10}(\text{PO}_4)_6(\text{OH})_2$  which is the same as naturally occurring hydroxyapatite. This powder was selected because the distributor advertises the powder as possessing the correct 1.67:1 ratio of Ca:P necessary for hydroxyapatite to be bioactive [3].

## Processing Methods

### Tape Casting

The starting hydroxylapatite powder was fabricated into green tape using an Incetek tape casting machine (Integrated Ceramic Technologies, Inc., San Marcos, CA). The composition of the tape casting slurries can be found in Figure 2.1. Slurries were combined into polypropylene bottles, beginning with the addition of the organic solvents. Three organic solvents make up the 35 wt% of the slurry: methyl ethyl ketone (MEK), toluene, and ethanol (EtOH). These are added in a ratio of 6.25:5.25:1. Plasticizer (Santicizer® S-160), dispersant (Blown Menhaden Fish Oil), organic solvents, and 10-15 alumina milling balls are combined all at once. The combination is swirled until the dispersant is completely suspended. Hydroxylapatite powder and binder (Butvar® B-98) are combined apart from the solvent mixture and then gradually added. The bottle containing all constituents was wrapped in paraffin wax to minimize solvent evaporation, and ball milled for a minimum of 12 h.

After ball milling, the slurries are immediately tape cast. Slurries were not filtered prior to casting because a skin forms rapidly once the slurries are removed from

the ball mill. Tape casting was performed at a speed of  $\sim 3.5$  m/min, the best possible speed of the tape caster, and at ambient conditions. The doctor blade was set at a height of 200  $\mu\text{m}$  above the moving tape. Cast tapes were allowed to dry inside the tape casting machine for a period of 1-2 h to ensure complete drying, although after 15-20 min tapes are no longer tacky, and can be handled. Dried tapes had a thickness of 100-150  $\mu\text{m}$ . After 1-2 h, the green tape is removed from the tape casting machine and processed in to specimens for testing.

### **Cold Pressing**

Green tapes are punched into discs using a 25mm diameter knife edge punch. 0.3 m (1 ft) of green tape yields 30-36 discs. Discs were stacked to a desired thickness and cold pressed in a graphite mold and die at a pressure of 3500 psi (24 MPa) using a hydraulic laboratory press (Model C, Fred S. Carver Inc., Menomonee Falls, Wis.). Pressure was applied in increments of 1000, 1000, 1500 psi, allowing the system to come to equilibrium after each pressure addition. Equilibrium was seen as being achieved once the applied pressure remained constant for a minimum of 30 seconds without any decrease in the pressure reading. Once the maximum pressure was applied, the system is allowed to come to a final equilibrium and held constant for 1 minute to ensure that equilibrium had been achieved.

### **Organic Burnout and Densification**

Thermal analysis was performed on green tape samples using thermogravimetric-differential thermal analysis (TG/DTA), (Seiko Systems, Model 302) in order to identify temperatures for removal of the organic constituents of tape casting slurries, Figure 2.3. Organic burnout was carried out in a muffle furnace (Model FA 1730, Thermolyne,

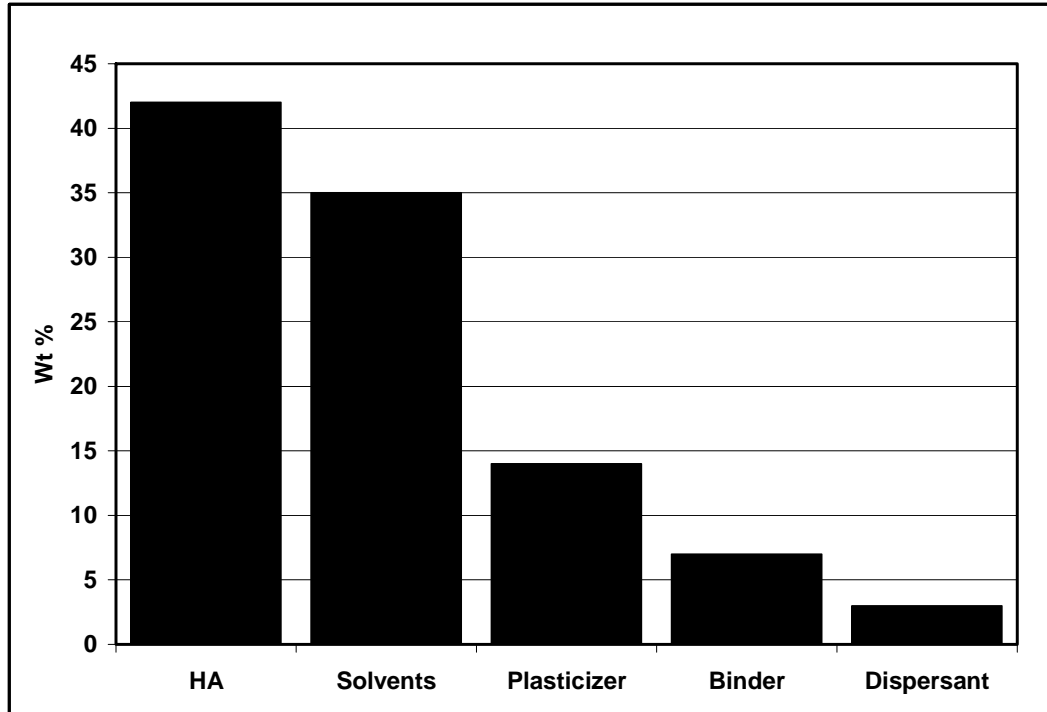


Figure 2.1 Weight % of each constituent in the tape casting slurry.



Figure 2.2 Green tape processing, shown are punched green discs (top left), the 25 mm (1") knife edge punch (middle), and scrap tape (top right). The section of tape processed (bottom) is 30 cm (12") x 11 cm (4.5") and produced 36 green discs.

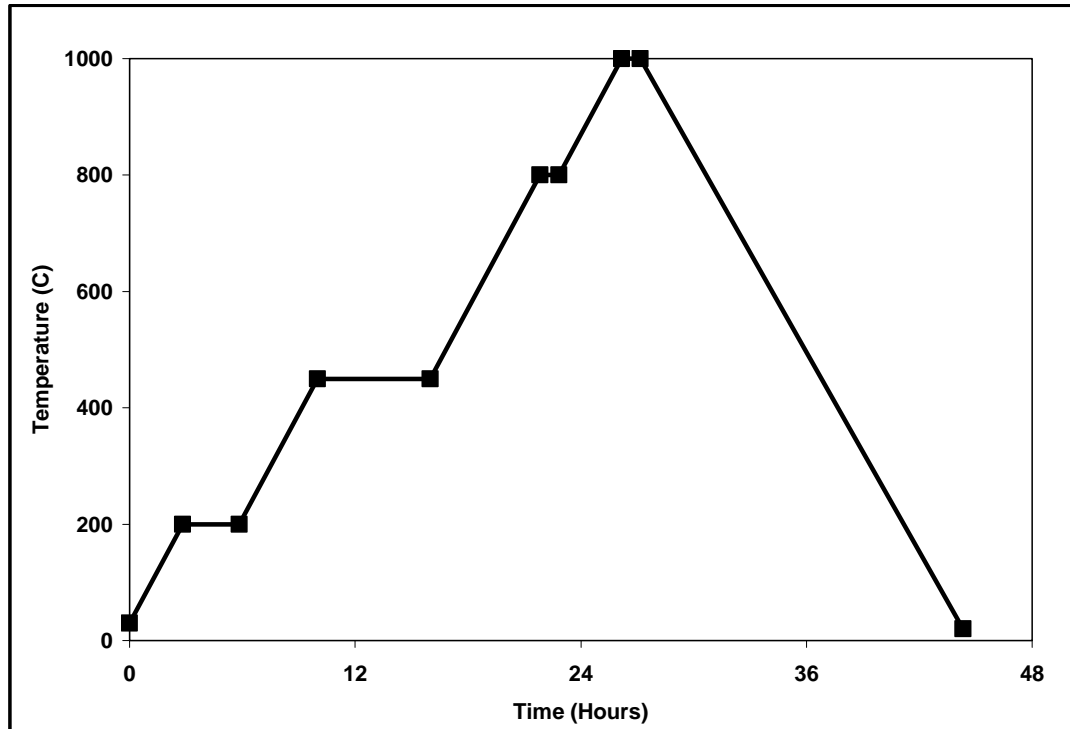


Figure 2.3 Organic burnout cycle performed on the consolidated discs produced by cold pressing hydroxyapatite green tape.

Dubuque, IA) with a programmable digital controller. The pressed hydroxylapatite discs were placed onto furnace plates that had been dusted with alumina powder to prevent any possible adhesion of the hydroxylapatite specimens to the furnace plates.

The rate of heating of  $1^{\circ}\text{C}/\text{min}$  was constant for all heating ramps, while the rate of furnace cooling was approximately  $0.5^{\circ}\text{C}/\text{min}$ . Removal of the organics occurs during the 3 h hold at  $200^{\circ}\text{C}$  and the 6 h hold at  $450^{\circ}\text{C}$ . The 1 h holds at  $800^{\circ}\text{C}$  and  $1000^{\circ}\text{C}$  are required for initial sintering of the hydroxyapatite in order to give the specimens enough mechanical strength to be handled for further processing. Specimens cooled from  $450^{\circ}\text{C}$ , and not fired through these upper two hold temperatures were too brittle to be handled.

## **Sintering**

After organic burnout, specimens were removed from the burnout furnace and placed in a second furnace. The second furnace was required since the burnout furnace was not capable of reaching the desired sintering temperatures. Specimens were placed in a drop down furnace (Del Tech Inc.). A short study was conducted to find the sintering temperature that produced hydroxyapatite specimens with the best combination of strength and processability. Seven specimen groups were sintered at temperatures of 1000°, 1050°, 1100°, 1150°, 1200°, 1250°, and 1300°C. The ramp rate of 5°C/min and hold time of 90 min were constant for each firing temperature.

The mechanical properties (flexural strength, hardness, fracture toughness) of the firing study specimens were characterized and compared for the seven sintering temperatures. The sintering temperature that yielded the best combination of strength and processability was 1200°C. To optimize the sintering process, testing was done on the effect of both the ramp rate and hold time of the sintering process. The effect of hold time was tested by sintering two specimen groups at 1200°C with different programmed hold times of 1 and 10 h, and using a constant ramp rate of 5°C/min. Three specimens groups were tested for the effect of ramp rate on mechanical properties. The three ramp rates tested were 1°, 5°, and 20°C/min to 1200°C with a constant hold time of 1 h.

The final sintering program consists of a ramp rate of 5°C/min with a hold time of 90 min at 1200°. This firing program was used to process all monolithic hydroxyapatite specimens as well as the hydroxyapatite specimens later used to fabricated composites.

The thickness of specimens was measured after sintering. The total reduction in thickness from the stacked green tapes was, on average, 55%.

## **Specimen Refinement**

The post-sintered specimens were polished by hand to a desired testing thickness using 45 and 15  $\mu\text{m}$  diamond polishing wheels. In some cases specimens were indented, these specimens were polished through the 15  $\mu\text{m}$  finish. Specimens that were not indented were further polished using 5, 3, and 1  $\mu\text{m}$  alumina pastes to remove as many large surface flaws as possible.

## **HA Characterization Methods**

### **Particle Size Analysis**

The particle size distribution and specific surface area of the starting hydroxylapatite powder was characterized using a laser diffraction particle size analyzer (Beckman Coulter, LS<sup>TM</sup> 13 320 series). Analysis was performed on the starting powder as it was delivered by the manufacturer.

### **X-Ray Diffraction**

X-ray diffraction (XRD) was performed using an APD 3720 automated powder diffractometer (Phillips Electronic Instrument, Inc., Mahwah, NJ). XRD was performed on the as delivered hydroxylapatite starting powder, post-organic burnout 1000°C sample, and post-sintering at 1200°C sample. Measurements were taken for a range of  $2\theta = 20^\circ$ - $70^\circ$ , with a step size of 0.05.

### **Density and Porosity**

The density of the monolithic hydroxyapatite specimens was measured using the Archimedes principle of volume displacement [31]. Specimens were dried at 150°C for 12 h and then weighed in air. Specimens were then placed in distilled water and placed in a vacuum chamber for 30 min to ensure saturation. Specimens were then weighed

both saturated,  $m_{sat}$  and suspended,  $m_{sus}$ . The density was then calculated by first calculating the volume of water displaced,  $V_{dis}$ , by the suspended specimen:

$$V_{dis} = \frac{(m_{sat} - m_{sus})}{\rho_{H_2O}} \quad (2.1)$$

where the density of water was assumed to be 1.0 g/cm<sup>3</sup>. The density of the HA specimens was then calculated through:

$$\rho_{HA} = \frac{m_{air}}{V_{dis}} \quad (2.2)$$

The total porosity of the specimens was then calculated through:

$$\%Porosity = \frac{V_{porosity}}{V_{total}} \quad (2.3)$$

where the pore volume is

$$V_{porosity} = \frac{(m_{sat} - m_{dry})}{\rho_{H_2O}} \quad (2.4)$$

and  $V_{total} = V_{porosity} + V_{specimen}$ .

### **Elastic Modulus and Poisson's Ratio**

The elastic modulus of the hydroxyapatite specimens was characterized using an ultrasonic technique [32]. The elastic modulus,  $E$ , was calculated from the equation:

$$E = \frac{3\rho V_p^s - 4\rho V_s^2}{(V_p / V_s)^2 - 1} \quad (2.5)$$

where  $\rho$  is the specimen density,  $V_p$  is the longitudinal wave velocity, and  $V_s$  is the shear wave velocity. Poisson's ratio,  $\nu$ , was then calculated from the equation [32]:

$$\nu = \frac{E}{2G} - 1 \quad (2.6)$$

where the shear modulus,  $G$ , is calculated from the equation [32]:

$$G = \rho V_s^2 \quad (2.7)$$

### **Optical Microscopy and Lighting Effects**

The majority of the fractography and other microscopic analysis were performed using optical microscopy on an Olympus optical microscope. This microscopy proved difficult at times due to the nature of the hydroxyapatite being analyzed. Hydroxyapatite is a white, polycrystalline material that reflects and absorbs light. The color of this material made it particularly difficult to see surface features necessary for fractographic measurements. Two methods were used to overcome these difficulties. The first was to sputter coat the specimens with Au-Pd alloy. This method was used primarily on the most difficult specimens since it requires both time and equipment that can be expensive to use. The second solution was to switch from using overhead lighting to oblique lighting. The oblique lighting caused surface features to stand out (Figure 2.4), and made analysis possible in a more cost effective manner.

### **Scanning Electron Microscopy**

Scanning Electron Microscopy (SEM) was used to characterize the microstructure of the hydroxyapatite, and to perform fractography on the fractured specimens. All SEM work was performed on a Joel 6400 scanning electron microscope.

## **Mechanical Testing Methods**

### **Establishing Baseline Properties for Monolithic Hydroxyapatite**

Strength tests were performed to establish the baseline properties of monolithic HA to compare with composite materials. Specimens were tested using a method of strength indentation in which specimens were first indented for hardness characterization, and then fractured in biaxial loading.



Figure 2.4 Oblique allowed surface features to be seen (bottom) in greater detail than with overhead lighting (top).

### **Indentation**

Monolithic hydroxyapatite specimens were indented with Vickers indentations. Indentation loads < 2 kg were applied using a Micromet3 microhardness tester (Buehler LTD, Lake Bluff, IL), loads > 2 kg were applied using an older indentation tester (Zwick Inc.) The hardness of the specimens was calculated using the equation:

$$H = 0.0018544 \left( \frac{P}{d^2} \right) \quad (2.8)$$

where P is the indent load in N, and d is the half diagonal length of the indent in mm [33].

### **Biaxial Flexure**

The monolithic hydroxyapatite specimens were loaded to failure in biaxial flexure using a piston on three-ball testing fixture. A loading piston with a diameter of 2.2 mm was selected for this study, and an effective ring radius produced by the three-ball support varied depending on the specimens being tested. Hydroxyapatite specimens fired to 1000°C were tested with a support diameter of 23.2 mm. Specimens fired to 1200°C had a small diameter due to shrinkage compared with the 1000°C samples and were instead tested with a support diameter of 15 mm.

The failure stress,  $\sigma_f$ , from bending in a piston and three-ball fixture can be calculated using the equation developed by Wachtman [34]:

$$\sigma_f = \frac{3P(1-\nu)}{4\pi t^2} \left[ 1 + 2 \ln \frac{a}{b} + \left( \frac{1-\nu}{1+\nu} \right) \left( 1 - \frac{b^2}{2a^2} \right) \frac{a^2}{R^2} \right] \quad (2.9)$$

Where  $P$  is the failure load,  $\nu$  is Poisson's ratio,  $t$  is the specimen thickness,  $a$  is the support ring radius,  $b$  is the loading piston radius, and  $R$  is the specimen radius.

Monolithic specimens were tested using a tensile testing machine (Instron) at a loading rate of 0.25 mm/min.

### **Work of Fracture and Toughness**

The toughness, or absorbed energy at fracture, of the monolithic specimens was calculated from the area under the stress-strain curves generated during loading in biaxial flexure [35]:

$$T = \int \sigma d\varepsilon \quad (2.10)$$

the stress,  $\sigma$ , was converted from the measured loads using equation 2.9, and the strain,  $\varepsilon$ ,

was calculated from the equation for elastic modulus,  $E=\sigma/\epsilon$ . The units for the toughness are  $J/m^3$ .

The work of fracture was calculated from the area under the load-displacement curves using the equation [36, 37]:

$$\gamma_{wof} = \frac{\int Pd\delta}{2A} \quad (2.11)$$

where  $P$  is the fracture load,  $\delta$  is the measured crosshead displacement, and  $A$  is the projected cross-sectional area of the created fracture surface. Work of fracture has units of  $J/m^2$ . Even though circular discs were fractured in biaxial flexure the cross-section of the fracture surface was assumed to be rectangular. The area of the fracture surface was dependent on the number of pieces created during the fracture process. Projected fracture surface areas were calculated by measuring the lengths of fractures and multiplied by the specimen thickness.

### **Fracture Toughness**

The fracture toughness,  $K_C$ , for the monolithic specimens was calculated using three different techniques. The first technique involved using the fracture mechanics equation [38]:

$$K_C = Y\sigma_f c^{1/2} \quad (2.12)$$

where  $\sigma_f$  is the failure stress calculated from equation 2.9,  $c$  is the critical flaw size, and  $Y$  is a geometric constant equal to 1.65 for indented specimens and 1.24 for nonindented specimens. The critical flaw size was measured using fractography and

$$c = (ab)^{1/2} \quad (2.13)$$

where  $a$  is the length of the semi-minor axis of the critical flaw, and  $2b$  is the length of

the semi-major axis, see Figure 2.5. Figure 2.5 is a schematic representation of fracture markings resulting from a brittle fracture process and is taken from Mecholsky, et al [53]. A detailed explanation of the different fracture markings can be found in this reference. Since HA is a polycrystalline ceramic it is difficult to distinguish many of these features. For this reason, only the size of the critical flaw was measured for fracture toughness calculations. The fracture markings that were measured are designated  $a_{cr}$  and  $b_{cr}$  in Figure 2.5.

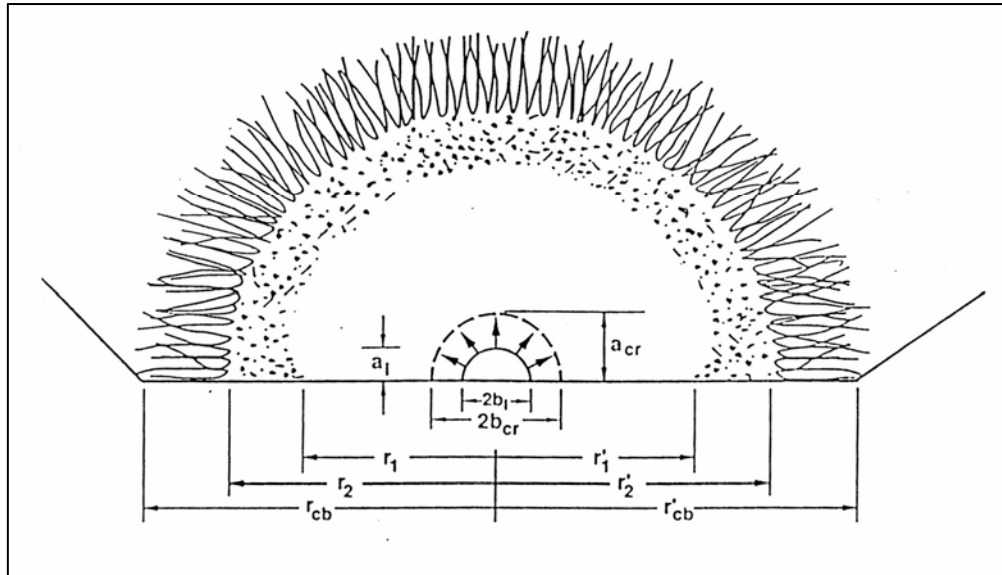


Figure 2.5 Schematic representation of fracture markings that result from a brittle fracture adapted from Mecholsky, et al [53].

The second method for calculating fracture toughness was through the strength indentation technique [39]. This technique calculates the fracture toughness using the equation:

$$K_{SI} = \eta_V^R \left( \frac{E}{H} \right)^{1/8} (\sigma_f P^{1/3})^{3/4} \quad (2.14)$$

where  $E$  is the elastic modulus of the specimen,  $H$  is the hardness,  $\sigma_f$  is the failure stress,  $P$  is the failure load, and  $\eta_v^R$  is a geometrical constant equal to  $0.59 \pm 0.12$ .

Anstis [40] demonstrated that the fracture toughness values  $K_C$  and  $K_{SI}$  should yield comparable results for brittle materials. The strength indentation technique was used to verify calculations using the fracture mechanics equation, which relies on measuring the critical flaw size, which in some cases proved difficult due to the fracture behavior of the hydroxyapatite and complexity of the observed cracks.

The strength indentation technique was also used to ensure that the fracture toughness was constant across a range of indent loads, and thus for different flaw sizes. A log-log graph of failure stress versus indent load should yield a straight line with a slope of  $-1/3$ . Deviation from the  $-1/3$  slope would demonstrate that fracture toughness is not constant for increasing flaw sizes and that phenomena such as microstructural effects or R-curve behavior was occurring. However, as will be demonstrated later in this chapter, fracture toughness values for HA were constant with increasing flaw size.

The third method used to calculate the fracture toughness from the work of fracture and elastic modulus using the relation [38]:

$$K_{Wof} = \sqrt{2E\gamma_{wof}} \quad (2.15)$$

### **Finite Element Analysis**

Finite element analysis was also performed to analyze the monolithic HA specimens. A detailed explanation of the analysis and the results are discussed in the Chapter 4.

## Statistical Analysis

All statistical analysis was performed using DOE Fusion Pro software. The software is running ANOVA statistics. All statistical analysis was run at  $\alpha = 0.05$ .

## Results and Discussion

### Starting Powder Characterization

The particle size distribution for the starting hydroxylapatite powder is shown in Figure 2.6. The starting hydroxylapatite powder shows a bimodal distribution. The use of a starting hydroxyapatite powder with a bimodal distribution has been reported previously [51] with the bimodal distribution attributed to the presence of large agglomerates. The starting powder was used in its as-received state and with no refinement to the particle size distribution. Since the goal of this study was to create a

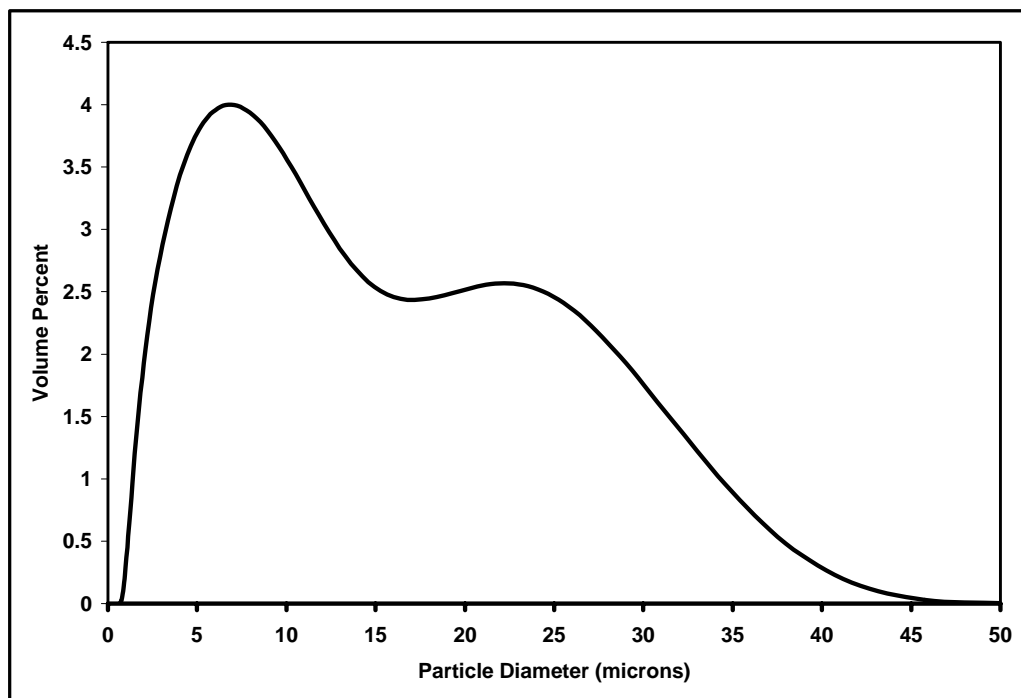


Figure 2.6 Particle size distribution for the starting hydroxylapatite powder

porous material that could allow cell infiltration, the particle size was left large in order to prevent packing during the processing steps. If the starting powder was refined to a smaller, more uniform particle size distribution the net result would be denser hydroxyapatite specimens. While the denser material would have increased flexural strength and toughness, the ideal result for this study would demonstrate that hydroxyapatite with a large amount of porosity can be fabricated to have mechanical properties within the range of bone.

XRD spectrum for the starting powder is shown in Figure 2.7. The spectrum shows a hydroxylapatite starting powder with low crystallinity, and is composed of mostly tri-calcium and tetra-calcium phosphate secondary phases.

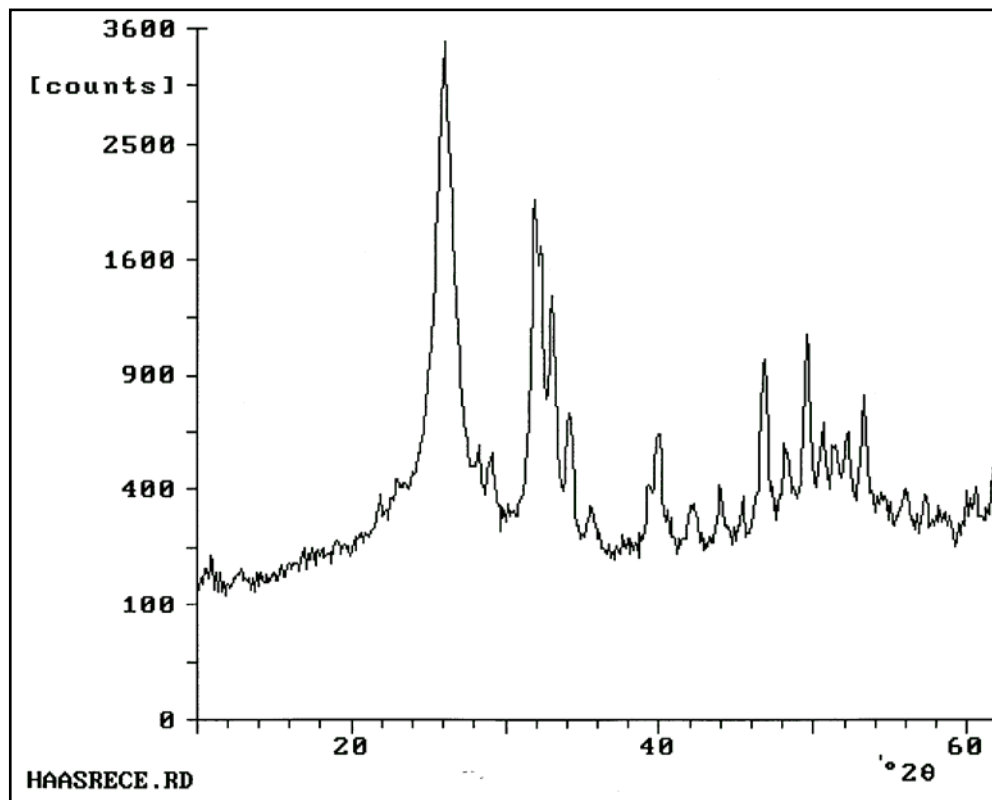


Figure 2.7 XRD spectrum for the as-received hydroxylapatite powder

### **Development of a Tape Casting Method for Hydroxylapatite**

Due to the large particle size distribution of the starting powder, and the type of tape casting machine being utilized developing a tape casting process for the hydroxylapatite proved a long and tedious trial and error process. The Incetek Model 104 tape caster has one exhaust port through which evaporating solvents are evacuated to a fume hood and a number of open seams around its doors and edges. These openings make it difficult to control airflow through the tape caster and thus the drying rate of the tape. Initial attempts were made to fabricate slurries with ethanol as the only organic solvent. However, the lower boiling point of ethanol ( $\sim 78^{\circ}\text{C}$ ) leads to a rapid evaporation rate and thus cracking of the green tape. To slow the evaporation rate, toluene was substituted for the ethanol since it has a higher boiling point of  $110^{\circ}\text{C}$ . The binder, B-98, is only partially soluble in toluene, which led to undissolved binder in the tape casting slurries and large tape defects upon drying. To remedy this problem MEK was added to aid in dissolving the binder. It has a boiling temperature ( $80^{\circ}\text{C}$ ) that is slightly higher than EtOH, which would also slow the drying process. The final slurry composition, which contains all three organic solvents, is a mixture which balances the need to dissolve the binder completely with evaporation rates that allow for drying of the green tape free of cracking due to overly rapid drying.

Once the drying problems were overcome, tapes were cast and consolidated through cold pressing. The two factors, which affected the cold pressing process, were applied pressure and hold time. A number of applied pressures (with a constant hold time) and hold times (with a constant applied pressure) were tested for their effect on the overall consolidation of the stacked green tapes during, Figure 2.8. Consolidation was

quantified by the measuring the percent reduction of total thickness of the stacked HA discs was reduced during cold pressing.

The consolidation of the stacked green tapes occurred through plastic deformation of the polymeric binder. This deformation determines the proximity of HA particles to each other. The organic tape casting constituents are removed during burnout leaving behind only the HA particles. With other factors such as phase structure, particle composition, wetting, and heating programs being constant, the particle spacing following cold pressing will control the final density of the HA specimens after sintering. As shown in Figure 2.8, it was found that the reduction in thickness of the stacked green tapes was not dependent upon either the applied pressure or the hold time. These results indicated that deformation of the binder occurs almost instantaneously upon the applied pressure reaching the threshold at which deformation occurs. The idea of the binder undergoing instantaneous deformation was supported by the equilibration of the applied pressure within a few seconds of the final pressure being applied and remaining constant for the duration of the hold time. Since the total amount of force applied by the press remains constant unless acted upon by an outside agent (i.e. additional ram strokes), a drop in the pressure of the system would indicate an increase in the area through plastic deformation. This deformation would result in an increase in the diameter of the discs. However, since the pressure comes to equilibrium after only a few seconds and remains constant all deformation must also occur during the initial seconds of applied pressure. The fact that the reduction in thickness remains constant for the pressure tested indicates that the threshold for deforming the polymer binder lies below the lowest pressure tested.

During the early stages of this study, a large amount of binder was added to the tape casting slurries. Some of the first experimental slurries contained as much as 25-30 wt% binder. The strategy was to prevent cracking due to drying stresses through the addition of large quantities of binder. This represented a “brute force” attempt for overcoming the formation of cracks in the dried tapes by having more of the ductile binder material in the system to absorb the drying stresses and effectively toughen the green tapes. The large amount of binder was successful in preventing cracks; however, it caused the manifestation of even larger defects during burnout and sintering. The larger amount of binder increased the distance between HA particles in the dried tapes resulting in large defects during burnout and sintering. Blowholes, delamination (Fig 2.9), and large cracks resulted from particles not being in close enough proximity to bond during the firing processes. The survival rate of these early trials was at best 40-45%. Some experimental tapes had less than 10% of specimens survive the burnout process. Through numerous trials with experimental slurries and burnout processes it was deduced that poor survivability of specimens was due entirely to the HA particle separation being too great due to the large amount of binder. The solution to this problem was to reduce the HA particle separation through increased deformation of the binder during consolidation. To do this the starting slurry composition was altered to include more plasticizer, making the binder more ductile, and allowing for greater deformation of the binder during cold pressing. It was also discovered that with the binder in a more plasticized form, less of it was required to overcome drying stresses. The effect of both the binder:plasticizer ratio and total amount of binder were tested to identify the combination that provided the largest reduction in thickness, and thus the most

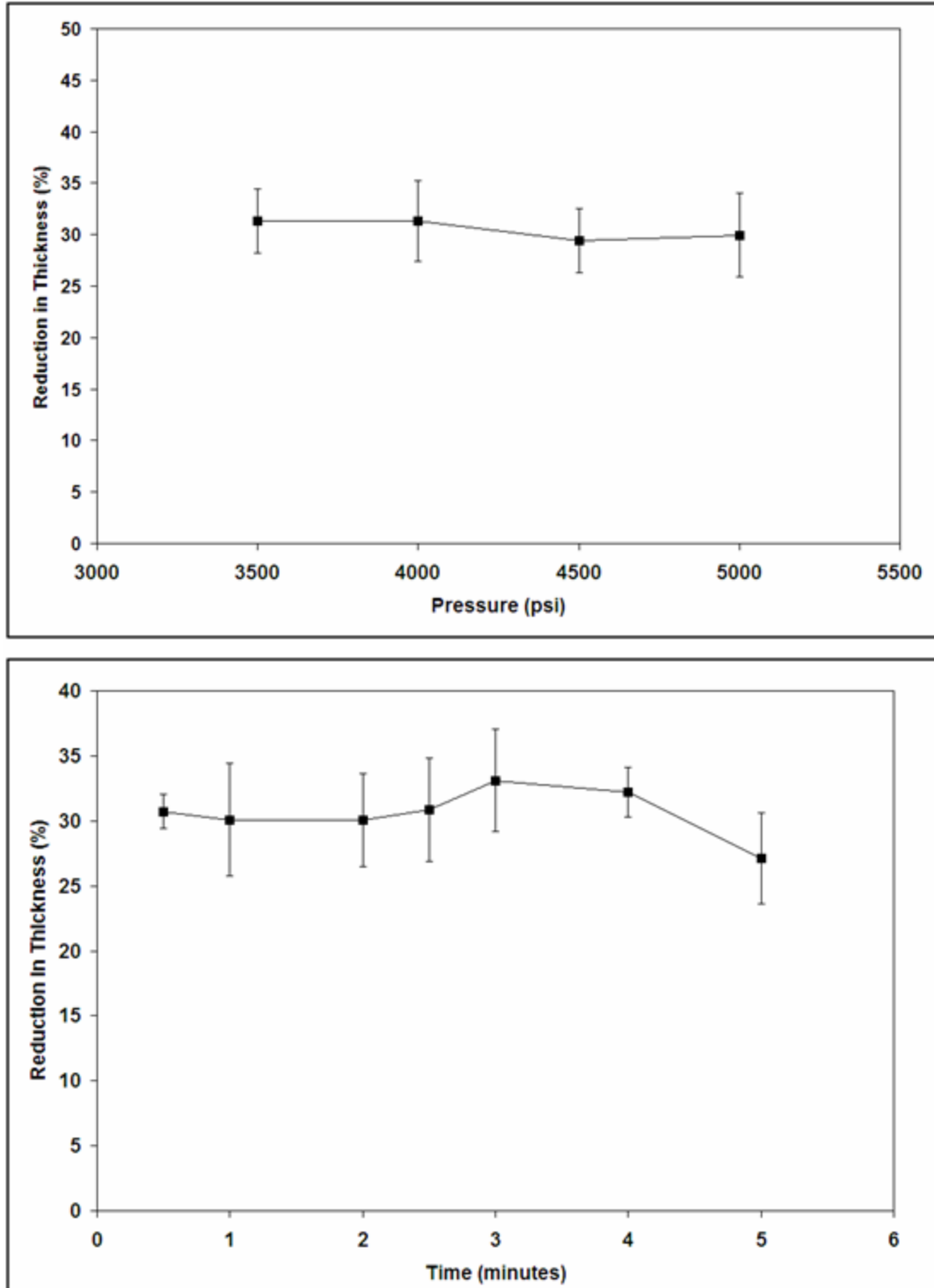


Figure 2.8 Effects of applied pressure (top) and hold time (bottom) on the reduction in thickness of stacked green tapes during cold pressing.

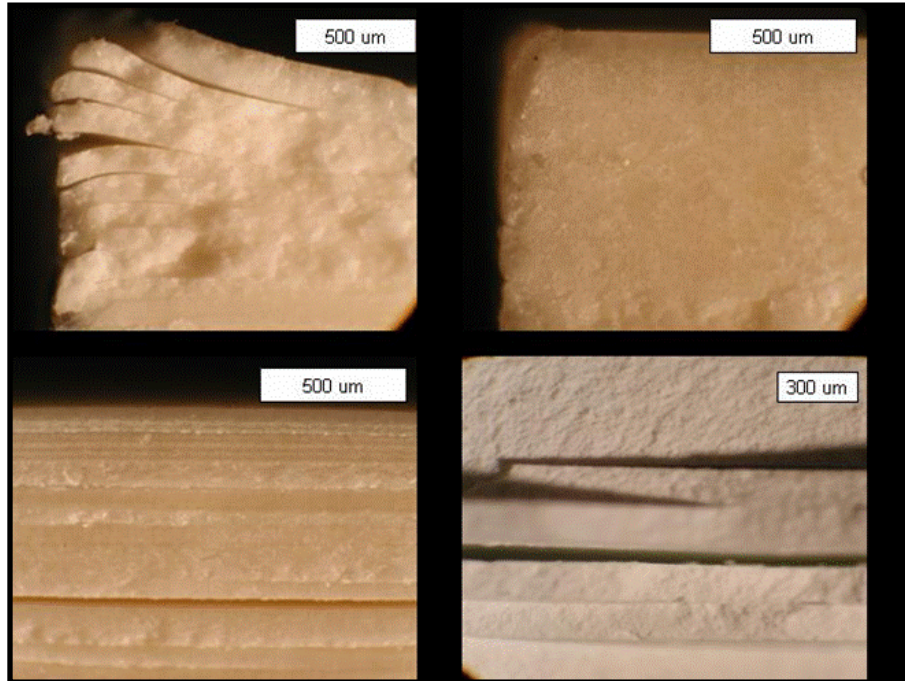


Figure 2.9 Optical micrographs of post-cold pressing edge delamination (top left), delamination at the center (bottom left), full consolidation (top right), and post-sintering center delamination.

consolidation of the green tapes. The results of these tests, Figure 2.10, led to a decreased amount of binder within the tape casting slurries, and an increase in the amount of plasticizer to a level equal to a binder:plasticizer ratio of 1:3 by weight. The results were tapes with increased ductility, and greater deformation during cold pressing due to the now highly plasticized nature of the binder, which decreased the separation between HA particles to a level, which allowed for better densification of the specimens during firing. The net result was a survival rate of greater than 95% for the organic burnout firing process.

Reduction in thicknesses were also measured before and after firing to see how great an effect firing had on the consolidation of the stacked green tapes. The reduction

in thicknesses during both cold pressing and firing were then combined to quantify the total reduction in thickness from the starting thickness of the stacked green tapes to the post-fired thickness of the specimens. The total thickness reduction could then be used as a design tool to estimate the necessary amount of stacked green tapes required to achieve a desired post-firing specimen thickness.

Two other aspects should be noted for the tape casting method developed here. First, the slurry composition in its final form, as described in the methods section of this chapter, can be used for any desired slurry volume. The slurry composition shown in Figure 2.1 can be used in small volumes for tape  $\leq 1$  m, moderate volumes for 3-5 m of tape, which is the limit of the research laboratory, or theoretically for large volumes necessary for mass production.

Second, the addition of all slurry components prior to milling is somewhat unconventional. Typically, slurries would be produced by first completely dissolving binder in solvent, and then adding the plasticizers. Separately, the ceramic powder would be suspended in solvent, dispersant would be added, and the powder-dispersant system would be milled to allow the dispersant to disperse the ceramic particles. Finally, the binder solution would be added, and the entire system milled to allow the binder to infiltrate between the dispersant-coated particles. The binder would be bonded to the dispersant, and this is how the tape would be held together. This is the more conventional stepwise approach to slurry formation. However, in all the attempts made in the early portion of this study to utilize the conventional slurry formation process, a usable tape was never processed. The lack of success with the conventional process facilitated the development of the less conventional “all at once” approach applied here.

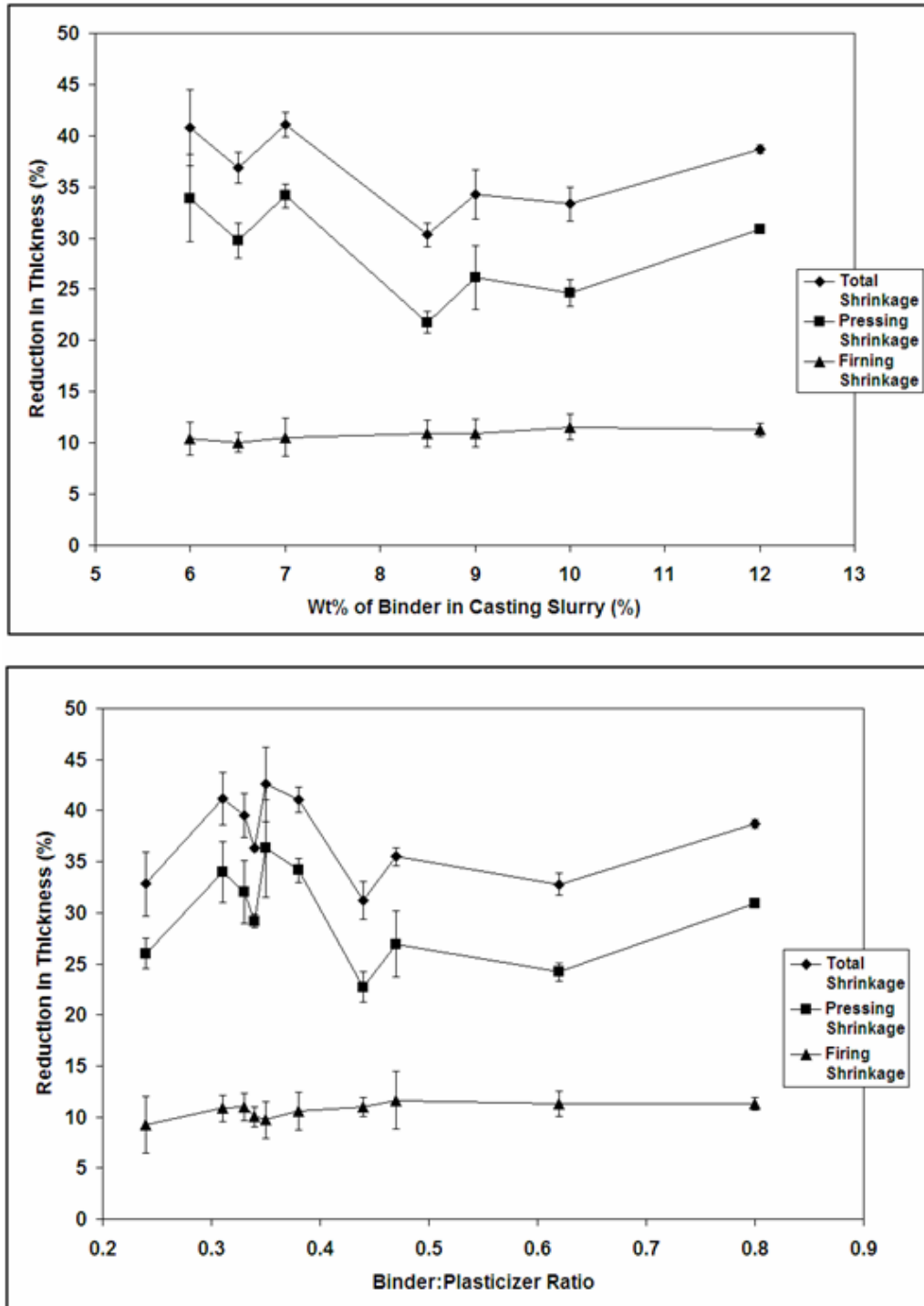


Figure 2.10 The reduction in thickness of the stacked green tapes is plotted versus wt% binder in the tape casting slurries (top), and binder:plasticizer ratio (bottom).

### **Burnout and Sintering Process**

The burnout and sintering process performed on the consolidated green tapes was determined after performing TG/DTA on samples of the green tape. TG/DTA was also performed on specimens following the burnout process to verify that all organic, tape casting materials were successfully removed. The resulting curve, Figure 2.11, showed that all the organic constituents burned out at temperatures at or below 450°C. The green tape TG/DTA curve shows a large volume of material being lost between 200-250°C. This represents the removal of binder and plasticizer as the binder has a glass transition temperature in the range of 140-200°C and the plasticizer has a boiling point of 240°C according to the material safety data sheets (MSDS) provided by the manufacturer. The remaining dispersant was removed at a temperature of 280°C.

The burnout program derived from the TG/DTA data contained two holds. The first 2 h hold at 250°C was added to slow the burnout process and allow degradation products to diffuse out of the specimens. This first hold was essential to the survival of specimens during firing. Without it, the degradation products would build up too rapidly within the specimens building up internal pressure sufficient to cause blowholes to form, thus destroying the specimens. The additional 6 h hold at 450° ensures sufficient time for organics removal from the HA specimens.

The TG/DTA curve for the post-burnout sample shows that the burnout process successfully removes the organic tape casting components. The small decrease in weight can be attributed to the loss of water bound within the HA crystal structure that was released at elevated temperatures [13].

### **Characterization and Mechanical Properties of Post-Burnout Hydroxyapatite**

Following the burnout and partial sintering process used to remove the organic tape casting additives, samples were characterized using XRD to show the effect of the firing program on the crystallinity and existing phases in comparison to the starting powder, Figures 2.12-2.13. The XRD spectrum for the post-burnout HA shows that firing the starting powder to 1000°C increases the degree of crystallinity and causes the transformation of the numerous secondary phases into a more homogenous material that is very similar to XRD spectra for naturally occurring form of HA [8], Figure 2.13. The only difference between the 1000°C HA spectrum and naturally occurring HA spectra is a small peak at a  $2\theta$  value between 37° and 38°. This peak is not found in the XRD spectrum for the starting powder and is therefore formed during the firing processes. This peak represents the formation of a CaO during the firing process, and this is supported by a similar identification of the peak by another group [41].

Additional XRD was performed on specimens sintered at 1200°C. The XRD spectrums for these specimens sintered at 1200°C closely resemble the spectrums for the 1000°C specimens with the only difference being the intensity of a few of the peaks. The result shows that the second firing of the specimens does not cause any phase transformations that would result in the existence of secondary calcium phosphate phases. The result of the firing processes as explained through the XRD characterization is the conversion of a starting powder that contains secondary calcium phosphates into a more homogenous hydroxyapatite phase that closely resembles naturally occurring hydroxyapatite and is stable at the sintering temperatures used in this study.

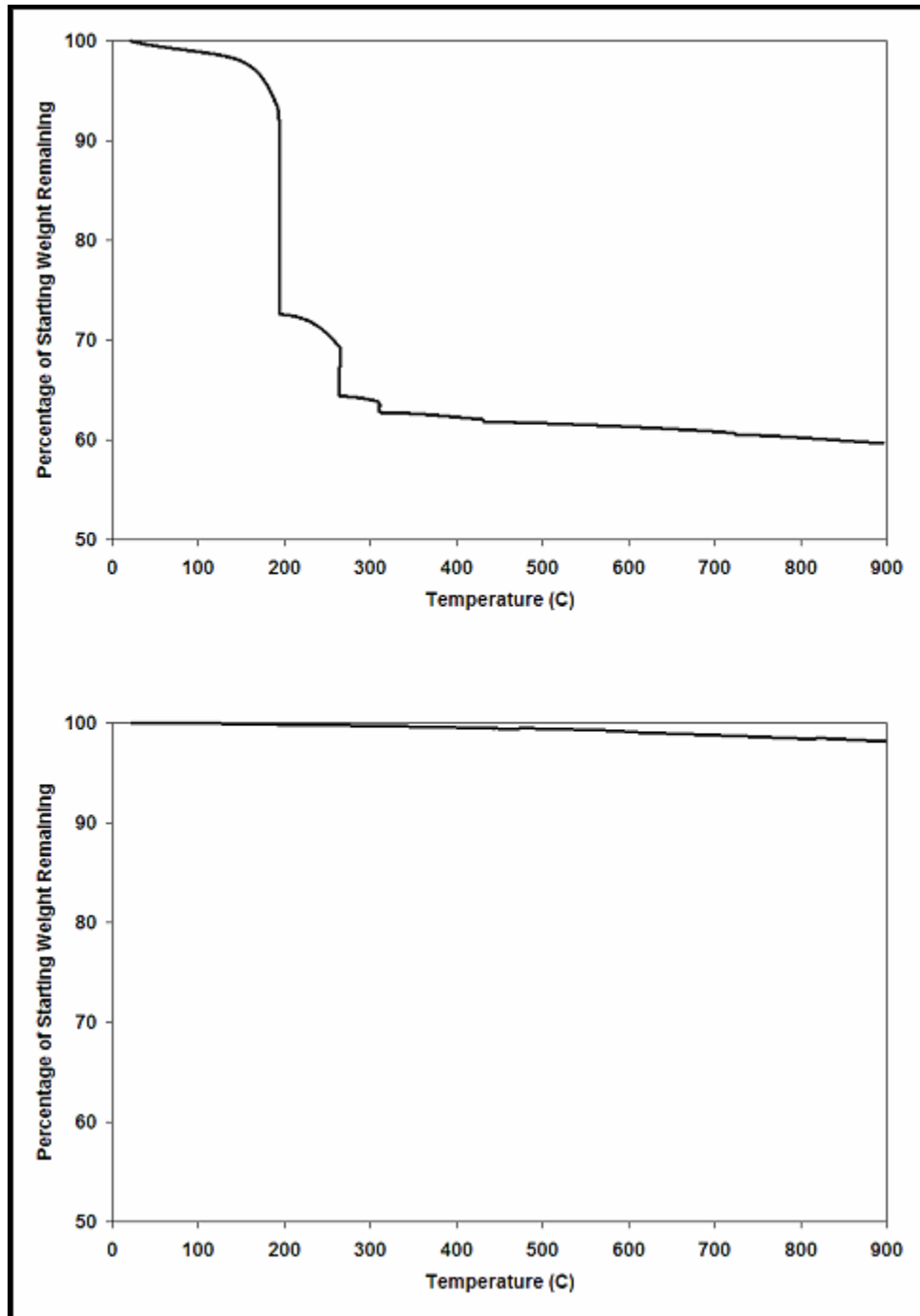


Figure 2.11 TG/DTA data curves for a pre-burnout green tape sample (top) and a post-burnout hydroxyapatite specimen.

### **Problems with Specimens Fired to 1000°C**

Initially it was proposed that the hydroxyapatite specimens would undergo only one firing process effectively minimizing the total energy required to produce testable specimens. A single firing at a relatively low temperature of 1000°C would ensure a large amount of porosity within the system, which would be necessary for future use in biomedical applications. However, it became clear very quickly that a second sintering process was a necessity for specimen fabrication. Less than 10% of the burned out specimens survived the necessary polishing and refinement in order to be used for mechanical testing. Of the 24 samples that could be burned out at one time, only 1-2 samples usually survived to reach mechanical testing, the rest fractured during polishing, most often at the outset. Thus it was determined that in order to conserve starting materials, and produce the number of specimens necessary for completion of this study that the one firing route would have to be abandoned for a two firing system that would yield specimens with greater mechanical stability. Therefore, a short firing study was performed to establish the best temperature that would yield the most usable specimens. “Usable” was defined as having the greatest percentage of specimens survive the polishing process.

### **Mechanical Properties of 1000°C Specimens**

A total of 29 specimens were tested after burnout at 1000°C. These specimens were polished to a thickness of 2 mm, and indented prior to loading in biaxial flexure. Indentation controlled flaw sizes were produced in order to lessen the number of specimens required for a statistical analysis. The six indent loads tested and the resulting mechanical properties are reported in Table 2.1. The diagonals of the Vickers

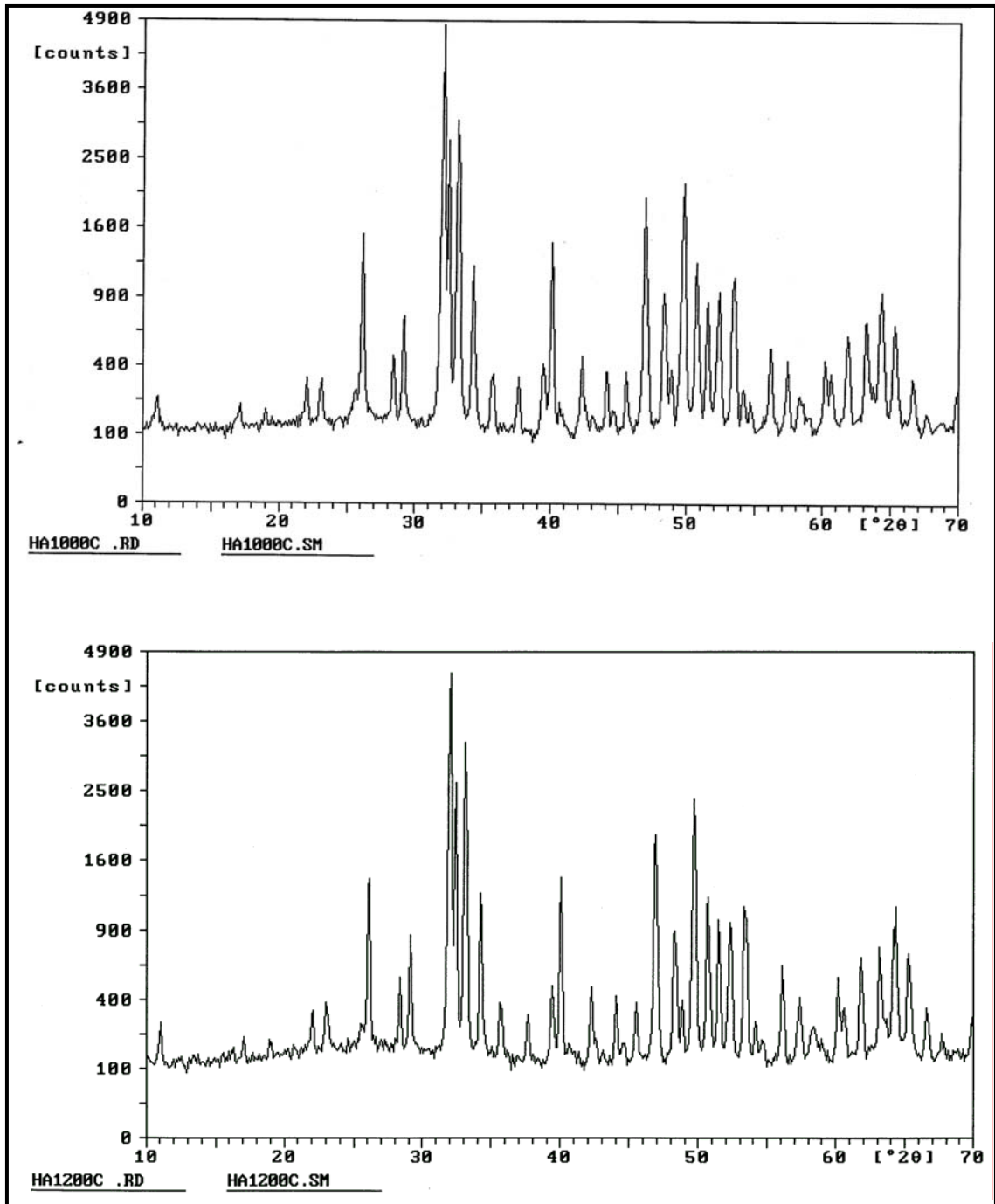


Figure 2.12 XRD spectrum for HA specimens burned out at 1000°C (top) and specimens sintered at 1200°C (bottom)

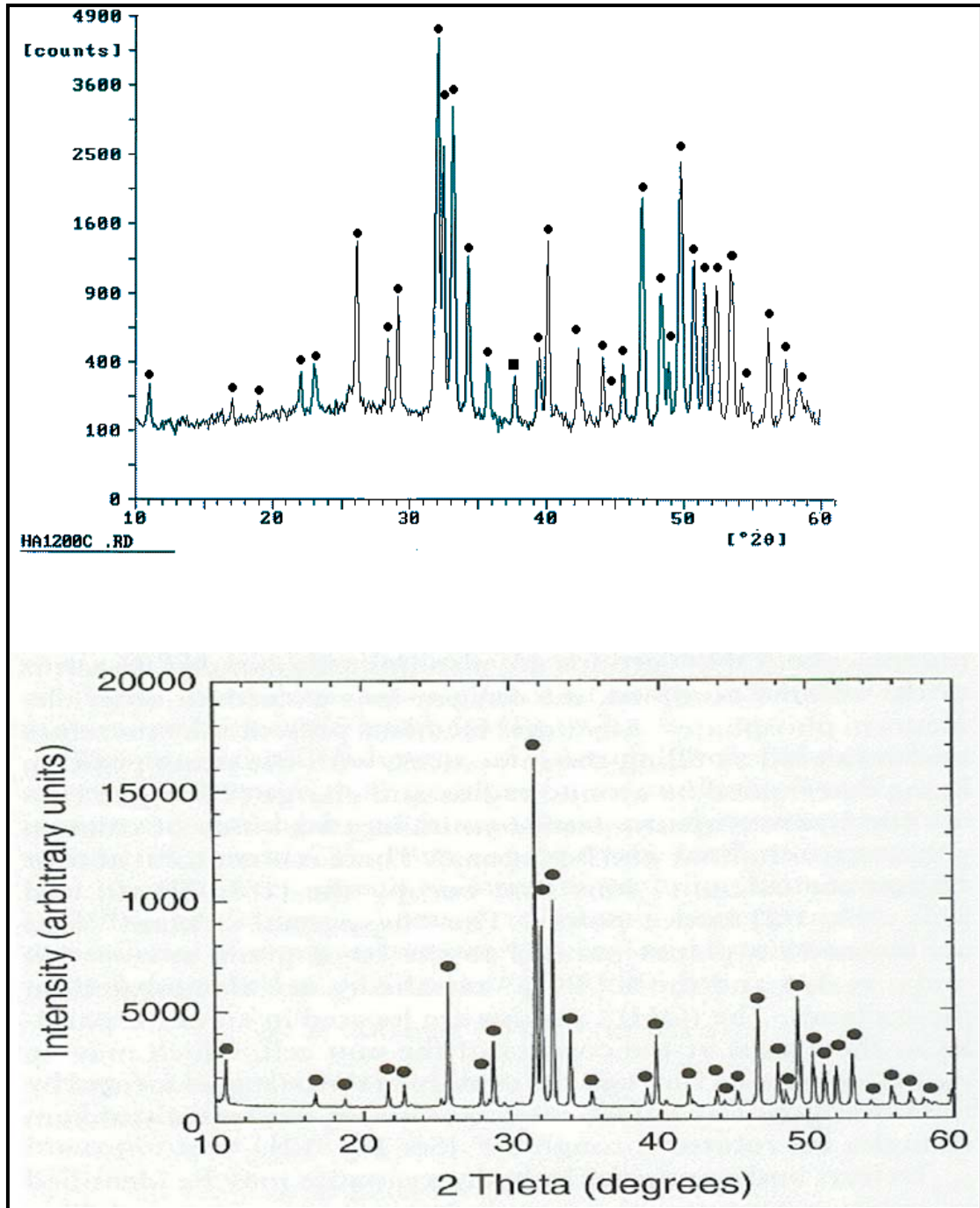


Figure 2.13 XRD spectrum for HA specimen fired to 1200°C (top) and for naturally occurring HA (bottom) [8]. Circles (●) indicate peaks found on both spectra, the square (■) indicates the peak that is unique to the 1200°C spectrum.

impressions (Figure 2.14) were measured for hardness calculations prior to biaxial loading, with the hardness calculated using Equation 2.8. A statistical analysis ( $\alpha = 0.05$ ) showed that there was no significant difference in the hardness values for the six tested indent loads.

Stress at failure was calculated from the experimentally measured failure loads and Equation 2.9. A statistical analysis ( $\alpha = 0.05$ ) showed that failure stresses were statistically different for the range of indent loads used, i.e. a decrease in failure stress with increasing indent load, as expected. Since the fracture toughness is constant for all specimens, a larger indent load results in a larger initial flaw and consequently lower failure stress.

Following failure in biaxial loading, fractures were examined to ensure that cracks originated from the indent flaw Figure 2.14, and these flaw sizes were measured using fractography. Fracture toughness was calculated using both the strength indentation method, Equation 2.14, and direct flaw size measurement, Equation 2.12. These two values should coincide with each other, but do not for the 1000°C samples. The reason for the difference shown in Table 2.1 is flaw size measurements for the 1000°C specimens were difficult due to the very low toughness of the material. Localized crushing around the indents made flaw size measurements potentially inaccurate. An 80% correlation will be shown between  $K_C$  and  $K_{SI}$  for the 1200°C specimens later in this chapter.

### **Constant Fracture Toughness**

Figure 2.15 is a log-log plot of the failure stress,  $\sigma_f$ , versus indent load  $P$ . As discussed in the materials and methods section, if the slope of such a plot is equal to -0.33 then the fracture toughness is constant for the range of indent loads tested. This is

important because deviation from this slope indicates that other factors must be taken into consideration when calculating the fracture toughness. A best-fit line through the six data points, factoring in standard deviation not shown on Figure 2.15, had a slope of -0.35.

Table 2.1 Mechanical data and fractography measurements for HA specimens fired to 1000°C

Indent Load (kgf)	n	Hardness (GPa)	Failure Load (N)	Failure Stress (MPa)	Initial Flaw Size ( $\mu\text{m}$ )	$K_{IC}$ ( $\text{MPa}\cdot\text{m}^{1/2}$ )	$K_{SI}$ ( $\text{MPa}\cdot\text{m}^{1/2}$ )
0.50	5	0.16 $\pm 0.03$	31 $\pm 6$	10.2 $\pm 0.9$	194 $\pm 46$	0.23 $\pm 0.04$	0.27 $\pm 0.02$
1.00	5	0.13 $\pm 0.02$	27 $\pm 3$	8.2 $\pm 0.9$	234 $\pm 40$	0.20 $\pm 0.03$	0.28 $\pm 0.02$
2.00	6	0.18 $\pm 0.03$	24 $\pm 3$	7.5 $\pm 1.0$	284 $\pm 37$	0.02 $\pm 0.01$	0.31 $\pm 0.02$
3.35	5	0.15 $\pm 0.02$	21 $\pm 2$	6.6 $\pm 0.7$	379 $\pm 145$	0.21 $\pm 0.04$	0.32 $\pm 0.02$
4.35	6	0.15 $\pm 0.02$	21 $\pm 2$	6.7 $\pm 0.7$	398 $\pm 43$	0.22 $\pm 0.03$	0.34 $\pm 0.03$
7.35	2	0.16 $\pm 0.01$	23 $\pm 1$	7.1 $\pm 0.2$	366 $\pm 42$	0.22 $\pm 0.01$	0.41 $\pm 0.01$

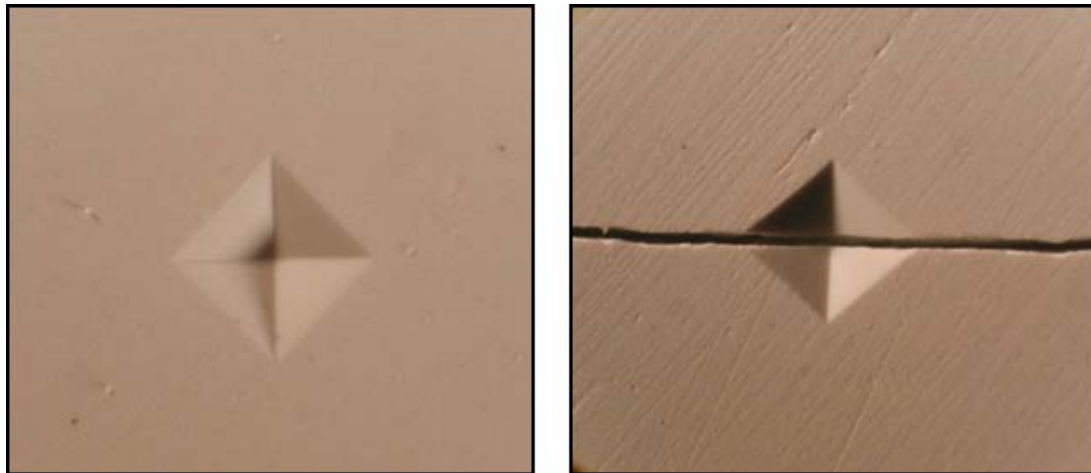


Figure 2.14 Optical micrographs of a Vickers indent for a 1000°C specimen (left) and crack propagation through a Vickers indent.

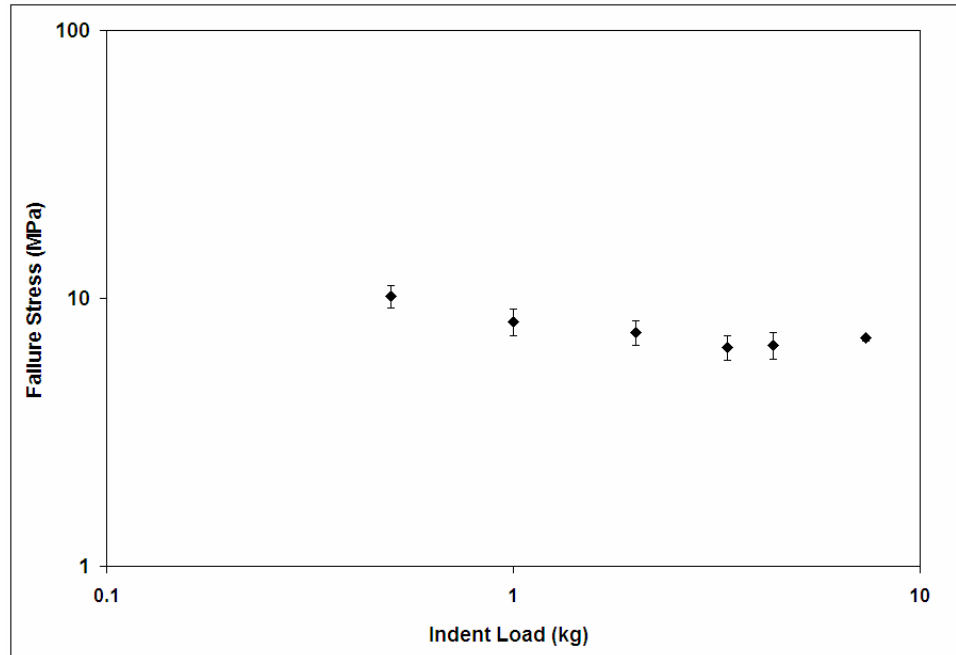


Figure 2.15 Log-log plot of failure stress versus indent load for HA specimens fired to 1000°C

### Firing Study

In order to improve the mechanical strength of the monolithic hydroxyapatite the specimens burned out at 1000°C were then sintered at a higher temperature. A range of elevated sintering temperatures was tested to see their effects of the mechanical strength, density, and hardness. The selected sintering temperatures included 1050, 1100, 1150, 1200, 1250, 1300°C. As with the 1000°C treatment, all specimens were indented prior to loading in biaxial flexure, and for comparison purposes all specimens were indented with a 4.35 kg load. The 4.35 kg indent load was selected to ensure that fracture occurred from the indentation flaw. Six specimens were tested at each temperature except for 1300°C. Only three of the specimens sintered at 1300°C survived the fabrication processes. Most specimens fractured under the loads applied during polishing.

### **Sintering Temperature Effect on Hardness**

The diagonals of Vickers indent impression were measured and the hardness calculated from Equation 2.8. Hardness values increased with increasing sintering temperature, Figure 2.16. The increase in hardness values associated with increases in sintering temperature has been shown to be the result of larger grains sizes [42].

### **Sintering Temperature Effect on Biaxial Flexure Strength**

The indented specimens were loaded in biaxial flexure and the failure load was recorded and used to calculate the failure stress of the specimens using Equation 2.9. The failure stress increased over the sintering temperature range from 1000°C up to 1200°C, as shown in Figure 2.17. The failure stress then remains statistically constant for a sintering temperature of 1250°C. The 1300°C specimens had an increased failure stress, however since only three specimens were tested it is difficult to identify the increase as a real occurrence or just as an anomaly resulting from the three strongest specimens surviving the fabrication process.

### **Sintering Temperature Effect on Density**

The density of specimens fired at increasing sintering temperatures was measured using the Archimedes method described in the materials and methods section. The density of the hydroxyapatite increased with increasing sintering temperature up to a peak at 1200°C, Figure 2.18, and then it decreased for the elevated firing temperatures. The decrease in density is a direct result of decomposition reactions, which lead to the formation of less dense calcium phosphates, calcium oxides, or oxyapatites and water as byproducts [13, 41].

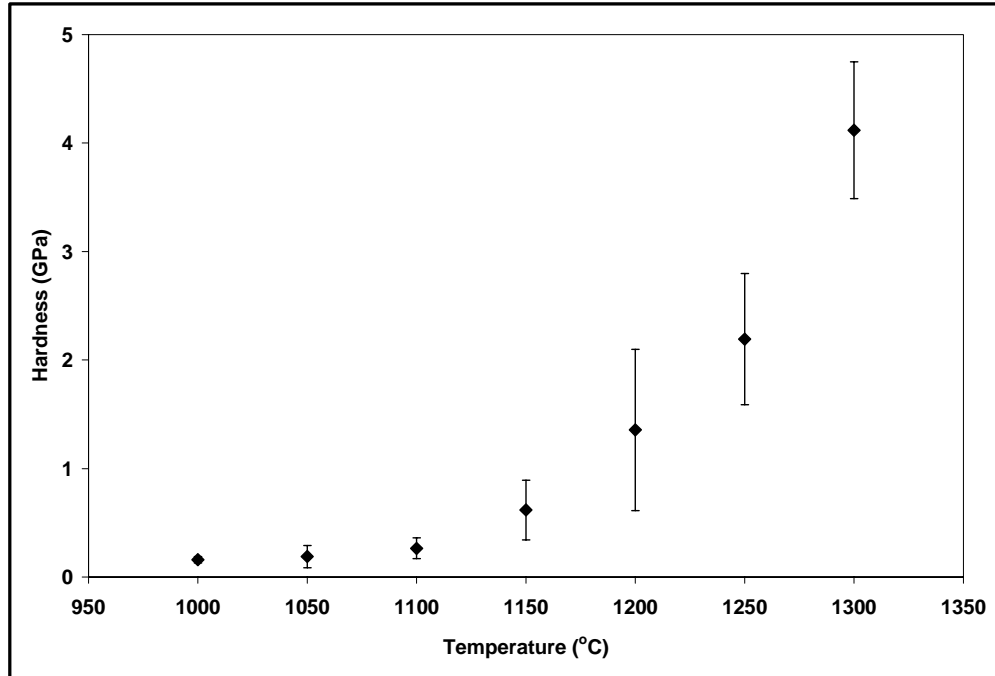


Figure 2.16 A plot of hardness versus sintering temperature for the hydroxyapatite specimens.

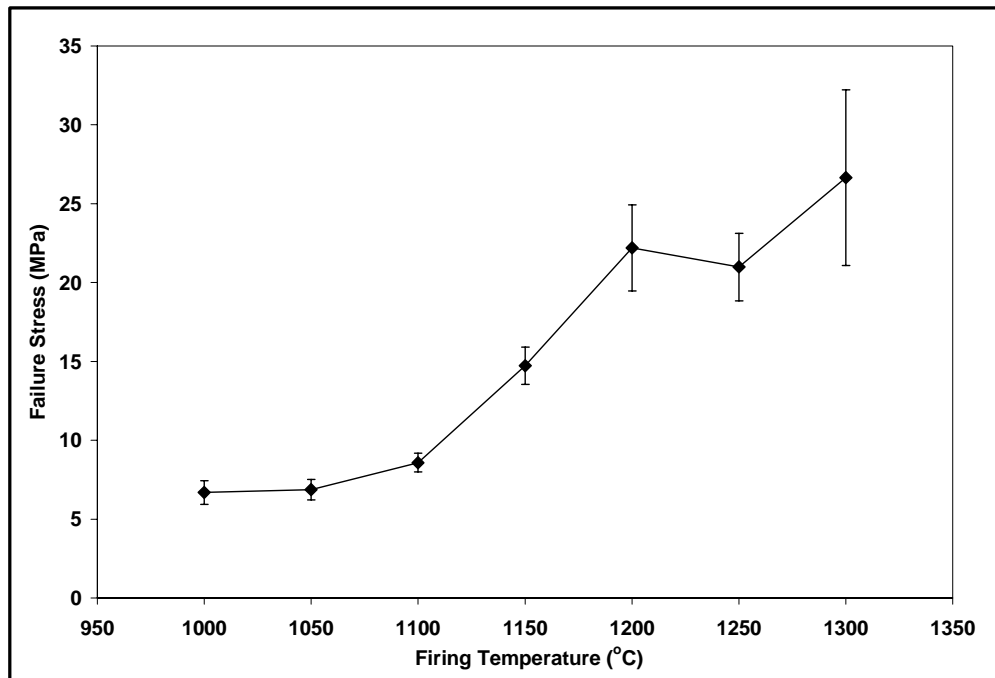


Figure 2.17 A plot of failure stress versus sintering temperature for the hydroxyapatite specimens.

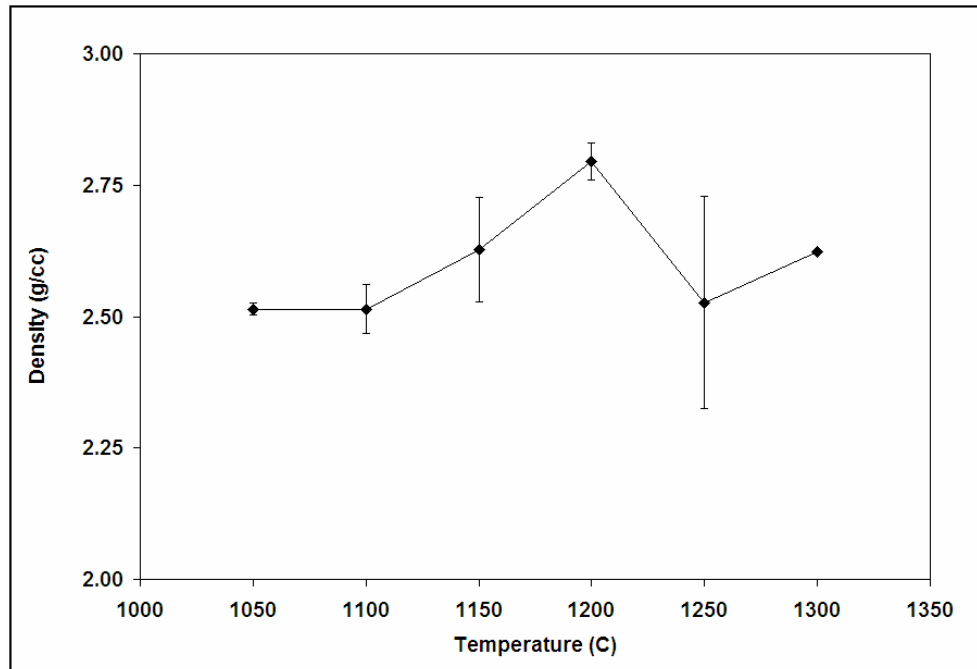


Figure 2.18 Plot of density versus sintering temperature for hydroxyapatite specimens.

### Qualitative Determination of Hydroxyapatite Decomposition

Hydroxyapatite has been shown to decompose into anhydrous calcium phosphates [13] at sintering temperatures between 1200-1450°C depending on the characteristics of the starting HA powder. XRD analysis of specimens sintered at 1200°C showed that decomposition had not occurred up to this temperature. However, a color change, most likely the result of some decomposition, starts to be seen at sintering temperatures at or above 1200°C. A side-by-side comparison, Figure 2.19, of specimens showed that at 1200°C specimens begin to take on a greenish hue, which darkens at 1250°C. Specimens fired at 1300°C, not pictured, take on a purple hue, indicating a further decomposition of hydroxyapatite into calcium phosphates.



Figure 2.19 Color comparison of specimens sintered at five different temperatures. Each row of specimens was fired at the temperature indicated to the right.

### Sintering Temperature Selection

After analyzing the mechanical properties of hydroxyapatite specimens, it was determined, that the hydroxyapatite specimen used for composite formation would be sintered at a temperature of 1200°C. There were three reasons for this selection. The most important was that XRD performed at 1200°C showed that hydroxyapatite, in a form closely resembling natural HA, had not undergone any decomposition significant enough to be show up in the spectrum. The XRD analysis showed that the hydroxyapatite was stable through both the organic burnout process and the additional sintering firing at 1200°C.

The second reason for selecting 1200°C as the sintering temperature was that it provided greatest reproducible failure stress. While potentially the 1300°C firing temperature would produce stronger specimens, the inability to fabricate intact specimens made using this temperature unfeasible. It would be possible to identify the reason for

the brittle nature of the 1300°C specimens, but it was determined that such an analysis would be costly in terms of time and materials.

The third reason for selecting the 1200°C is that it represents the lowest temperature that could produce specimens in bulk quantities. Being the lowest temperature, sintering would require less energy and consequently less heating and cooling time to produce the number of specimens required for this study.

The only draw back of the 1200°C specimens is their density being a relative maximum for the sintered specimens. The total porosity estimated from the Archimedes method calculations was 35-40% of the total volume. While the project rationale for this project called for producing HA specimens with the greatest possible pore volume, as this is desirable for biomedical application, using more dense specimens sintered at 1200°C was necessary for increased processing ability.

### **Optimization of Sintering**

Once 1200°C was established as the sintering temperature for this study, the sintering process was optimized to reduce processing time. The mechanical properties were tested as a function of ramping rates, and hold times. Specimens were fabricated, indented, and loaded in biaxial flexure. The failure stress was then compared for two hold times, Figure 2.20, and three ramping rates, Figure 2.21. The results showed that the failure stress was constant for holds times of 1 and 20 h. This was confirmed by a statistical analysis ( $\alpha = 0.05$ ) that showed that there was not benefit to increased hold times. It was assumed that testing of additional specimens at hold times within in the range between 1 h and 20 h would produce strength values consistent with the 1 h, and 20 h hold strengths. Therefore, no further testing was performed.

Failure stress was shown to decrease with increasing ramping rates. This is mostly likely the result of an inability of the Deltech furnace to keep up with the higher heating rates and consequently the temperature reached was lower than the desired 1200°C. It was determined that 5°C/min was the fastest ramping rate that the Deltech furnace could handle and still ensure reaching the desired sintering temperature at the programmed time.

### **Density and Elastic Modulus of 1200°C Specimens**

The density of the 1200°C specimens calculated from the Archimedes method was found to be  $2.85 \pm 0.06 \text{ g/cm}^3$ . The theoretical density of hydroxyapatite is between  $3.14 - 3.20 \text{ g/cm}^3$ . The calculated density is 10% less than the theoretical density value indicated the existence of significant porosity. The porosity of the 1200°C HA was calculated to be 30-35%. The strength values for the specimens sintered at 1200°C are consistent with hydroxyapatite specimens verified to have 30% porosity through helium pycnometry by another study [13]. It is assumed therefore that the HA specimens produced for this study possess 30% porosity, and that the accuracy of the density measurement is limited due to the low precision of the Archimedes method. SEM imaging of the HA microstructure, Figure 2.22, show that the 30% porosity measurement is plausible. Mercury porosimetry was attempted in order to better quantify the density and porosity of HA specimens, however at the time of writing no data was available.

The elastic modulus of 10 hydroxyapatite specimens sintered at 1200°C was measured using an ultrasonic technique. The specimens were randomly selected from different sintering batches to gain a better statistical average for later use in laminate composites calculations. The elastic modulus would be assumed constant for all of

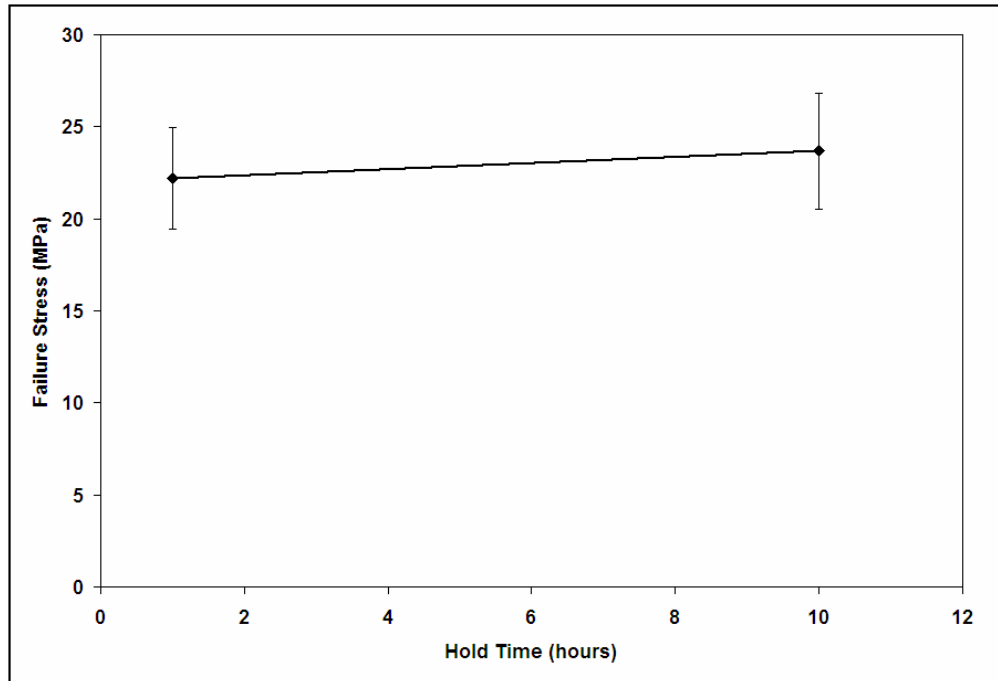


Figure 2.20 Plot of failure stress versus hold times at 1200°C

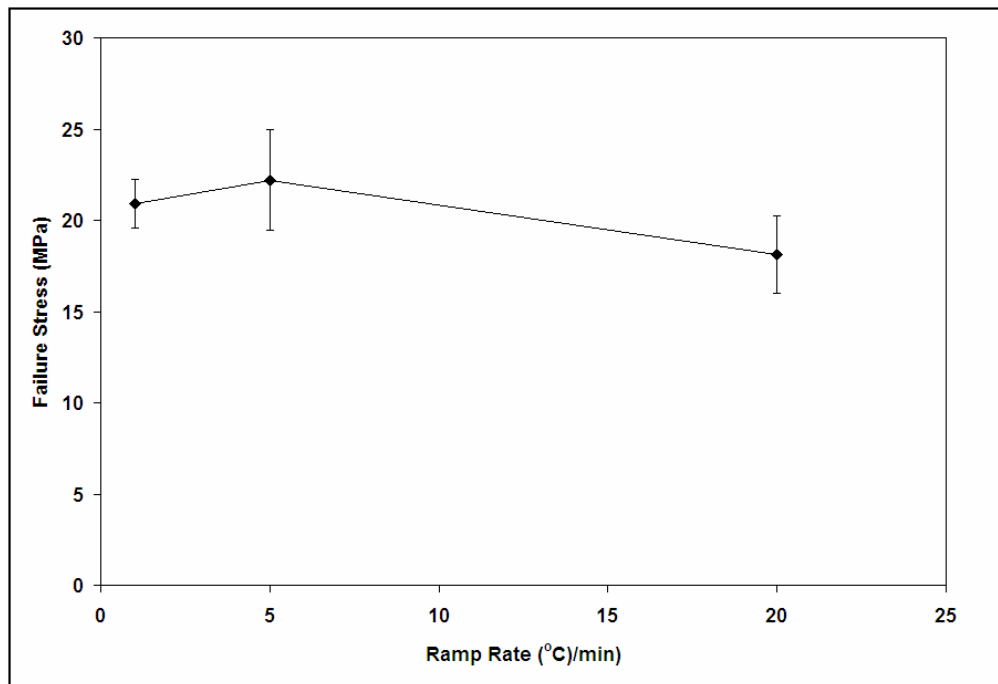


Figure 2.21 Plot of failure stress versus ramp rate sintering temperature of 1200°C.

the HA used in composite fabrication. The elastic modulus was measured at  $56 \pm 3$  GPa, with the lowest measured value being 52 GPa. The 52 GPa value will be used for all composite calculations as it represents the minimum possible modulus for the HA specimens developed.

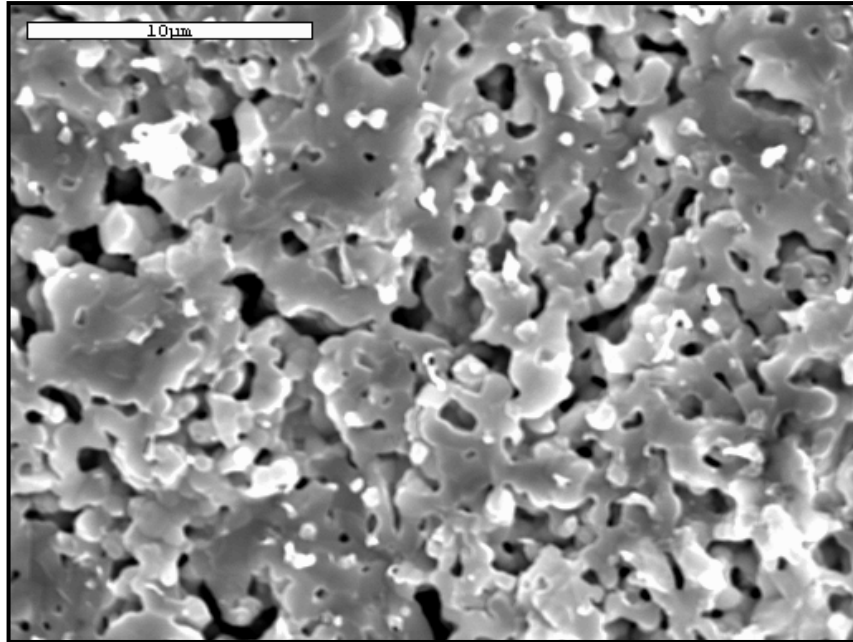


Figure 2.22 SEM micrograph of the microstructure of the hydroxyapatite specimens sintered at 1200°C.

### **Hardness of 1200°C Specimens**

The hardness of the 1200°C specimens was measured for the firing study, Figure 2.16. The hardness was measured at  $1.4 \pm 0.7$  GPa for the size of the Vickers indent impression. This value represents an approximately 1000% increase from the hardness of the 1000°C specimens. This increase in hardness as a result of increased sintering temperature has been well established for HA [30, 41, 43].

### Biaxial Flexure Strength of 1200°C Specimens

The mechanical properties of specimens sintered at 1200°C were characterized in the same manner as the 1000°C specimens. Groups of six specimens were indented and loaded in biaxial flexure to fracture. Four groups of 1200°C specimens were tested, three of these groups were indented with 3.35 kg loads, and one group was tested without indents. The three indented groups were polished to three different thicknesses; these were 1.5, 2.0, and 2.2 mm. Three thicknesses were tested for a failure load comparison with composites having a similar range of thicknesses. The non-indented sample group tested the inherent strength of the hydroxyapatite. Failure stresses of the 1200°C specimens, Table 2.2, showed an increase of approximately 200% over the values measured for 1000°C specimens with the same indent load (Table 2.1).

Table 2.2 Biaxial flexure strength data for specimens sintered at 1200°C.

Group	n	Indent Load (kg)	Thickness (mm)	Failure Load (N)	Failure Stress (MPa)
1	6	3.35	1.5	31 ± 3	19 ± 2
2	6	3.35	2.0	58 ± 6	22 ± 2
3	6	3.35	2.2	70 ± 11	24 ± 4
4	6	N-I	2.0	89 ± 19	39 ± 8

Figure 2.23 is a comparison of stress-strain curves for an indented specimen versus a non-indented specimen. The comparison shows approximately constant elastic modulus as the curves have identical initial slopes, with the elastic modulus being 64 GPa. This is greater than the calculated value from ultrasound, but well within the acceptable range for hydroxyapatite.

## Work of Fracture and Toughness

Work of fracture values were calculated using Equation 2.11, and are reported in Table 2.3. Specimens fractured into either two or three pieces as shown in Figure 2.24. The length of all cracks was measured from fracture surface. All work of fracture integrations and toughness calculations were performed in Microsoft Excel spreadsheets. Work of fracture and toughness values were not calculated for Group 1 because most of the loading data was lost with only the greatest measured load and loading curves being saved on paper. Calculating the area under load-displacement curves by hand would have resulted in inaccurate data being included in the study.

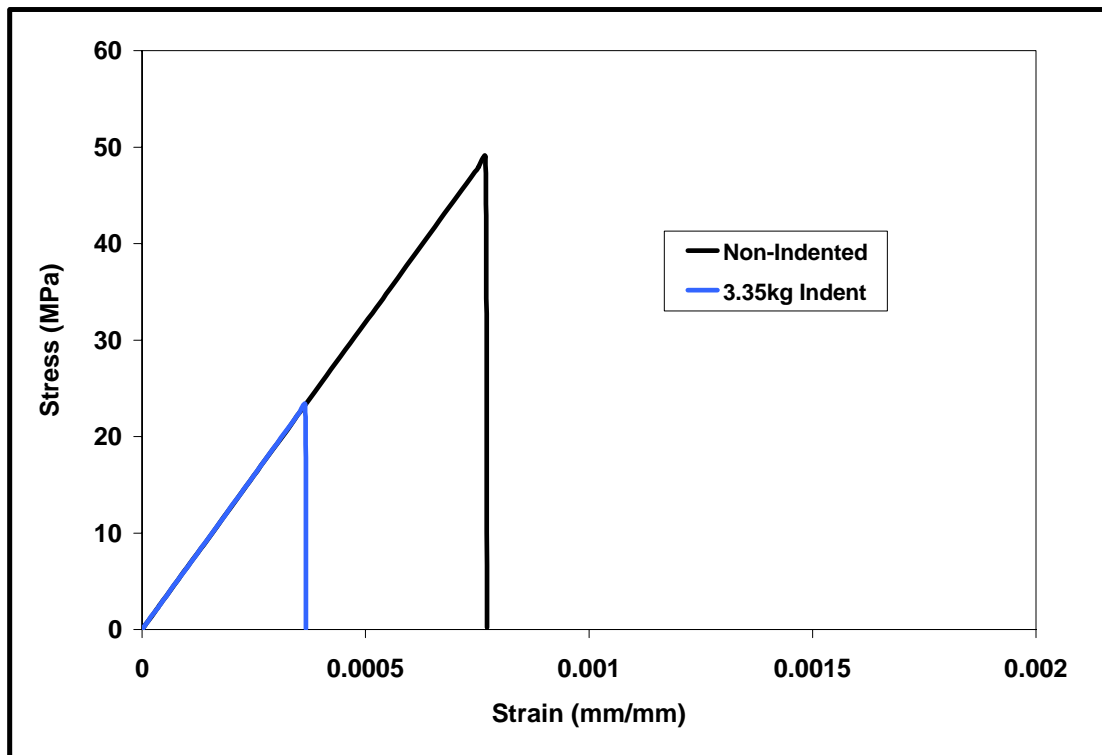


Figure 2.23 Comparison of stress-strain curves for indented and non-indented HA specimens.

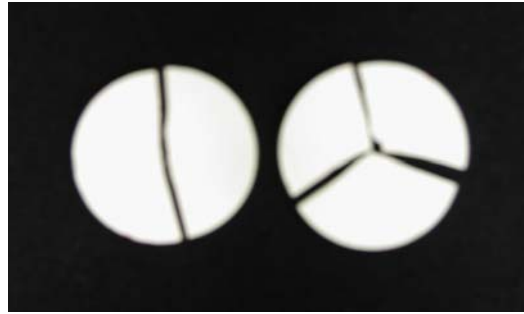


Figure 2.24 All specimens tested in biaxial flexure fractured into either two (left) or three (right) pieces.

Table 2.3 Work of fracture values for specimens sintered at 1200°C

Group	n	Indent Load (kg)	Work of Fracture (kJ/m <sup>2</sup> )	Absorbed Energy at Failure (kJ/m <sup>3</sup> )
2	6	3.35	0.009 ± 0.002	5 ± 2
3	6	3.35	0.011 ± 0.002	5 ± 1
4	6	N-I	0.020 ± 0.006	17 ± 8

### Fracture Toughness of 1200°C Specimens

Fracture toughness values were calculated using the three methods described in the Methods section of this chapter. The fracture toughness values measured using all three methods are reported in Table 2.4.

The measured values for the fracture toughness calculated from the size of the critical flaw,  $K_C$ , and from strength indentation,  $K_{SI}$ , are in reasonable agreement. It has been demonstrated that these two values should be equal, and a plot of these values against one another should yield a line with a slope of 1.0. A plot of the fracture toughness values measured in this study, Figure 2.25, produces a best-fit line with a slope of 0.8. The discrepancy most likely arises from the direct measurement of the flaw sizes and Equation 2.12 which assumes a particular flaw geometry resulting from indentation

Table 2.4 Fracture toughness values for 1200°C hydroxyapatite specimens

Indent Loads (kg)	Initial Flaw Size ( $\mu\text{m}$ )	$K_C$ ( $\text{MPa}\cdot\text{m}^{1/2}$ )	$K_{SI}$ ( $\text{MPa}\cdot\text{m}^{1/2}$ )	$K_{wof}$ ( $\text{MPa}\cdot\text{m}^{1/2}$ )
3.35	$313 \pm 39$	0.59	0.66	1.0
Non-Indented	$98 \pm 43$	0.63	N/A	1.5

yielding a constant value of 1.65 for the geometric constant,  $Y$ . Fracture surfaces generated for the HA were often complex due to the porous nature of the HA microstructure and loading in biaxial flexure, and thus there is some experimental error involved in the fracture toughness calculation. This error accounts for the discrepancy between the two values for fracture toughness. Critical flaws for two of the 1200°C specimens are shown in Figures 2.26 – 2.27.

The fracture toughness value calculated from the work of fracture,  $K_{wof}$ , is statistically greater ( $\alpha = 0.05$ ) than the other two values due to an underestimation of the fracture surface area generated during the fractures process. The projected area of the fracture surface was used for calculation of  $K_{wof}$ , however an area of the fracture surface calculated on smaller length scales is required for an exact calculation of fracture toughness. Because of the area estimation,  $K_{wof}$  should be viewed as an apparent toughness value and not a direct measurement of fracture toughness.

### **Monolithic Hydroxyapatite Specimens**

The focus of this study is on the ability of a composite structure to enhance mechanical properties. To this end, the role of the monolithic testing was to establish baseline mechanical properties for comparison to composite properties. The mechanical properties of the monolithic hydroxyapatite produced here were considered acceptable regardless of how they compared to previous work done with hydroxyapatite. The firing

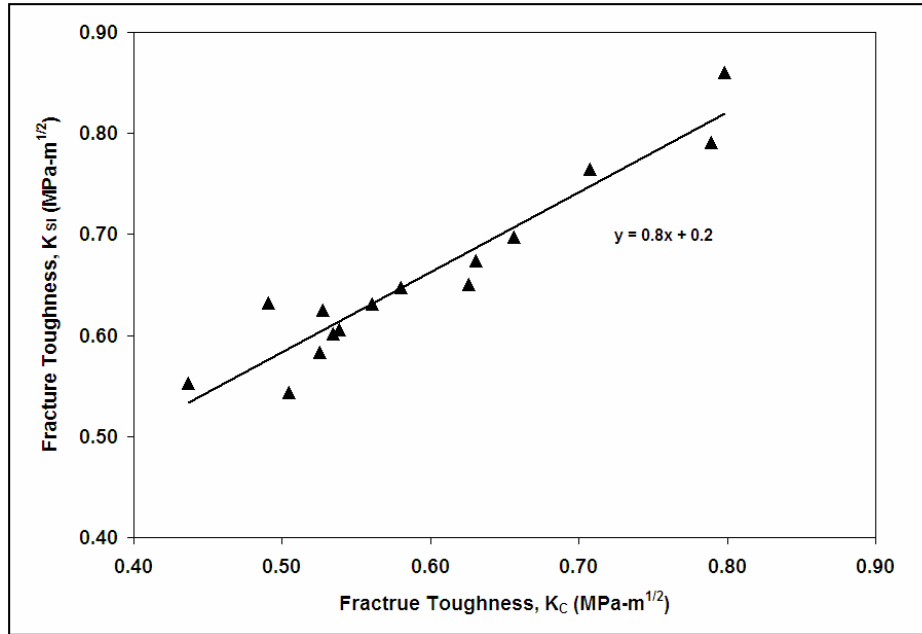


Figure 2.25 Plot of  $K_C$  versus  $K_{S1}$  for the hydroxyapatite specimens sintered at 1200°C.

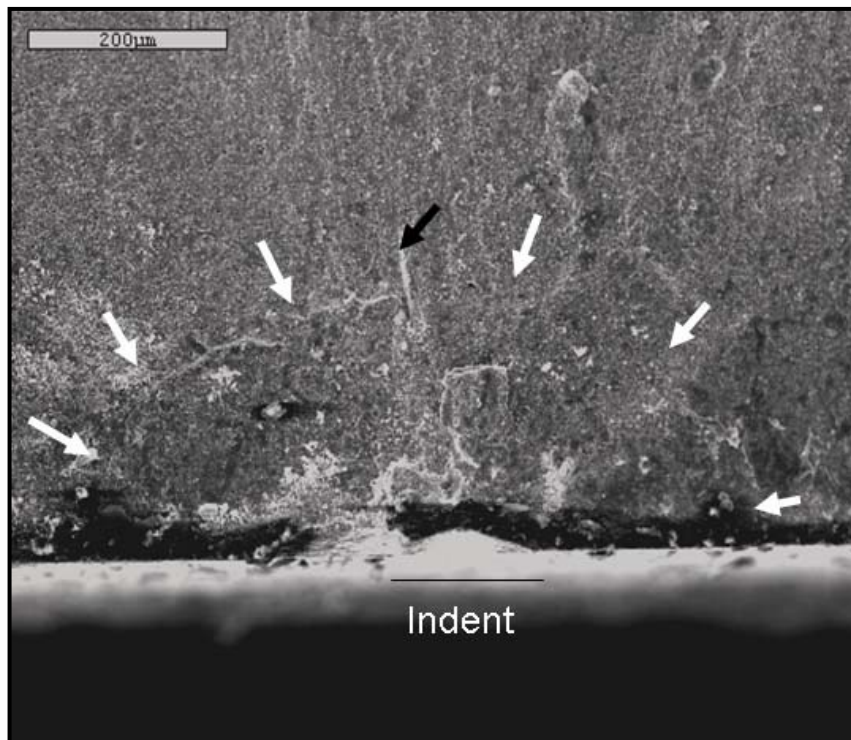


Figure 2.26 SEM micrograph of the initial crack caused by an indent (black bar) for a 1200°C HA specimen. The outer boundary of the initial crack (white arrows) and a twist-hackle marking (black arrow) are shown.

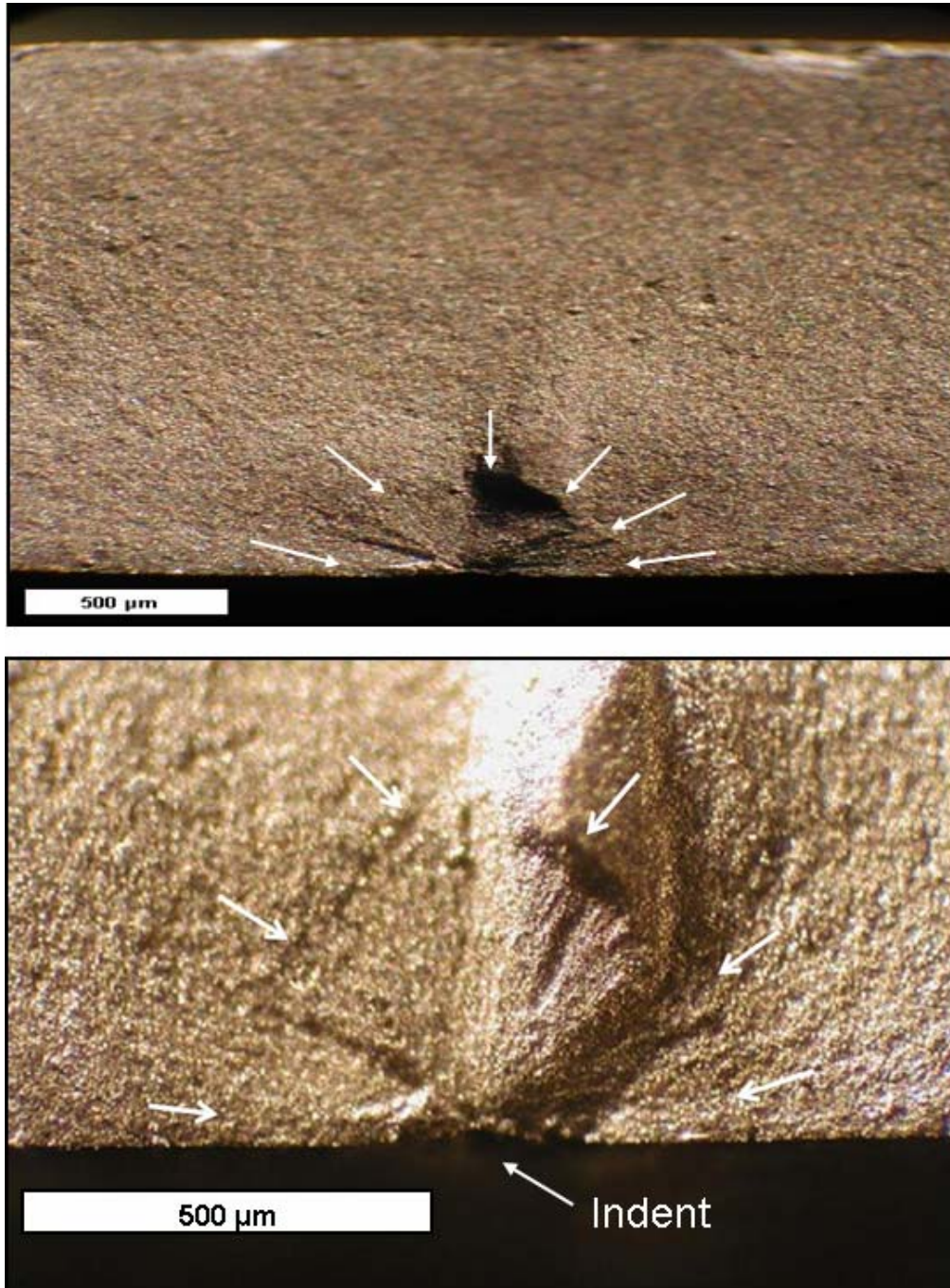


Figure 2.27 Optical micrographs of an entire fracture surface (top) and initial flaw (bottom) of a 1200°C specimen indented with a 3.35 kg indent. The white arrows indicate the outer edge of the critical flaw.

study and analysis performed to ensure that hydroxyapatite specimens could be produced in sufficient quantities for composite formation and that fabrication would be both efficient and reproducible. There are many possible ways to further refine the hydroxyapatite and increase the mechanical properties. The optimization of the hydroxyapatite prior to composite formation is a tangential aspect of this work that was left to future researchers.

## CHAPTER 3 LAMINATE FABRICATION

### **Design and Nomenclature**

#### **Laminate Design**

Symmetric laminates were designed with five total layers. The five layers consisted of two thin outer ceramic layers, each bonded to a polymer layer, and then a thick middle ceramic layer. This design is based on the principle that the stress at which brittle failure occurs in a ceramics is controlled by the fracture toughness of the ceramic and size of the initial flaw as shown by fracture mechanics [38]. Based on this principle it was hypothesized that thinner ceramic layers on the laminate surfaces would limit the potential size of the initial flaw and increase the failure strength of the laminate. The thicker middle ceramic provide the mechanical strength of the laminate. Polymer layers are positioned to increase laminate toughness through crack arrest and reinitiation. Similar toughening mechanisms have been shown to occur in ceramic/metal laminates [24].

#### **Laminate Geometry and Nomenclature**

A laminate design with a five-layer structure of alternating HA and Polysulfone (PSu) layers in the order HA/PSu/HA/PSu/HA was selected for fabrication. Laminates with various geometries were fabricated for studying how different variables, such as individual layer thicknesses, influence mechanical behavior. The initial laminate design was 2.0 mm in total thickness, with a symmetric geometry such that individual layer

thicknesses were 400  $\mu\text{m}$ /200  $\mu\text{m}$ /800  $\mu\text{m}$ /200 $\mu\text{m}$ /400 $\mu\text{m}$ . These laminates will be designated as 400-200-800. This nomenclature represents the individual layer thicknesses in microns in the order of outer HA layer/PSu layer/middle HA layer. Even though not explicitly designated through this naming scheme, all laminates for this study have five total layers. In later chapters, laminates with different geometries will be discussed using this same designation scheme.

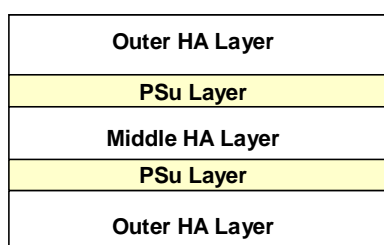


Figure 3.1 Schematic diagram of HA/PSu laminate

### **Solvent Casting of Polysulfone**

Solvent casting, a.k.a. film casting or solution casting, as described by Allcock [44] is a simple technique requiring only a polymer and a solvent, which readily dissolves the selected polymer. Once the polymer has been dissolved, solutions can be poured onto any surface on which a polymer film or coating is desired. Drying occurs through evaporation of the solvents out of the polymer. The result is a polymer film coating on the desired surface.

Casting of polysulfone by immersion precipitation was shown to produce porous membranes used for filtration [28]. This technique is analogous to the solvent casting technique, and indicates a high probability that solvent casting of PSu will produce films with some degree of porosity.

## Materials

The polymer selected for this study was commercially available polysulfone (Udell™ 1700, Solvay Advanced Polymers Inc.). Polysulfone has the repeat unit shown in Figure 3.2. Data sheets provided by the distributor for the polysulfone listed it as having a molecular weight of 35000 g/mol, and a glass transition temperature of 180°C. Molecular simulations and experimental values have demonstrated that polysulfone is an amorphous polymer with little long range order [45]. PSu is distributed in the form of small pellets. The term “PSu pellet” seen at times in this chapter refers to characterization performed on PSu in as received form.

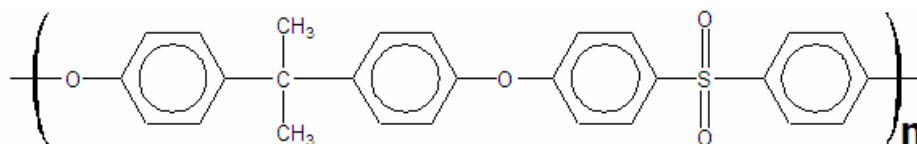


Figure 3.2 Polysulfone

A small number of composites were also fabricated out of a sulfonated version of the polysulfone (sPSu), Figure 3.3. sPSu was prepared through a sulfonation reaction performed by the research group of Dr. Anthony Brennan of the Materials Science and Engineering Department at the University of Florida. sPSu was incorporated into this study because it can be used in association with coupling agents and therefore can be chemically bonded to the HA to increase the mechanical integrity of the PSu-HA interface. However, studying the effect coupling agents have on the mechanical behavior of the laminates has been left to future work. The only results of any significance gained from the sPSu will be shown in discussion on interfaces in Chapter 5.

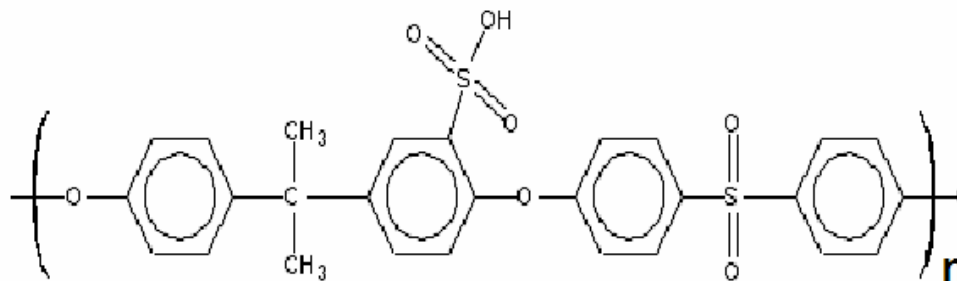


Figure 3.3 Sulfonated Polysulfone

## Methods

### Solvent Casting of Polysulfone

#### Casting Solution

As received PSu pellets were dried at 100°C for 24 h before solution preparation. Solvent casting of polysulfone was performed by first preparing 10 wt% solutions of polysulfone (PSu) in trichloroethane (TCE). Solutions were prepared by dissolving 10 g of PSu pellets per 100 mL of TCE. Solutions were typically prepared in volumetric flasks and had a total volume of 250 mL. Once PSu pellets were added to the required volume of TCE the volumetric flasks were placed on a hot plate with magnetic stirring capability and the solutions were stirred on hot plates for a period of 24 h, or longer as needed to ensure all PSu was dissolved.

The 10 wt% solution was used for all polysulfone layer fabrication in this study. The original casting solutions used were furnished by the research group of Dr. Anthony Brennan of the Materials Science and Engineering Department at the University of Florida. Successful early attempts at casting the 10 wt% PSu solution on glass slides, coupled with the fact that higher weight percent solutions are difficult to produce due to

solubility limits between the PSu and TCE, were the reasons that only one wt% casting solution was used in this study.

Solvent casting of the sPSu was performed using the same techniques as the PSu, but instead of TCE, the sPSu was dissolved in dimethyl formamide. (DMF)

### **Casting of Polysulfone**

Casting of PSu films was performed by pipeting fixed volumes of the 10 wt% PSu solution onto surfaces. The volume of solution deposited on the surface was controlled to within 0.05 mL. Through early tests, it was established that 0.0012 mL of casting solution was required per mm<sup>2</sup> of surface area being coated with the PSu film. This ratio of casting solution volume to surface area was sufficient to produce a 100 μm thick PSu film on a surface. For laminate formation, the casting process was repeated as many times as necessary to build up the desired PSu layer thickness.

After each PSu solution addition, the solution was dried at 70°C for a period of 4-6 h, or until the surface of the PSu was no longer tacky to the touch. Great care was taken to ensure that specimens were dried on a level surface to avoid any variation in the thickness of the PSu layers being cast.

### **Drying of PSu Films**

Drying of the PSu films was studied at temperatures of 70°C, 150°C, and 190°C. 70°C was the drying temperature recommended by the research group that provided the initial solutions, and 150°C and 190°C are temperature above and below the glass transition temperature of the PSu. Solvent removal through drying at these temperatures was characterized using TG/DTA and DSC. The elastic moduli, break stresses, and elongations at break for PSu films dried at each temperature were characterized through

tensile tests conducted according to ASTM D638-02. The 70°C drying temperature was used for the majority of laminates fabricated, with one group of laminates being fabricated using a 190°C drying temperature. 70°C was selected because characterization of the dried films showed no statistical variation between the elastic modulus and failure stress for the three drying temperatures. In addition, the group of laminates fabricated through the 190°C drying temperatures was lower strength than laminates dried at 70°C, as will be shown in the results section of this chapter.

The 70°C drying is also more time efficient because the higher drying temperatures require drying to be done in a drying oven with controlled ramping rates to avoid rapid solvent diffusion out of the solutions. Theoretically drying at a lower temperature should take more time, but when the added time necessary to set up drying ovens and slowly ramp to a higher drying temperature is factored in, the lower drying temperature becomes more efficient.

## **Specimen Preparation**

### **Tensile Testing Specimens**

PSu films for tensile tests were prepared by casting 1.0 mm thick films onto glass slides. From each glass slide two dogbones were punched using a steel die with dimensions conforming to ASTM D1822-68.

### **Laminate Specimen Preparation**

HA-PSu laminates were fabricated using three methods. These methods will be designated: the matching halves method, the bottom up method, and the prefabricated polymer layer method. Each of these methods was used to fabricate laminate specimens for this study. The matching halves method was the original method used to fabricate laminates. Drawbacks associated with this method led to the development of the bottom

up method, which was used to fabricate laminates designed with PSu layers  $\leq 200 \mu\text{m}$ . Again, this method has some drawbacks, which facilitated the development of the prefabricated polymer layer method. This third method was used to fabricate laminates designed with PSU layers  $> 200 \mu\text{m}$ .

All HA specimens used for laminate fabrication had been processed according to the procedure described in the Methods section of Chapter 2 and polished to a thickness of 0.80 mm.

### **Laminate Fabrication Method 1: Matching Halves Method**

Figure 3.4 shows a schematic of this laminate fabrication technique. This technique begins by building PSu layers of equal thickness onto HA layers. In the case of the 400-200-800 laminates, a  $100 \mu\text{m}$  PSu layer was built onto two HA specimens. Layer thicknesses were controlled by measuring the change in thickness that resulted after each casting. Once the difference in thickness from the starting HA disc thickness to the new total thickness was measured at  $100 \mu\text{m}$  the matching halves are ready for fabrication. PSu layers were dried in order to remove as much of the TCE solvent as possible. Once dried, the PSu surfaces were re-wet with a small volume ( $< 0.1 \text{ mL}$ ) of the casting solution. The two wetted surfaces were then placed together and a 300 g weight was placed on top of the three-layer sandwich structure. The sandwich structure was then dried at  $70^\circ\text{C}$  for 4-6 h. The next step was to build PSu layers on a third HA specimens and on one of the outer surfaces of the sandwich structure. Again, PSu layers were built to  $100 \mu\text{m}$  and dried at  $70^\circ\text{C}$ . The dried layers were wetted, placed together, and the weight re-applied to the now five-layer structure. The specimen was then dried

for a final time at 70°C. Once dried the specimen was ready for polishing and mechanical testing.

### **Laminate Fabrication Method 2: Bottom Up Method**

As shown in the schematic for the bottom up method, Figure 3.5, processing of laminates begins by building a PSu layer on a single HA disc, which forms one of the two outer layers of the laminate. Once the PSu is built to the designed thickness, it is wet with casting solution (< 0.1 ml), and the second HA layers in placed on the wetted surface, a weight is applied and the sandwich structure is dried at 70°C. After drying, the second PSu layer is built onto what will become the middle HA layer of the finished laminate and the four-layer structure is dried at 70°C. Following drying, the second PSu layer is wetted with casting solution and a third HA discs in placed onto the wetted surface. Weight is applied to the five-layer structure, and the entire laminate is dried at 70°C. Once dried the laminate is ready for polishing and mechanical testing.

### **Laminate Formation Method 3: Pre-fabricated PSu Layer Method**

As the name implies, the third method involves fabrication of PSu layers with the designed thickness prior to building laminates. A schematic of this method is shown in Figure 3.6. A casting solution in the required volume is pipetted into a 1” deep aluminum pan with a diameter greater than that of the HA discs. The increased volumes of casting solutions necessary to produce thicker PSu layers requires extended drying times to ensure that as much solvent as possible was removed from the PSu films. Subsequently, PSu films were dried for 48 h at 70°C. The dried films were then trimmed to be the same diameter as the HA discs.

Thin PSu layers ( $<50\ \mu\text{m}$ ) were cast on two HA discs, and dried at  $70^\circ\text{C}$ . Following drying, the two PSu layers were wetted with casting solution, a thick pre-fabricated PSu layer was placed between the two wetted surfaces, and a weight was applied to the sandwich structure. The structure was then dried at  $70^\circ\text{C}$ . Again, thin PSu layers ( $< 50\ \mu\text{m}$ ) were cast on a third HA disc, and on one of the HA layers of the sandwich structure. These layers were dried, wetted, and a second thick PSu layer was placed between them. A weight was again applied, and the five-layer structure was dried at  $70^\circ\text{C}$ . Once dried, the finished laminate was ready for polishing and mechanical testing.

### **Salvaging of HA Discs**

As with any processing techniques, there exists the potential for defect formation during the solvent casting process. The ease of the casting process means that any PSu layers with defects could be discarded and a new defect free layer cast. However, the HA discs used for laminate formation require many days of processing and refinement. On the rare occurrence that solvent casting was performed poorly, the valuable HA discs were left coated with a defective PSu layer and could not be used in such condition for continued laminate processing. The remedy for this situation was to reclaim the HA disc by dissolving away the PSu layer. Defective specimens were placed in chloroform until all visible PSu was dissolved away, then the HA discs were heated to  $600^\circ\text{C}$  to burnout any residual PSu. HA discs were inspected for any macroscopic flaws, and were then reincorporated into laminate processing.

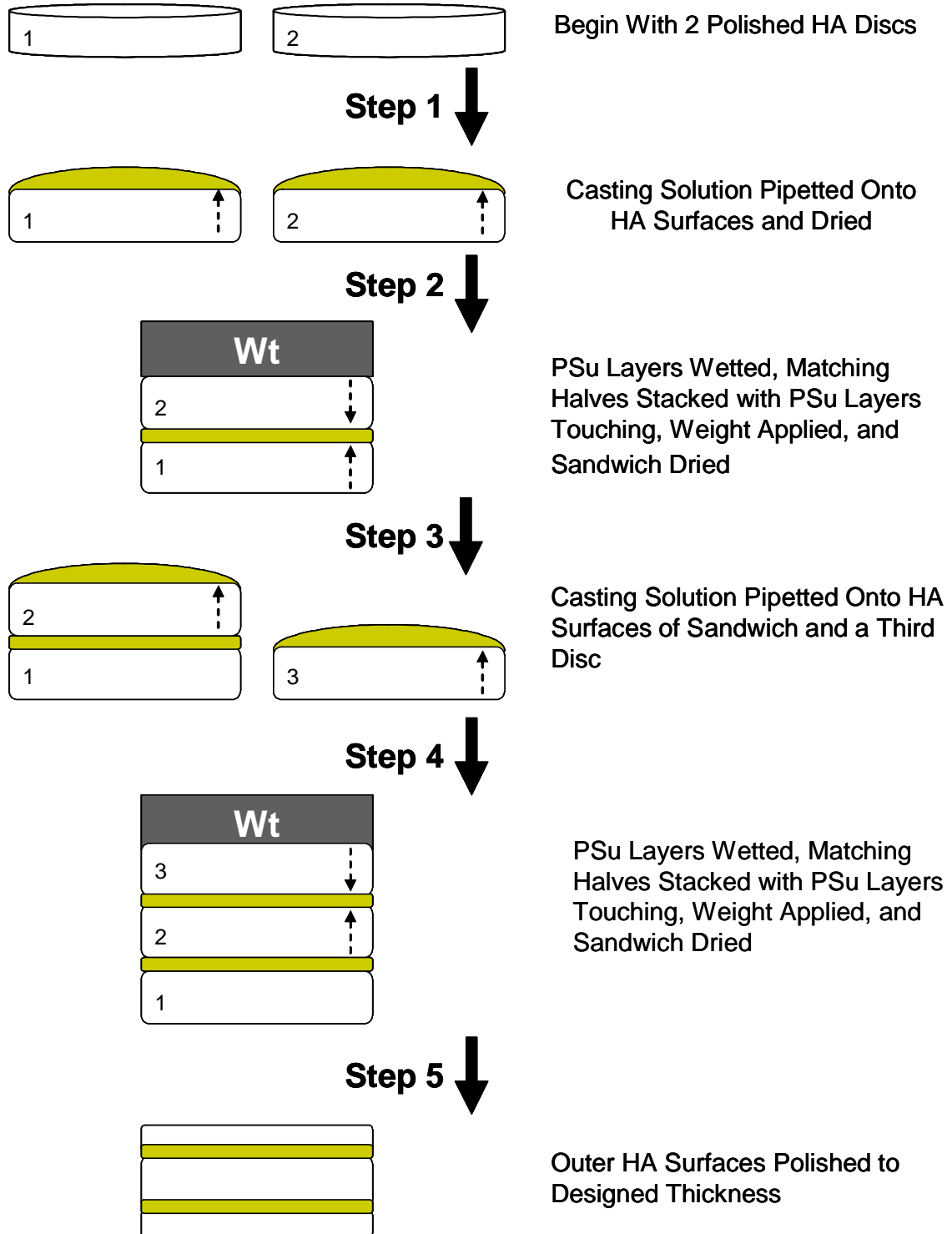


Figure 3.4 Step-by-step schematic of laminate fabrication method 1: The Matching Halves Method

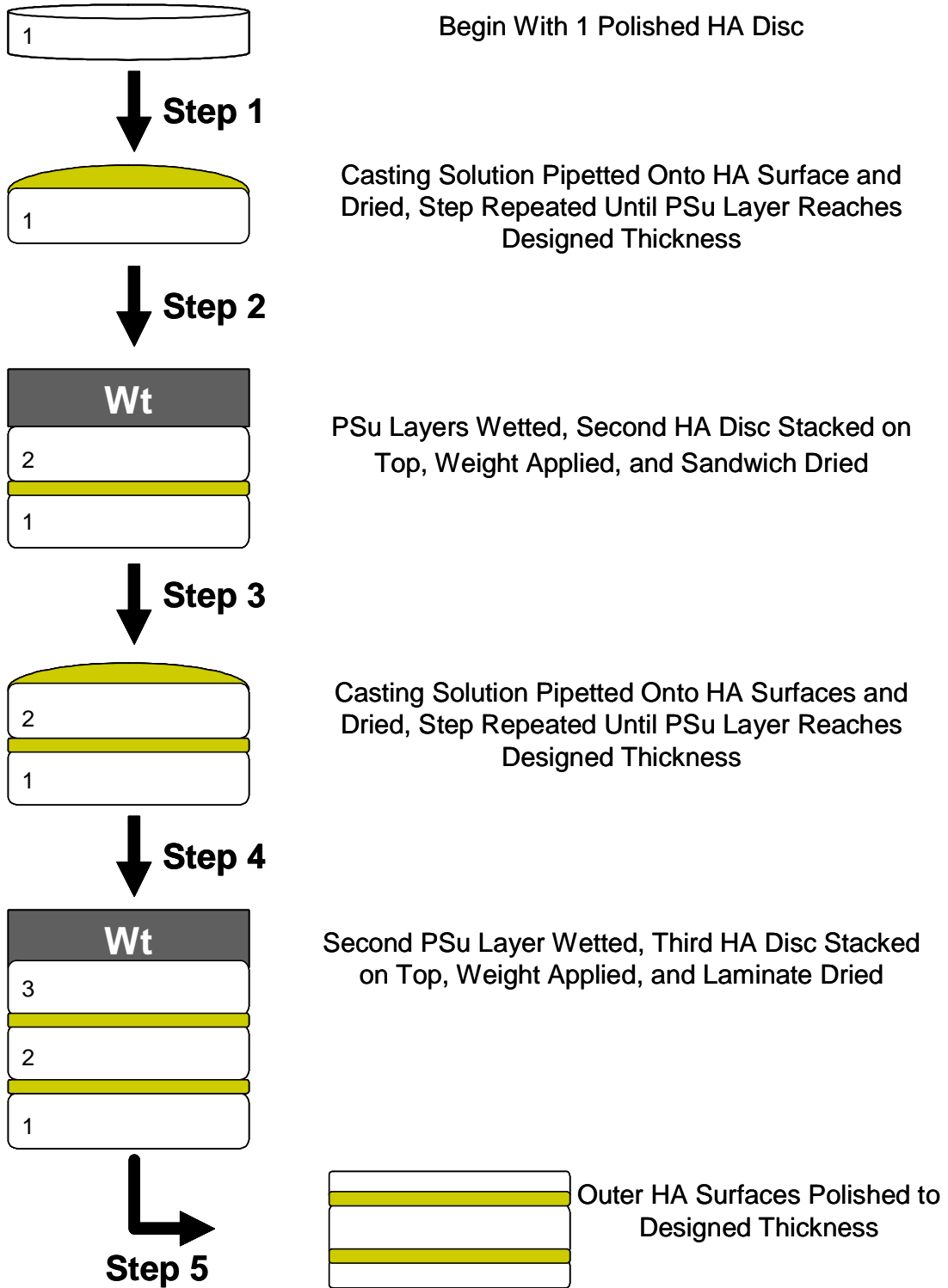


Figure 3.5 Step-by-step schematic of laminate fabrication method 2: The Bottom Up Method

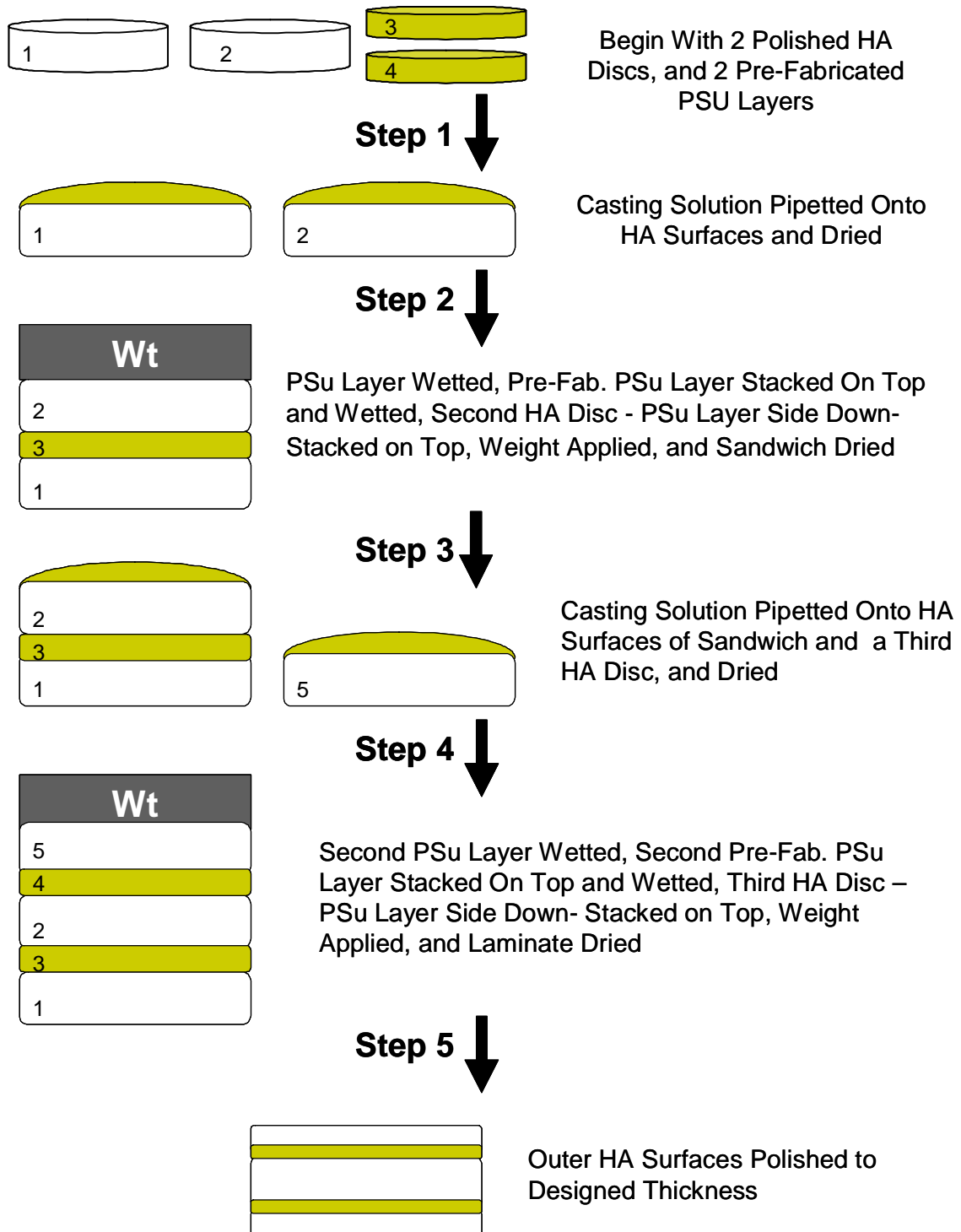


Figure 3.6 Step-by-step schematic of laminate fabrication method 3: The Pre-Fabricated PSu Layer Method

## **Polishing of Laminates**

At the start of fabrication, all HA discs have been polished to a thickness of 800 microns using a 600 grit diamond polishing wheel. After the final drying, the laminates possess three HA layers of equal thickness. The thickness of the entire laminate is measured, and then each outer HA layer is polished to the designed thickness. In the case of the 400-200-800 laminates, half the thickness of the outer HA layers is polished away. Polishing to the final thickness was done through 600 (45  $\mu\text{m}$ ) and 1200 (15  $\mu\text{m}$ ) grit diamond polishing wheels if they were to be indented with non-indented laminates polished through a 5  $\mu\text{m}$  alumina paste.

To test the effect of surface finish on bonding, a set of laminates was prepared for which the surface of the middle HA discs was polished through the 5  $\mu\text{m}$  alumina paste. Failure loads and stresses of these laminates were compared to the same properties for middle HA discs polished with the 600 grit finish. Failure loads and stresses were determined using methodology that will be described in detail in the following two chapters.

## **Characterization of PSu Films and Laminates**

### **Thermal Analysis of PSu Films**

TG/DTA was performed using the same equipment described in Chapter 2. As delivered pellets and solvent cast PSu films were tested at a heating rate of 4°C/min to a temperature of 800°C.

Differential Scanning Calorimetry (DSC) was performed using a differential scanning calorimeter (Seiko Systems). Heating profiles were established through a temperature programs that included three heating and cooling cycles. The cycled

temperature range was from 0°C to 350°C and heating was constant at a rate of 10°C/min.

### **Mechanical Testing of Laminates**

Failure loads were measured for laminates fabricated through each of the three methods described using the biaxial flexure test described in Chapter 2. The process for the converting these loads to stresses is described in detail in Chapters 3 and 4.

## **Results and Discussion**

### **Problems With the Solvent Casting Methods**

#### **General Casting Problems**

The nature of the solvent casting technique leads to bubble formation within the dried PSu layers. In some cases while diffusing out of the drying layers, the solvent is trapped in pockets. When this occurs on the surface, these pockets can expand to form large bubbles, see Figure 3.7. Solvent pockets forming within a PSu layer between two HA discs form locations of stress concentration, which occasionally caused fracture of an HA layer, see Figure 3.7.

The other problem associated with solvent casting was drying stresses arising from shrinkage of the PSu layers due to solvent loss. The drying stresses were of sufficient magnitude to cause fracture of the HA discs. The result was either a completely fractured HA disc or peeling of the PSu layer off the HA discs (Figure 3.8). In one case of complete fracture of the HA disc, a critical flaw was identified through fractographic analysis of the fracture surface. The measured size of the flaw showed that a failure stress comparable to the biaxial flexure strength of the HA was reached. The major problem with this particular failure mode was that detection of the failed HA discs proved difficult as the PSu layers would hold the fractured pieces together causing the crack to

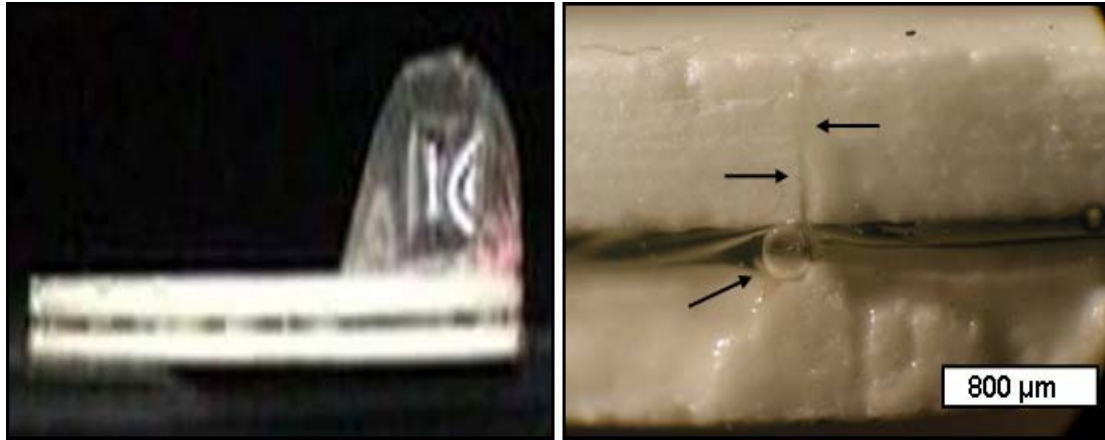


Figure 3.7 Optical micrographs of (left) a large surface bubble formed during laminate fabrication, and (right) a small bubble (black arrow) within a PSu layer that caused a HA layer to fracture (white arrows).

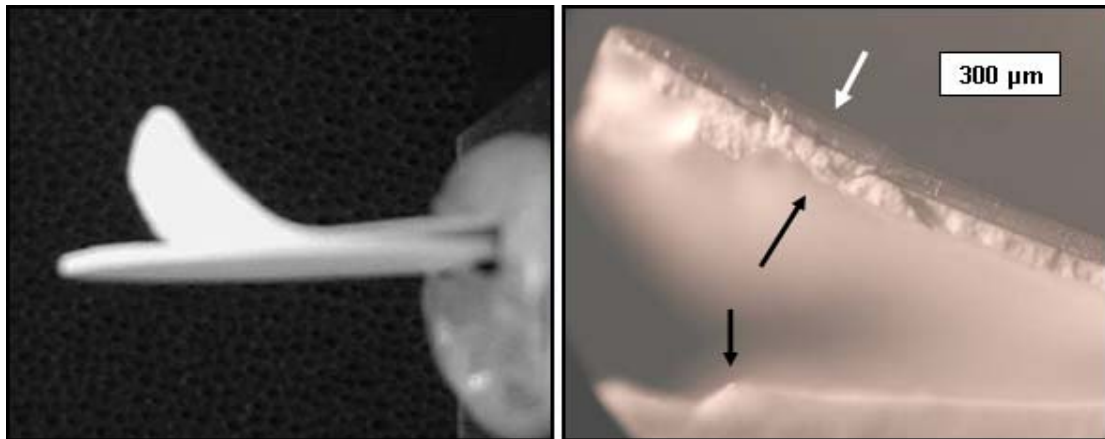


Figure 3.8 Left: Optical micrograph of a PSu layer that peeled from the HA disc during drying. Right: Higher magnification image of the PSu layer (white arrow) that peeled due to fracture of the HA layer (black arrows) which is still bonded to the PSu layer.

be undetectable through a macroscopic inspection. Once this failure mode was identified, all HA discs were inspected microscopically at each step of the laminate formation process to ensure that no fractured specimens were incorporated into laminates.

The second failure mode, peeling of the PSu layer from the HA discs, was the more prevalent of the two types of failure caused by solvent casting. These failures also occurred by fracturing the HA. However, in this case the fracture tended to propagate in the direction of the PSu/HA interface. Figure 3.8 shows that this failure was not of the interface itself, but of the HA as evidenced by the thin HA layer still bonded to the PSu post failure. Although no direct evidence was found, it is most likely that these failures occurred along within the HA along the interface of what was formerly two green tape layers that were not fully bonded during sintering. Most of the post-firing delamination was seen closer to the center of the HA discs rather than near the outer surfaces. Through polishing of the specimens these delamination flaws were moved from the center to the surface of the HA discs, marking these defects the most plausible explanation for the peeling failure seen during solvent casting. These failures were prevented through casting of multiple thin PSu layers instead of one thick layer. The drying stress associated with the thin layers was of lesser magnitude and consequently prevented failures of this type from occurring.

### **Problems with the Matching Halves Method**

The matching halves method for fabricating laminates was the first method developed for laminate fabrication. This method is the most time efficient of the three methods, but turned out to have the largest drawback. This method requires half the processing time of the other methods because each PSu layer can be built

simultaneously on matching HA specimens and then combined to form the designed PSu layer. This is a simple two-step process to producing each polymer layer. However, problems arose from the inability of gases, trapped when combining the two halves, to escape through the already dried layers. The result was the formation of a large open cavity at the center of the PSu layers. The cavity formed at the center because the wetted PSu layers dry the quickest at the outer edge where diffusion of the solvent into the ambient environment occurs almost immediately resulting in a less permeable skin around the edge. As the rest of the PSu layer dries, evaporating solvent and gases migrate to the center of PSu layer as this is where drying occurs the slowest and the PSu is still the most permeable. The resulting pressure forces separation of two halves of the PSu layer. The two layers dry separately and can trap a large pocket of evaporated solvent and air.

This processing problem was discovered when specimens were indented prior to mechanical testing. Instead of indenting the outer HA surface, the indenter proceeded to penetrate through the entire outer HA layer resulting in a large hole, Figure 3.9. Shortly after indentation of these specimens, the distinct odor of TCE could be detected in the environment surrounding the indenter, indicating the release of the trapped solvent. Specimens were fractured despite these huge flaws, and analysis of the fracture surfaces revealed the large cavities at the center of the specimens, Figure 3.9. Thirty laminates prepared through this method were indented with 3.35kg Vickers indents. Hardness measurements, shown in Table 3.1, indicated that cavity formation occurred in 43% of the laminates. This percentage represented an unacceptable number of defective

specimens produced through this method and facilitated the development a better laminate formation method.

Table 3.1 Hardness of laminates made through the matching halves method.

n ( $N_{\text{total}} = 30$ )	Hardness (GPa)	% ( $n/N_{\text{total}}$ )
17	$1.20 \pm 0.05$	57
13	$0.05 \pm 0.03$	43

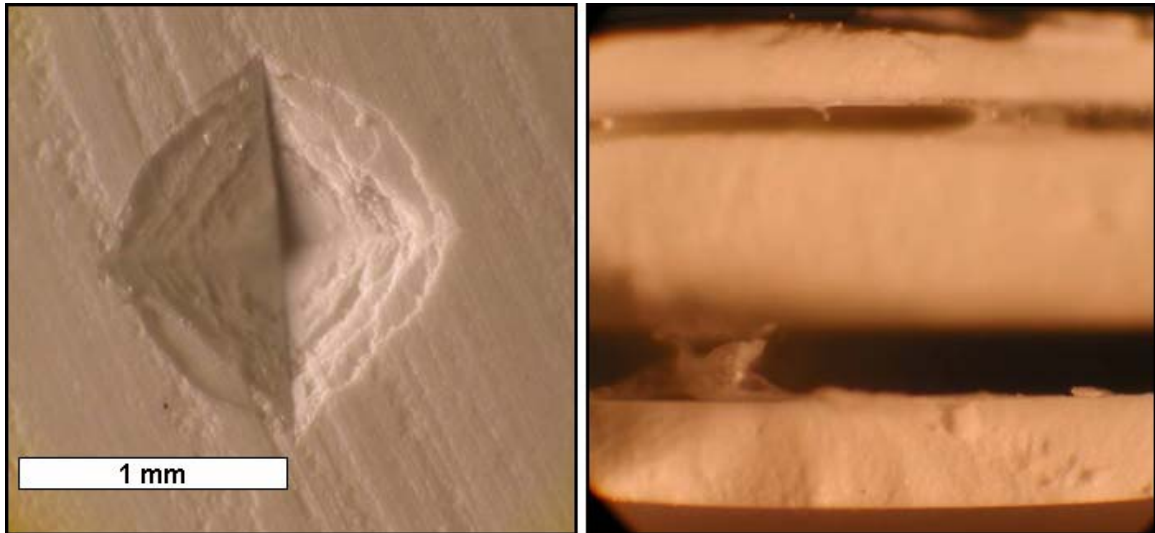


Figure 3.9 Optical micrographs of a large hole that formed during indentation (left), and of a laminate with a defective PSu layer containing a large open cavity (right)

### Problems with the Bottom Up Method

The bottom up method was developed to prevent the formation of a large cavity in the PSu layers. Laying down the complete PSu layer onto one HA disc provides a greater surface area for solvent diffusion. Drying of laminates fabricated through this method was always done with the newest added layer positioned at the top to allow for solvent

evaporation through the new layer prior to drying. Hardness for 19 laminates made through this method indented with 3.35 kg Vickers indents was measured at  $1.33 \pm 0.20$  GPa. This value includes 100% of the laminates fabricated demonstrating that there was no longer the potential for large cavity formation during processing. SEM, Figure 3.10, taken after mechanical testing revealed that instead of one large open cavity at the middle the solvent formed many small cavities or bubbles throughout the layer.

The drawback to this method was that it could only be used to fabricate laminates with PSu layers with thicknesses  $\leq 200 \mu\text{m}$ . The reason for this is that when the casting solution is pipetted onto the HA disc surface it forms a meniscus. As the PSu layer dries

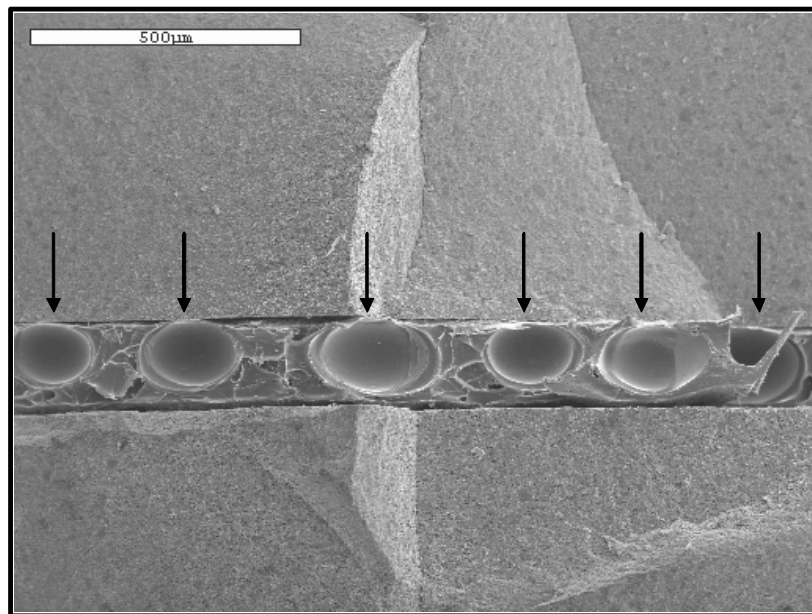


Figure 3.10 SEM image of bubbles (black arrows) which formed during laminate fabrication using the bottom up technique.

it retains the rounded edge formed by the meniscus. Subsequent PSu castings to build up the thickness of the PSu layer result in an increase in the distance between the outer edge of the HA disc and the outer edge of the PSu surface layer. When the next HA disc was

added, the round edge of the PSu layer led to an open area between the surfaces of the HA discs. When the outer HA layers are polished these open areas act a pivot points and concentrated stresses which leads to chipping of the outer HA layer (Figure 3.11). For PSu layers  $\leq 200 \mu\text{m}$ . The chipping occurs outside the diameter of the biaxial flexure

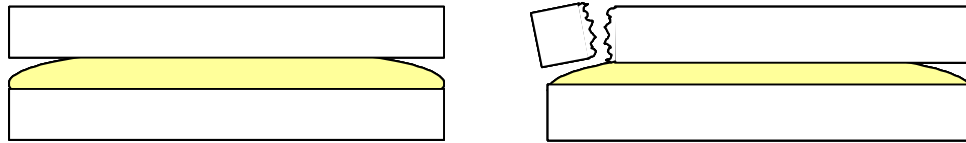


Figure 3.11 Schematic drawing of chipping failures that occur when fabricating thick PSu layers through the bottom up method.

support ring and thus does effect mechanical testing. However, with thicker polymer layers chipping can occur inside the diameter or the three-ball support. Chipping inside the support diameter was deemed unacceptable was this could result in lower values for failure loads and thus jeopardize the statistical integrity of the study.

### **Problems with the Pre-fabricated PSu Layer method**

The method of pre-fabricating PSu layers was developed because it prevented the chipping problem associated with the bottom up method. The pre-fabricated PSu layers were trimmed to the exact diameter of the HA discs and thus there are no gaps formed at the edges. There are two drawbacks to this method. The first is the 48 h required to dry the PSu layers is equivalent to the time required to completely fabricate laminates through the other methods. Therefore this method is more time consuming that the other methods.

The second drawback to this method is alignment of the stacked five layers during drying of the laminate. Due to both sides of the thick PSu layer being in contact with wetted surface the layers were susceptible to sliding if stacking and drying were not done on a completely level surface. The slightest angle would cause laminate layers to slide off-center and as such are unusable. When this occurred the defective laminates were placed in chloroform, the PSu layers dissolved, and the HA discs reused in other laminates.

### **Thermal Analysis of Polysulfone Layers**

#### **TG/DTA of Polysulfone**

A full TG/DTA curves generated for the as received PSu is shown in Figure 3.12. TG data was plotted as a percentage of the starting weight versus temperature. The full curve for the as received PSu shows the onset of degradation occurring at approximately 450°C, with all remnants of the PSu completely burned away by 625°C.

TG curves for the solvent cast layers dried at the three different temperatures are shown versus the as received PSu in Figure 3.13. The TG curves were used to measure the amount of solvent retained by the PSu films after drying at different temperatures. The amount of solvent is quantified in Table 3.2. The retained solvent data shows that a

Table 3.2 Weight percent solvent retained results for PSu layers fabricated at all three drying temperatures.

Drying Condition	Wt% Solvent Retained
PSu, As Delivered	< 1%
70° C	20%
150°C	10%
190°C	4%

significant amount of solvent is trapped within the PSu films until the films are heated past the  $T_g$  of the PSu at which point softening occurs and allows for diffusion of the remaining solvent out of the film. Tensile testing of these films which will be shown later in this chapter, proved that there was no benefit to increasing the drying temperature above 70°C. Therefore, it is reasonable to assume that the PSu layers of the laminates contain approximately 20 wt% solvent.

### **Consistency of Solvent Casting**

Once 70°C was selected as the drying temperature of the solvent cast PSu films, TG/DTA was run on six sample films cast at different times to see, qualitatively, how much variation there is in this solvent casting process. The six curves are shown in Figure 3.14. The solvent casting process shows good consistency with there being only a 4% difference between extremes. The TG data suggests that the solvent casting technique has sufficient reliability to assume that trends which arise during mechanical testing are a function of laminate behavior and not due to variations in the solvent casting technique.

### **TG/DTA Analysis of a Fractured PSu Layer**

One of the 400-200-800 laminates tested according to the parameters that will be discussed in the subsequent chapters has a fracture surface which demonstrated a considerable amount of delamination. Enough of a PSu layer was exposed to use for a TG/DTA run. Figure 3.15 is the curve that resulted from this run. The curve seems to confirm the idea that as the PSu layers dry, solvent segregated into small cavities or bubbles. The numerous drops in weight seen in the curve could possibly coincide with

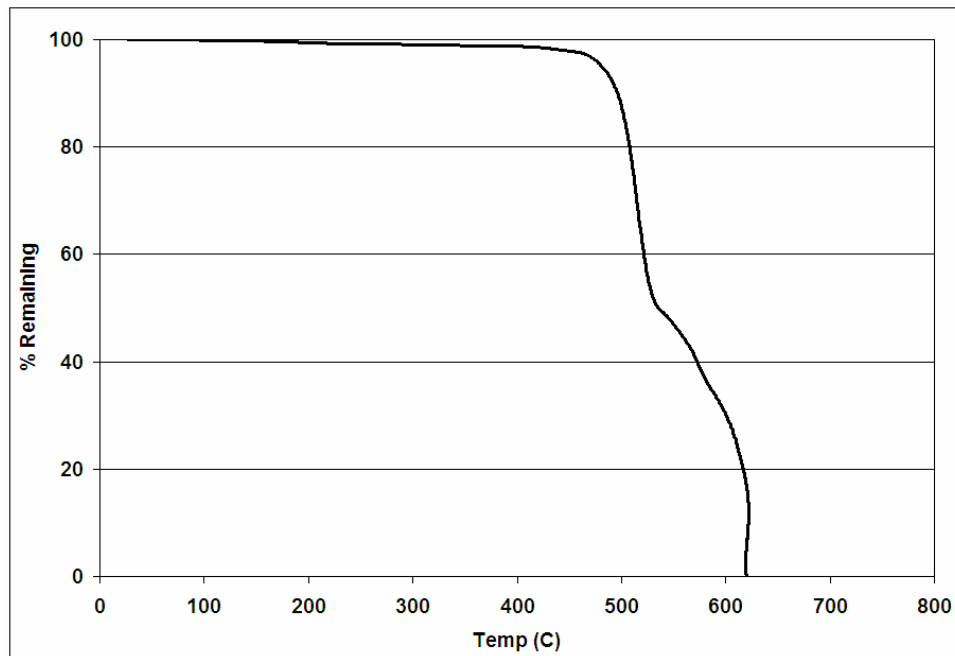


Figure 3.12 Complete TG curve for an as received PSu pellet.

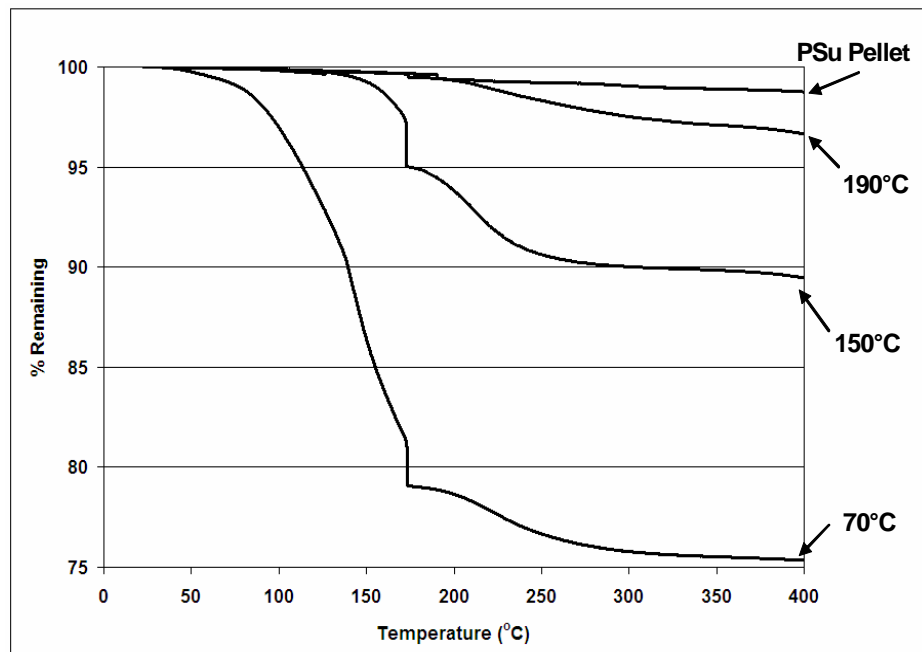


Figure 3.13 A comparison of TG curves PSu films dried at the three different temperatures.

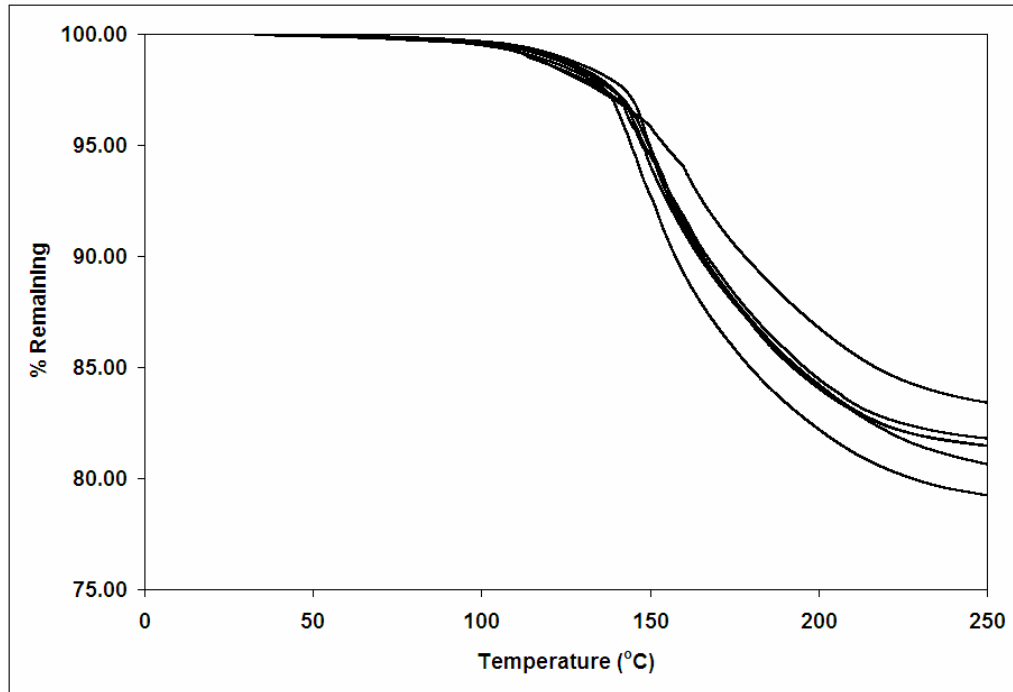


Figure 3.14 TG curves for six different PSu films dried at 70°C.

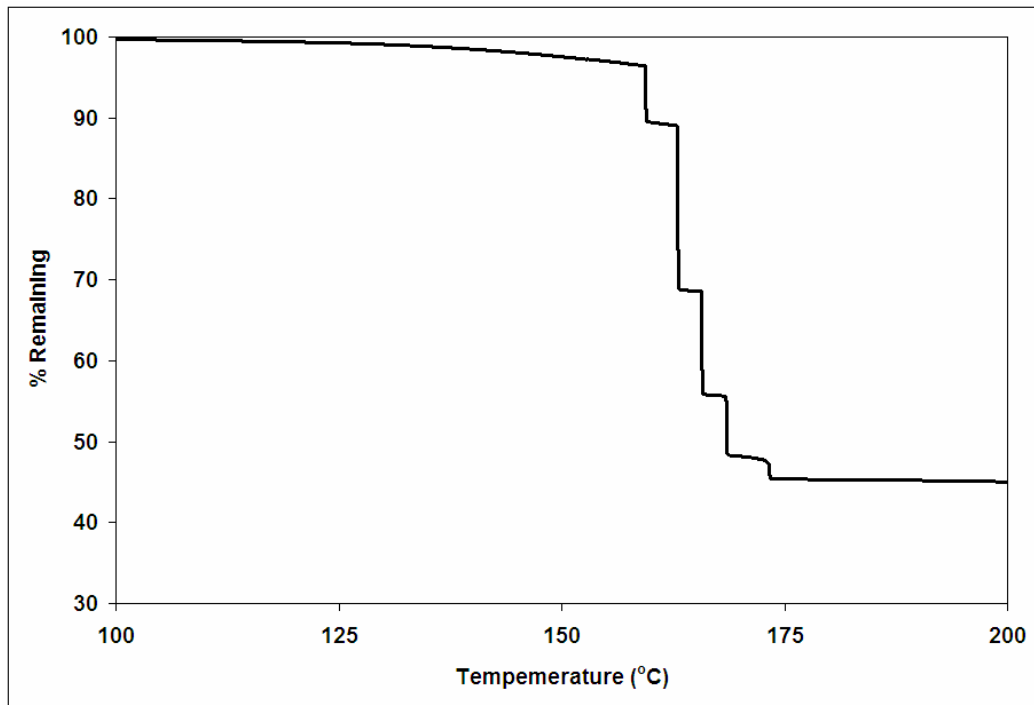


Figure 3.15 TG curve for a PSu sample taken from a delaminated region of a laminate fracture surface.

the release of solvents from different cavities. As the PSu sample is being heated in the TG/DTA, the outer surface of the PSu softens first with the middle softening last due to the principles of heat flowing into the system. The result is solvent pockets closer to the outer film surfaces are released first, followed by the pockets closer to the center. This behavior was not seen in prior testing because those films were cast onto glass slides, which produce more homogenous films. Solvent pockets would be more prevalent within the laminate layers because there is a second HA disc stacked on top of the drying film, which acts as an additional barrier preventing solvent from escaping into the environment.

Unfortunately, this data could not be reproduced as only this one sample was taken from an actual fracture surface. The value of the fracture surfaces is in explaining the failure mechanisms of the laminates, and for this reason, more layers were not tested in TG/DTA. The tested layer could possibly be nothing more than an anomaly, but the TG curve coupled with the SEM image, Figure 3.10, of numerous bubbles within the PSu laminate layers suggest that solvent segregation is occurring as has been described.

### **DSC Analysis of PSu Films**

DSC was performed on a PSu pellet and on a PSu film dried at 70°C. Three heating and cooling cycles were performed over the temperature range of 0 – 350 °C, with the polymer specimens in crimped aluminum pans. DSC curves generated for the PSu pellet are shown in Figure 3.16. The curves confirm that the as received PSu has a  $T_g$  around 180°C and is amorphous as there is no melting peak.

DSC curves generated for the PSu films are shown in Figure 3.17. The initial heating show an initial drop beginning at 50°C, which is consistent with the PSu pellet,

and a second drop that begins between 100-150°C. This second peak is the result of solvent evaporation that increases the pressure inside the crimped pan, which is read as an increase in heat. This has been shown to occur elsewhere when additives burnout of a polymer matrix. The result is the inability to get an accurate reading of the T<sub>g</sub> of the PSu films. Once the solvent has completely evaporated, the second heating and cooling curves are consistent with the as received PSu.

### **Tensile Testing of PSu Layers**

Tensile tests were performed on twenty-four total PSu specimens with eight specimens fabricated for each drying condition. The elastic modulus, stress at break, and elongation at break were compared for the three drying temperatures, Figures 3.18 – 3.20. There was no statistical difference ( $\alpha=0.05$ ) between the mechanical properties of PSu films prepared at each of the three drying temperatures. The tensile testing demonstrated that strength of the PSu layers were not directly influenced by the amount of residual solvent contained within the layers. These results are an indication of segregation between the polymer chains and solvent molecules. If the solvent molecules were dispersed within the PSu chain then they would affectively plasticizer the PSu and tensile testing would show the 70°C to be of a lower modulus, and a greater elongation at break would be seen.

### **Laminate Fabrication Effect on Biaxial Flexure Strength**

Laminates fabricated through each method were tested in biaxial flexure to establish which method and drying temperature would provide the greatest values for failure loads and failure stress. The process for calculation failure stress is detailed in the next chapter. Figure 3.21 shows the loads to failure measured during biaxial flexure and the

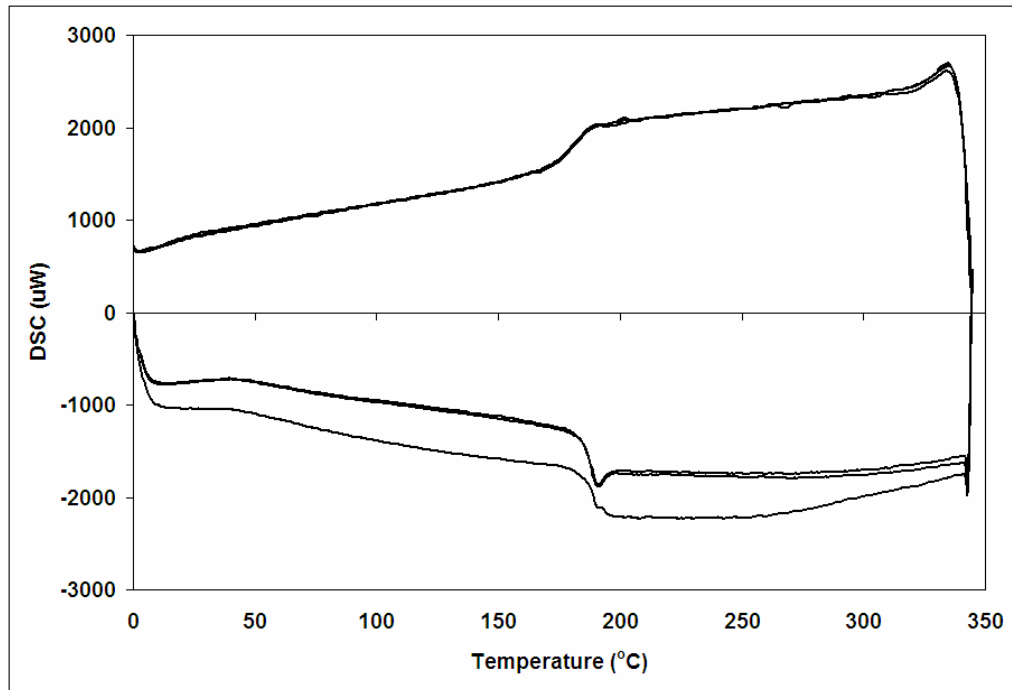


Figure 3.16 DSC curves generated through three heating-cooling cycles for an as received PSu pellet.

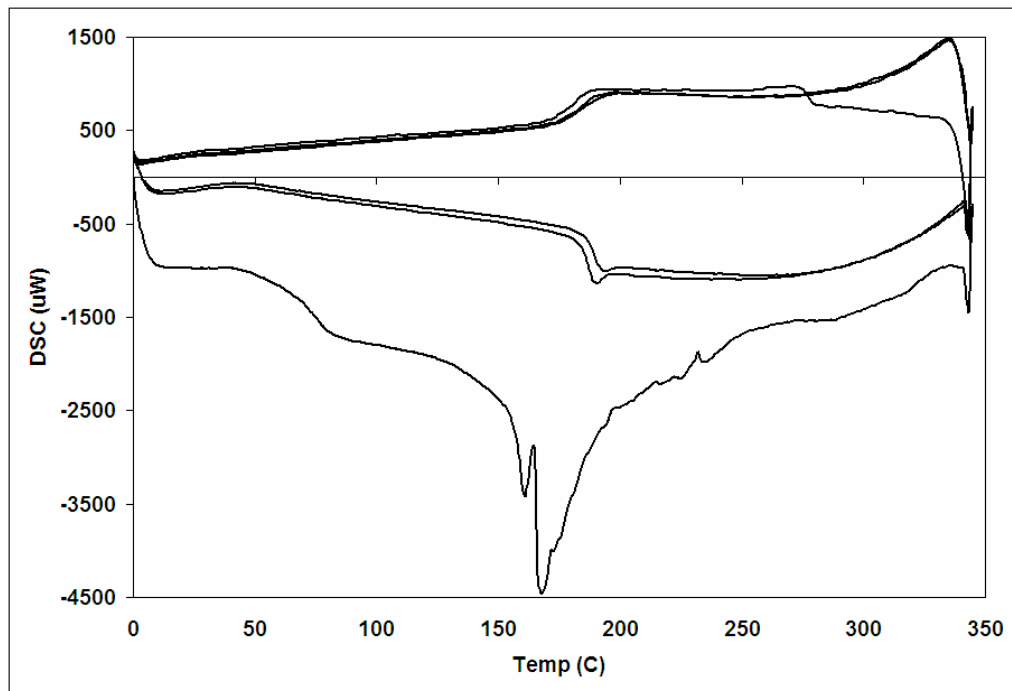


Figure 3.17 DSC curves generated through three heating-cooling cycles for a PSu film dried at 70°C.

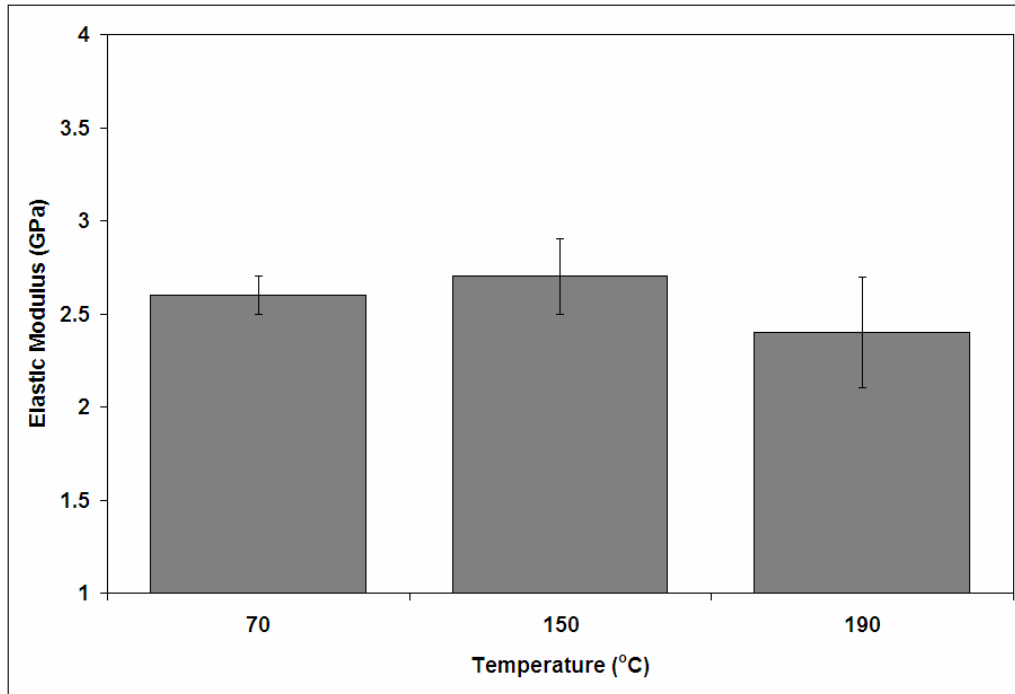


Figure 3.18 A plot of elastic modulus vs. drying temperature for PSu layers.

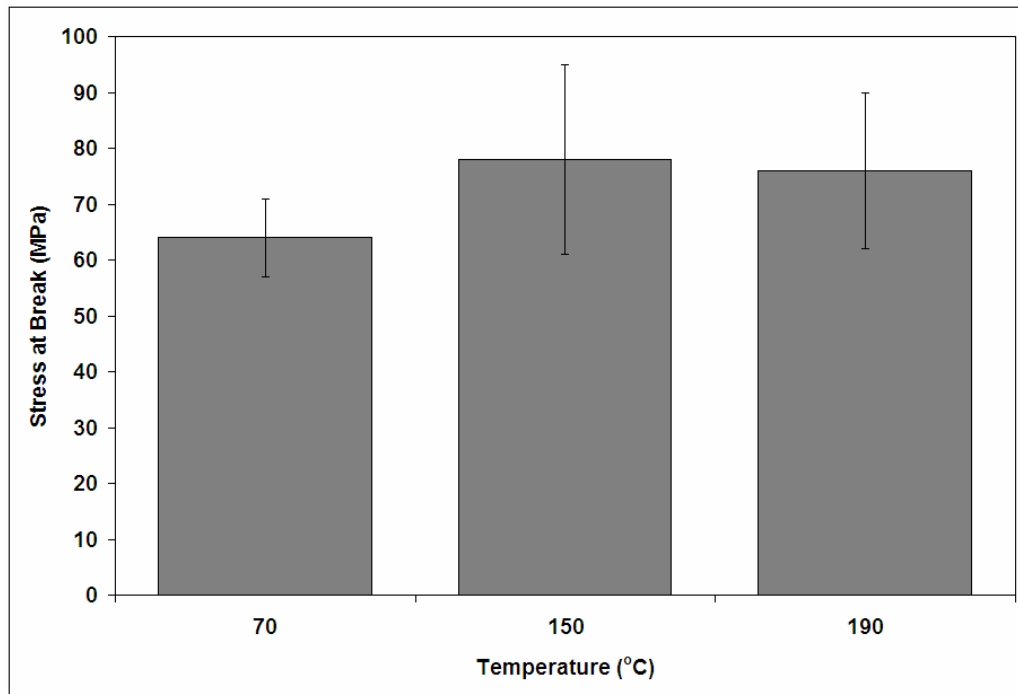


Figure 3.19 A plot of break stress vs. drying temperature for PSu layers.

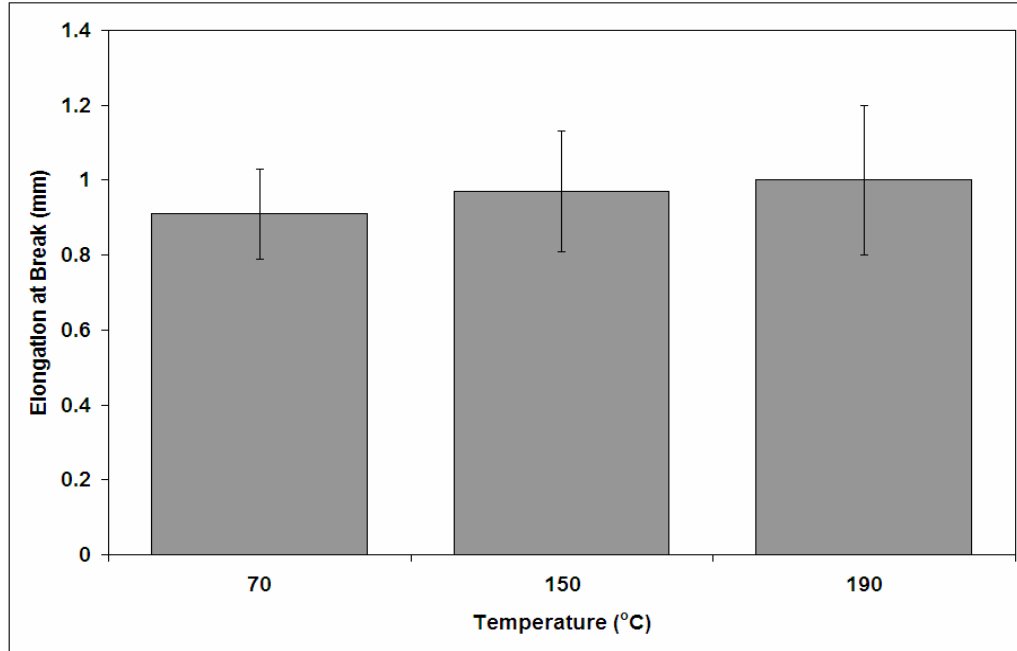


Figure 3.20 A plot of elongation at break vs. drying temperature for the PSu layers.

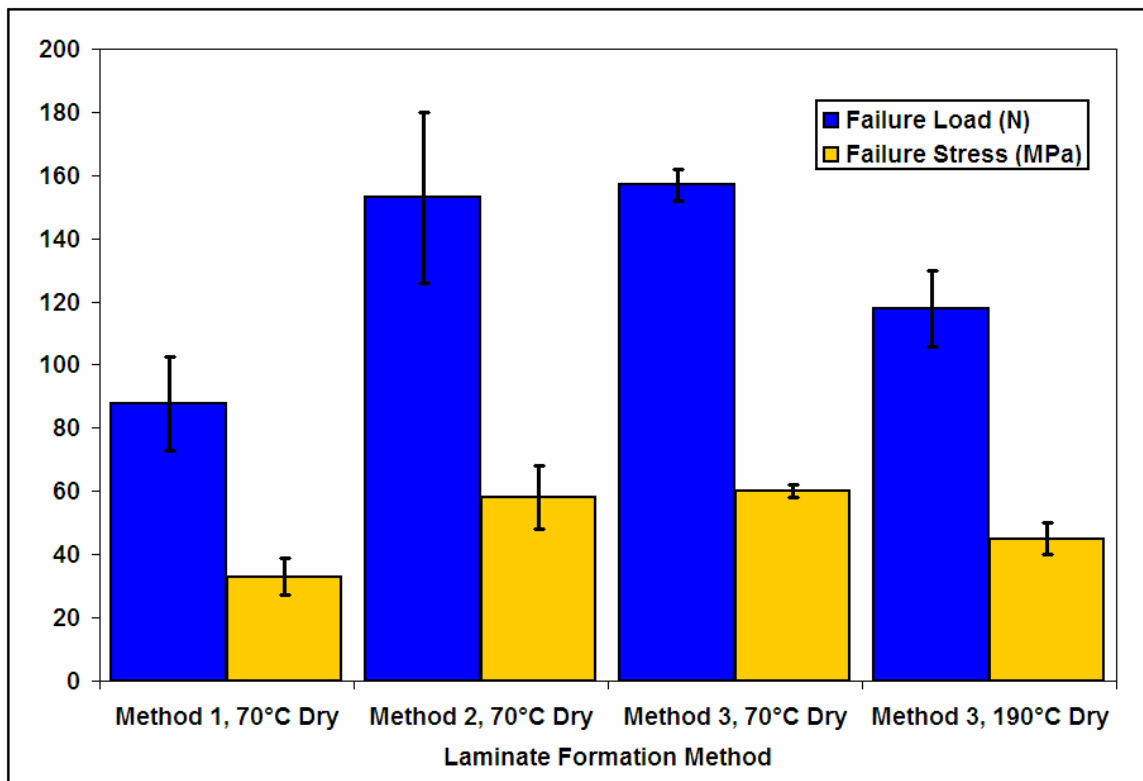


Figure 3.21 A plot of failure loads and stresses vs. laminate fabrication method and drying temperature. Units of the y-axis are different for each series.

corresponding failure stresses for the three laminate fabrication methods and for drying at 70°C and 190°C. Statistical analysis ( $\alpha=0.05$ ) showed no difference between the failure load and failure stress values for fabrication methods 2 and 3 dried at 70°C. Statistics showed that the load and failure values for these two methods were statistically different from the values for both method 1, the matching halves method, and for drying at 190°C. The biaxial flexure results indicate that fabrication through methods 2 and 3 yields laminates with similar failure loads and stress and are superior to those of laminate fabricated through method 1. The methods 2 and 3 failure loads and failure stresses, which are 175% of those for method 1. The lesser properties of the method 1 laminates are a result of the large cavities, which form within the PSu layers. Without the structural support of the PSu, the HA layers around the cavity regions are unable to sustain loads equivalent to those where the PSu is present. This is why only methods 2 and 3 were used for laminate fabrication in this study.

Results also suggest that drying at 70°C is preferable to drying at 190°C, with failure loads and stresses for the 70°C laminates being 130% of those for the 190°C laminates. This suggests that the greater residual solvent content of layers dried at 70°C drying is potentially beneficial to the mechanical properties of the laminates. The reason for better properties is that 70°C is below the boiling temperature of TCE (b.p. = 110°C) the drying process will be slow. As the TCE evaporates the viscosity of the PSu layer increases. With the slower drying process allows the PSu to maintain a lower viscosity longer, resulting in a greater depth of penetration into the HA discs. The greater penetration depth establishes a strong interface between the PSU and HA which are bonded through a

mechanical interlocking. These stronger interfaces allow for greater stress transfer to the PSu layers during loading and result in the increased failure loads over the 190°C drying.

### Middle Layer Surface Finish and Mechanical Properties

Biaxial flexure testing of six laminates prepared with middle HA layers finely polished prior to lamination were compared with data gained from testing of laminates which had been prepared with the rougher 600 grit finish. A comparison of failure loads and failure stresses is shown in Figure 3.22. Statistical analysis ( $\alpha=0.05$ ) showed that the values for failure loads and stresses for the two polishing methods were different, with

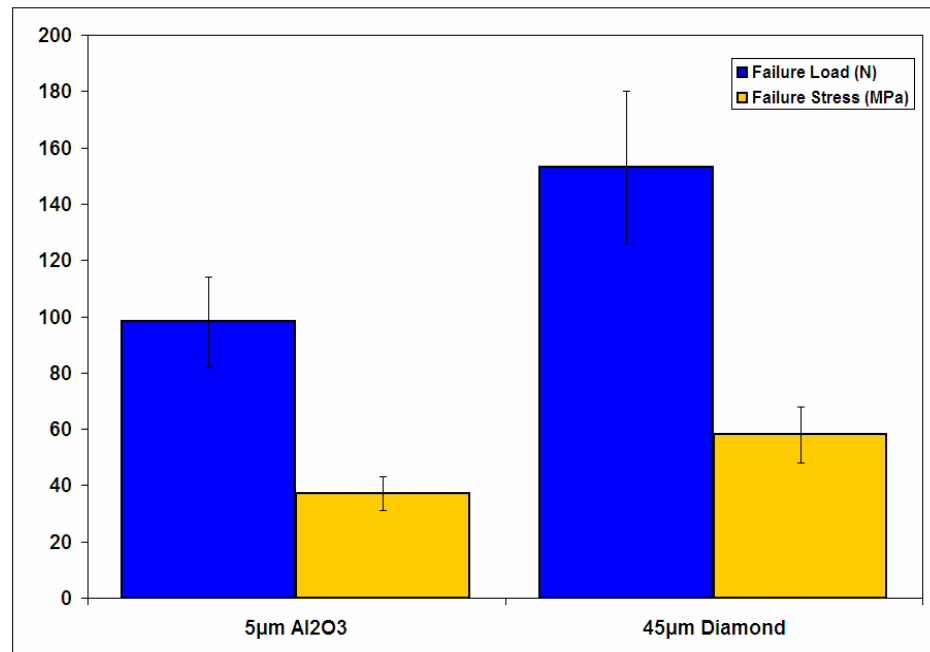


Figure 3.22 A plot of laminate failure loads and stresses vs. surface polishing medium. The ordinate axis has units are unique to each series plotted.

the 600 grit finishing having failure loads that were 150% of those laminates having the fine polished middle surfaces. Analysis of the fracture surfaces showed that the finer polished specimens delaminated occurred along entire HA/PSu interfaces which

compromised the mechanical stability of the laminate. Initial debonding along the HA/PSu interface was sufficient to cause the PSu layer to bow out, or buckle; opening a large gap between the PSu layer and the middle HA layer. This result indicates that bonding of the laminate is through mechanical interlocking and not through chemical means.

### **Comparison of PSu Laminate to sPSu Laminates**

A set of six laminates were fabricated with sPSu instead of PSu. Failure loads and stresses from loading in biaxial flexure are compared in table 3.3. The results show that there would be no benefit to using the sPSu without coupling agents, which could potentially strengthen the interface and change the mechanical behavior of the laminates. Since addition of coupling agents is not part of this study, no further testing of laminates with sPSu was performed.

Table 3.3 Comparison of laminates fabricated with polymer layers composed of both PSu and sPSu

Polymer	Failure Load (N)	Failure Stress (MPa)
PSu	150 ± 22	56 ± 8
sPSu	135 ± 15	50 ± 5

## CHAPTER 4 LAMINATE THEORY

### **Background**

#### **Stress Analysis for Laminated Discs**

No mathematical solution currently exists for converting experimental failure loads measured through biaxial flexure tests into stresses for laminated discs. There are only two used to calculate stresses for laminated discs. These are through attachment of strain gauges prior to testing [46] or through finite element modeling [47]. While these are effective ways for calculating stresses, they are more complex and time consuming than having a mathematical model. The strain gauge method requires experimental testing of specimens, and the finite element modeling requires access to modeling software, which can be expensive. For these reasons, a purely mathematical model, which could predict failure stresses and failure loads, is desired.

#### **Development of a Laminate Theory Solution**

A laminate solution will be developed for laminate discs loaded in biaxial flexure. Accomplishing this will be done through combining laminate theory derived for the bending of beams with bending moments derived for simply supported circular plates loaded at the center. Laminate theory as presented by Mallick [48] describes the bending mechanics for fiber-reinforced cross-ply laminate beams. This laminate theory can be applied to laminates that do not contain fibers by assuming that all fibers are of the same modulus as the surrounding matrix, and are aligned in the  $0^\circ$  direction. Making these two assumptions allows the laminate theory to describe the bending mechanics for laminate

beams made out of the materials selected for this study. However, since the experimental design calls for biaxial flexure of laminated discs, not beams, the bending moments used in the laminate theory must be changed to reflect this change in loading geometry.

Bending moments for simple supported circular plates loaded at the center as described by Timoshenko and Woinowsky-Krieger [49] were found to be the most applicable to the desired solution. Derivation of a laminate solution for the laminated discs using these two theories is presented in the following section. The final solution requires a six-step calculation to generate a stress profile for a laminate.

### **Verification of Laminate Theory**

The validity of the derived laminate solution will be verified through a comparison with finite element analysis run on identical laminate geometries. Agreement between the laminate theory and finite element models will demonstrate that a proper mathematical solution was derived.

## **Methods**

### **Laminate Theory**

A schematic of a laminate showing the variables necessary for laminate theory calculations can be found in Figure 4.1. The first step of the laminate theory is calculation of the stiffness matrix  $[Q]$  using equation 4.1 – 4.2[48]:

$$[Q] = \begin{bmatrix} Q_{11} & Q_{12} \\ Q_{21} & Q_{22} \end{bmatrix} \quad (4.1)$$

$$Q_{11} = Q_{22} = \frac{E}{1-\nu^2}, \quad (4.2a)$$

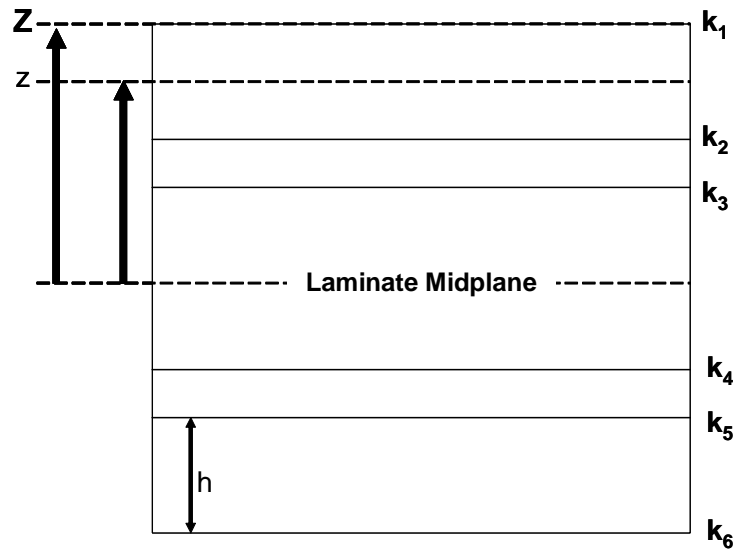


Figure 4.1 A schematic representation of a laminate indicating the mathematical variables required for laminate theory calculations.

$$Q_{12} = Q_{21} = \frac{\nu E}{1 - \nu^2} \quad (4.2b)$$

where  $E$  is the elastic modulus and  $\nu$  is Poisson's ratio of the particular lamina being analyzed. From this matrix, the bending matrix  $[D]$  can then be calculated through equation 4.3- 4.4[48]:

$$[D] = \begin{bmatrix} D_{11} & D_{12} \\ D_{21} & D_{21} \end{bmatrix} \quad (4.3)$$

$$D_{11} = D_{22} = \sum_{k=1}^{NL} \left( \frac{Q_{11(k)} h_{(k)}}{12} + Q_{11(k)} h_k z_{(k)}^2 \right) \quad (4.4a)$$

$$D_{12} = D_{21} = \sum_{k=1}^{NL} \left( \frac{Q_{12(k)} h_{(k)}}{12} + Q_{12(k)} h_k z_{(k)}^2 \right) \quad (4.4b)$$

and  $z$  = distance from the midplane of the laminate to the midplane of the  $k$ th layer, see

Figure 4.1. An equivalent value for the Poisson's ratio of the composite can be

calculated through equation 4.5:

$$\nu_{eq} = \frac{D_{12}}{D_{11}} \quad (4.5)$$

The next step in the solution is calculating the moments of inertia,  $M_r$  and  $M_t$ , through equations 4.6a and 4.6b respectively [49]:

$$M_r = -\frac{P}{4\pi}(1+\nu)\log\frac{a}{r} \quad (4.6a)$$

$$M_t = -\frac{P}{4\pi}\left[(1+\nu)\log\left(\frac{a}{r}\right) - (1-\nu)\right] \quad (4.6b)$$

where P is the applied load,  $\nu$  is Poisson's ratio for the composite equal to  $\nu_{eq}$ , a is the support radius, and r is the radial distance from the center of loading.

From the moments of inertia and the bending matrix, the curvatures,  $K_r$  and  $K_t$ , are calculated through the matrix multiplication of equation 4.7 [48]:

$$\begin{Bmatrix} K_r \\ K_t \end{Bmatrix} = [D]^{-1} \begin{Bmatrix} M_r \\ M_t \end{Bmatrix} \quad (4.7)$$

From the curvatures, the strains,  $\varepsilon_r$  and  $\varepsilon_t$ , are calculated through the matrix multiplication of equation 4.8[48]:

$$\begin{Bmatrix} \varepsilon_r \\ \varepsilon_t \end{Bmatrix} = Z \begin{Bmatrix} K_r \\ K_t \end{Bmatrix} \quad (4.8)$$

where Z is the distance from the laminate midplane to the tensile surface of the kth layer, and differs from the previous value for z.

Finally, from the strain values and the stiffness matrix [Q], the stresses,  $\sigma_r$  and  $\sigma_t$ , can be calculated through matrix multiplication, equation 4.9 [48]:

$$\begin{Bmatrix} \sigma_r \\ \sigma_t \end{Bmatrix} = [Q] \begin{Bmatrix} \varepsilon_r \\ \varepsilon_t \end{Bmatrix} \quad (4.9)$$

The entire laminate theory calculation was setup in a Microsoft Excel spreadsheet so that stress values could be gained immediately if any parameters needed to be changed. A sample sheet for the 400-200-800 laminate can be found in Figure 4.2.

### **Finite Element Analysis (FEA)**

Finite element analysis was performed by the research group of Dr. Bhavani Sankar in the Department of Mechanical and Aerospace Engineering of the University of Florida. FEA was performed using the computer program ABAQUS™, standard version 6.4-1. The model had 1533 nodes and 1440 total elements with 5 integration points throughout the element thickness. Each laminate layer had 4 elements in the thickness direction. The type of elements used was axisymmetry 3-D solid 4 node elements.

The FEA was performed to verify the accuracy of laminate theory calculations. The data gained from the FEA was a calculation of the maximum principal stress at the center of the tensile surface resulting from a 1 N load being applied, as it would be during loading in biaxial flexure. Figure 4.3 is an example of the graphical output gained from FEA analysis of a 1 N applied load being placed on a 400-400-800 HA/PSu laminate. The region showing the darkest red coloring on the bottom surface represents the area on the tensile surface of the laminate where the highest principal stress can be found.

### **Material Modeling Parameters**

A number of materials and testing parameters were made constant for modeling. Elastic modulus for HA and PSu were verified through previously described experiments at 52 GPa and 2.7 GPa respectively. Poisson's ratio for HA was 0.25 verified through ultrasound, while performing modulus measurements, and assumed to be 0.33 for PSu. Biaxial loading fixture dimensions for the support ring radius of 7.5 mm, and the loading piston radius of 1.1 mm were constant for both models.

Materials Parameters									
E (HA) =	5.20E+10	PA	v(HA)=	0.25	Lamina	h (m)	z (m)	Z (m)	
E (PSU) =	2.70E+09	PA	v(PSU)=	0.33	1	0.0004	0.00080	0.0010	
					2	0.0002	0.00050	0.0006	
					3	0.0004	0.00020	0.0004	
					4	0.0004	-0.00020	-0.0004	
					5	0.0002	-0.00050	-0.0006	
					6	0.0004	-0.00080	-0.0010	
					Total (mm)	2.00			
Q Matrix									
[Q] =	Q11	Q12							
	Q12	Q22							
Q11 (HA) =	$E/(1-\nu^2)$	$5.55E+10$	Pa						
Q11 (PSU) =	$E/(1-\nu^2)$	$3.03E+09$	Pa						
Q12 (HA) =	$\nu E/(1-\nu^2)$	$1.39E+10$	Pa						
Q12 (PSU) =	$\nu E/(1-\nu^2)$	$1.00E+09$	Pa						
D Matrix									
[D] =	D11	D12	D11=	$E((Q11(k)h(k)^3)/12) + Q11(k)h(k)z(k)^2$					
	D12	D11	D12=	$E((Q12(k)h(k)^3)/12) + Q12(k)h(k)z(k)^2$					
Lamina	1	2	3	4	5	6	Total		
D11	14.50	0.15	1.18	1.18	0.15	14.50	32	$v(eq) = D12/D11$	0.251
D12	3.62	0.05	0.30	0.30	0.05	3.62	8		
Moments									
a = (support piston radius =			0.0075	m					
r = (loading piston radius =			0.0002	m					
			<b>P = Load =</b>	<b>N</b>					
Mr =	$(P/4P)[(1+\nu(eq))\log(a/r)]$		0.16	N					
Mt =	$(P/4P)[(1-\nu(eq))\log(a/r)] - 1 - \nu(eq)$		0.22	N					
Curvature									
{K <sub>r</sub> } =	$[D]^{-1}$	{Mr}	$[D]^{-1} =$	1	D11	-D12 =	0.034	-0.008	
{K <sub>t</sub> } =		{Mt}		$D11^2 - D12^2$	-D12	D11 =	-0.008	0.034	
{K <sub>r</sub> } =	$D11^{-1}Mr + D12^{-1}Mt$		0.003	1/m					
{K <sub>t</sub> } =	$D11^{-1}Mt + D12^{-1}Mr$		0.006	1/m					
Strain									
Layer									
{ε <sub>r</sub> } =	Z	{K <sub>r</sub> } =	1	2	3	4	5	6	
{ε <sub>t</sub> } =		{K <sub>t</sub> } =	3.5E-06	2.1E-06	1.4E-06	-1.4E-06	-2.1E-06	-3.5E-06	
			6.0E-06	3.6E-06	2.4E-06	-2.4E-06	-3.6E-06	-6.0E-06	
Stress		Layer							
{σ <sub>r</sub> } =	[Q]{κ}	{ε <sub>r</sub> } =	1	2	3	4	5	6	
{σ <sub>t</sub> } =		{ε <sub>t</sub> } =	2.7E+05	9.9E+03	1.1E+05	-1.1E+05	-9.9E+03	-2.7E+05	
		In Mpa	3.8E+05	1.3E+04	1.5E+05	-1.5E+05	-1.3E+04	-3.8E+05	
			0.36	0.01	0.15	-0.15	-0.01	-0.36	

Figure 4.2 The Microsoft Excel spreadsheet designed to calculate the laminate stress distribution for the 400-200-800 laminate

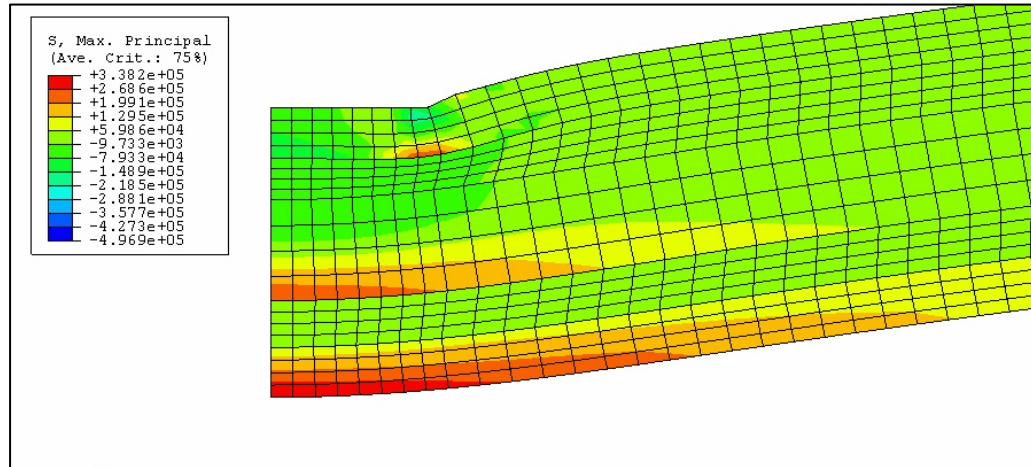


Figure 4.3 Graphical representation of the stress field resulting from a 1 N applied load on a 400-400-800 HA/PSu laminate.

## Results and Discussion

### Comparison of FEA and Laminate Theory Models

#### Monolithic HA Modeling

Modeling was performed for a monolithic HA specimens because this is the simplest design for comparison. The monolithic HA specimen was modeled with a thickness of 1.6 mm. The monolithic specimens could be modeled numerous ways through laminate theory. To demonstrate that the laminate theory solution developed was valid, the monolithic HA was modeled as both a symmetric bilayer and a 200-200-800 laminate. The solution for both models should yield the same value and be comparable to FEA. Thus, the FEA results would be used to validate applying the laminate model to the HA/PSu laminates.

#### Initial Model Comparison

The initial comparison of the laminate models, Table 4.1, indicated there was a discrepancy between the FEA solution and the laminate theory solution. The laminate theory underestimated the FEA value by 35%.

Table 4.1 Initial comparison of laminate models to FEA for monolithic HA.

Model	Maximum Principal Stress Resulting From a 1 N Load
FEA	0.51 MPa
Laminate Theory – Bi-layer	0.33 MPa
Laminate Theory – 400-200-800	0.33 MPa

### Correction of Laminate Theory

Many reasons for the discrepancy between the two models were analyzed. The discrepancy was ultimately in the position where the stress was being calculated by the laminate theory. It was assumed that the variable  $r$  in the moment of inertia equations, 4.6a and 4.6b, was the contact radius of the loading piston as it is for biaxial flexure, equation 2.8. However,  $r$  is actually the radial distance from the center of loading at which the stress value is calculated. Therefore, the radius of the loading piston in equations 4.6a and 4.6b was converted to a value of 0.2 mm, which proved to be the value that brought the laminate theory and FEA into agreement. A new comparison of the models, Table 4.2, yielded values that were identical for all three models.

Table 4.2 Comparison of corrected laminate models to FEA for monolithic HA.

Model	Maximum Principal Stress Resulting From a 1 N Load
FEA	0.51 MPa
Laminate Theory - Bilayer	0.51 MPa
Laminate Theory – 400-200-800	0.51 MPa

### Modeling of Laminates

The corrected laminate model was shown to be accurate for calculating stresses for the monolithic HA. It was then tested for its accuracy in describing the behavior of

HA/PSu laminates. Eight laminate geometries were modeled through FEA for comparison with the laminate theory. The laminate geometries chosen would all be fabricated and tested experimentally. These particular geometries were selected because they represented a wide range of total laminate thicknesses, ratios between the thicknesses of the individual layers, and composite moduli, which were calculated using the rule of mixtures. The contact field radius was kept constant at 0.2 mm, as this corrected value was established through the monolithic HA calculations. The results for the selected geometries are shown in Table 4.3. A negative % difference indicates an underestimate by the laminate theory, while a positive % difference means an

Table 4.3 Comparison of maximum principal stress calculated through FEA and Laminate Theory for various laminate geometries.

Laminate Geometry	Composite Modulus (GPa)	Total Thickness (mm)	FEA (MPa)	Laminate Theory (MPa)	% Difference
400-200-800	42	2.0	0.41	0.38	- 7%
400-50-800	44	1.8	0.48	0.47	- 2%
100-200-800	37	1.4	1.09	1.14	+ 5%
200-200-800	40	1.6	0.69	0.70	+1 %
100-100-1600	47	2.0	0.41	0.41	0%
350-400-500	32	2.0	0.52	0.43	- 17%
400-400-800	36	2.4	0.34	0.30	- 12%
200-400-800	32	2.0	0.55	0.56	2%

overestimation. On the average, laminate theory underestimated the stress from a 1N load by -3% from the FEA stress value. However, considerable differences exist for the 350-400-500, and 400-400-800 laminate geometries.

In order for each laminate theory calculation to agree with FEA the radial contact distance,  $r$ , was varied until the correct value was established which brought the laminate theory into agreement with the FEA. The corrected radial distance for each laminate group is shown in Table 4.4. The results show that 0.2 mm is a good approximation for the contact radius for all laminate groups except the 350-400-500 and 400-400-800 groups.

Table 4.4 Contact stress field radii for each laminate geometry that yields the same results as the FEA

Laminate Geometry	Composite Modulus (GPa)	Total Thickness (mm)	FEA (MPa)	Laminate Theory (MPa)	Corrected Radial Distance (mm)
Monolithic HA	52	2.0	0.51	0.51	0.20
400-200-800	42	2.0	0.41	0.41	0.14
400-50-800	44	1.8	0.48	0.48	0.18
100-200-800	37	1.4	1.09	1.09	0.25
200-200-800	40	1.6	0.69	0.69	0.22
100-100-1600	47	2.0	0.41	0.41	0.19
350-400-500	32	2.0	0.52	0.52	0.07
400-400-800	36	2.4	0.34	0.34	0.10
200-400-800	32	2.0	0.55	0.55	0.22

The origin for the discrepancy of the 350-400-800 and 400-400-800 group is not known for certain. No relationship or equation could be derived from the composite modulus, total thickness, or laminate geometries, which would yield the radial distance that correlates the FEA solution to the laminate theory solution. One hypothesis is that the FEA does not properly model the viscoelastic nature of the PSu. The FEA assumes a well-bonded material and looks at each layer only as they affect the overall global

behavior of the system. It would therefore be possible that the FEA over estimates the deflection resulting from the 1N load. Greater deflection would result in a greater principal stress at the center of the tensile surface. The laminate theory calculation deals with the stiffness of each layer separately taking into account the contribution of each layer on a more localized scale. The localization of the laminate theory versus the global properties predicted by the FEA may be the reason for the discrepancies that arise with the thicker PSu layers. Without a proven way of calculating the adjusted value for the contact radius of the loading piston the value of 0.2 mm was applied to all laminate theory calculations because the average discrepancy is only -3% and, at worst, this approximation leads to an underestimation of the failure stresses for the laminates with thicker PSu layers.

### **Laminate Stress Distribution**

One advantage of laminate theory is the ability to quantify stresses at any point within the laminate. This is done by adjusting the value of  $Z$ , which is the distance from the midplane of the laminate to the location where the stress value is desired, making it possible to derive a picture of the stress distribution throughout the entire laminate. The stress distribution for the 400-200-800 laminate is shown in Figure 4.4. The stress distribution shows that the applied force is linear across all three HA layers and the two PSu layers, but is discontinuous at the interface between the HA and PSu. This stress distribution results from the lower elastic modulus of PSu compared to HA. A 1N load applied to the laminate results in deflection of the laminate. This deflection is quantified in terms of a uniform strain on the laminate. If each layer is assumed to behave

according to Hooke's Law [35],  $\sigma = E\varepsilon$ , the same strain results in a greater stress felt within the higher modulus layers.

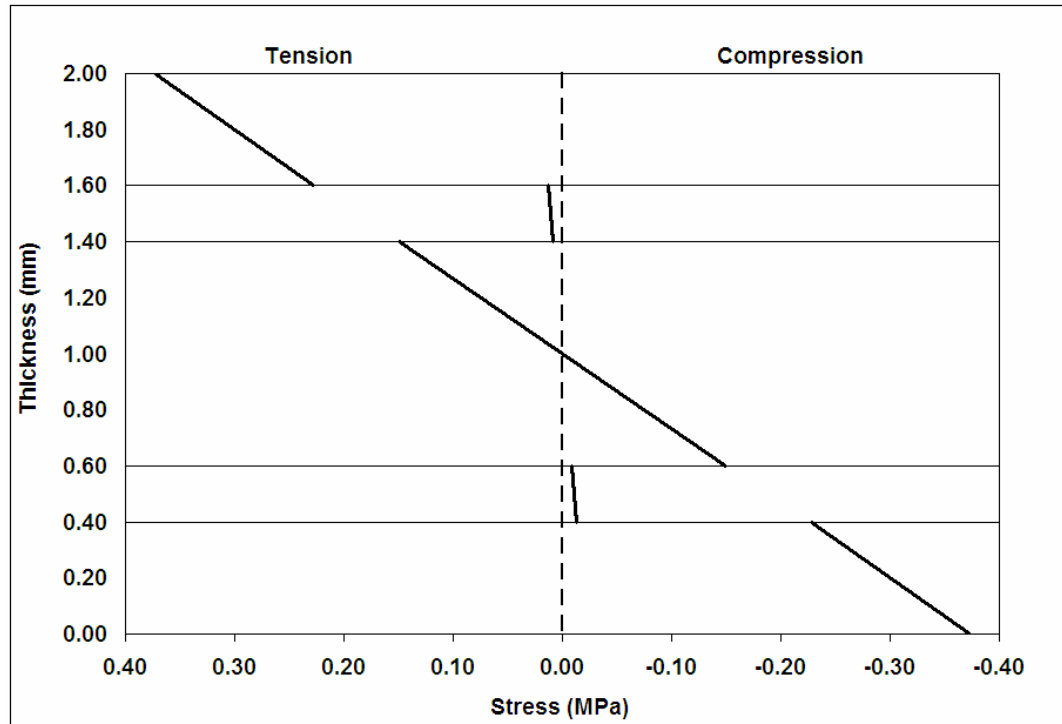


Figure 4.4 Stress distribution calculated using laminate theory resulting from a 1N load applied to a 400-200-800 laminate. Laminate layers are drawn to scale, with the 2.00 thickness representing the outer HA layer tensile surface.

## Predicting Laminate Behavior

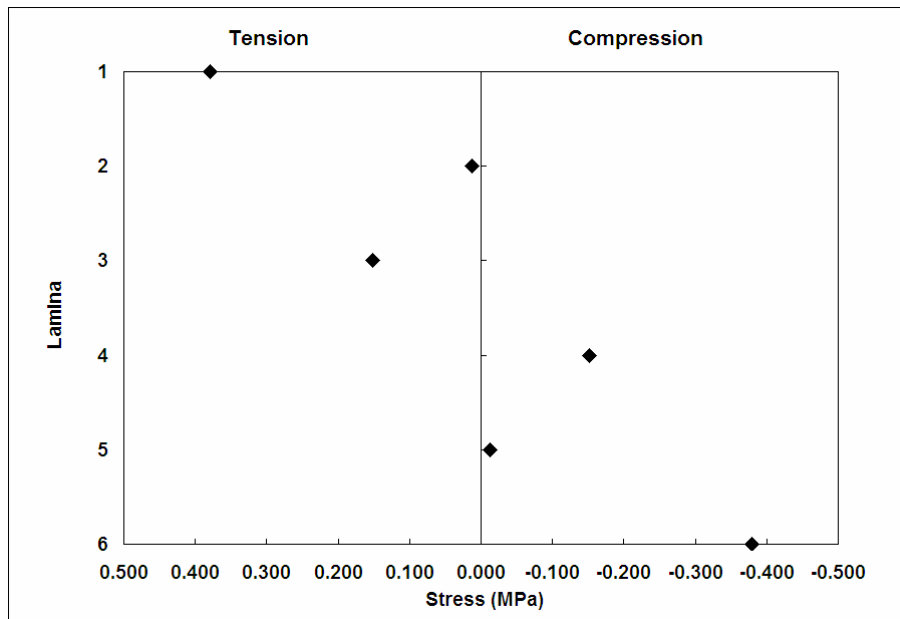
### Maximum Stresses

Laminate stress distributions were refined for comparison of different laminate geometries. Six data points were plotted for each laminate geometry modeled using the laminate theory, Figure 4.5 (a). Three points were for the maximum tensile stresses found for the outer HA layer on the indent side of the laminate, the PSu layer on the tensile side of the laminate, and for the tensile side of the middle layer. The other three points were for the maximum compressive stresses of the middle HA layer, the second

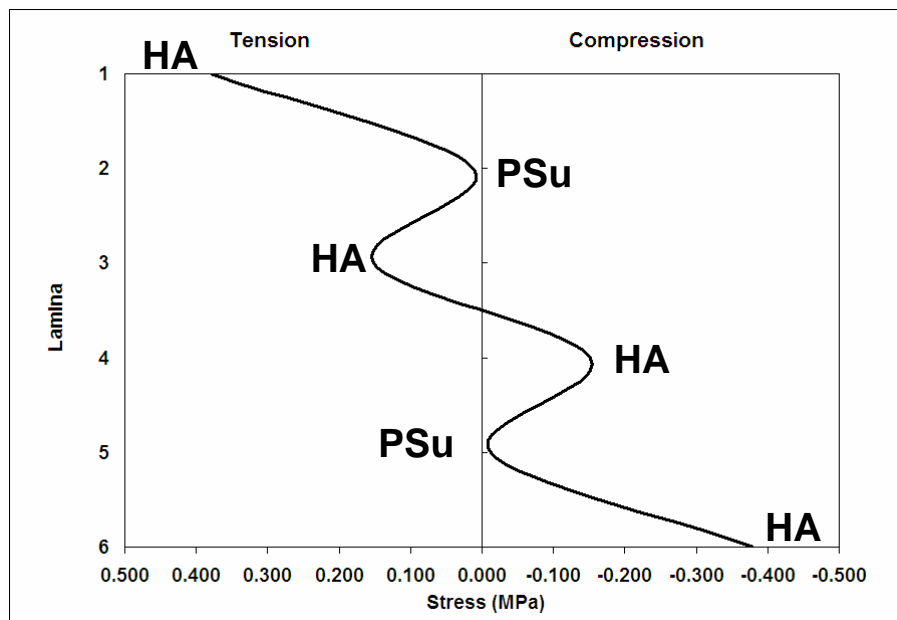
PSu layer, and the outer HA layer in contact with the loading piston. These points were then connected, generating a smooth curve, Figure 4.5 (b), which shows how the stress values changed from layer to layer. To avoid confusion it should be pointed out that this is not the same as the stress-distribution curve shown in Figure 4.4. This graph shows how stress values change between the individual layers of the laminate. These two plots contain entirely different information. A graph like this one was generated for all laminate geometries. Selected curves were drawn on the same graph in order to compare the stresses for different laminate geometries.

### **Comparison of Maximum Stress Curves**

Stress curves were graphed for all laminates in order to see if the laminate theory matched the experimental behavior of the laminates, and could thus be used as a predictive tool. Experiments were designed to test the effect of each layer on the mechanical behavior for the laminates. Stress curves were generated to show the effect of changing the thickness of the PSu layers (Figure 4.6), the outer HA layers (Figure 4.7), and the middle HA layer (Figure 4.8). Laminate theory was also used to generate stress curves for different laminate geometries with a constant thickness of 2 mm (Figure 4.9), to see which laminate geometry produced the minimum stress value. The six stress values of all of the laminate geometries tested experimentally are shown in Table 4.5. It was predicted that the laminate with the minimum stress value at the middle layer would result in the highest experimental failure loads. Trends the stress curves will be compared with experimental data in the laminate behavior chapter.



(a)



(b)

Figure 4.5 Maximum stresses for the 400-200-800 laminate as (a) a plot of individual points and (b) a graphed smoothed curve.

### Maximum Tensile Stress and Lamina Ratios

Laminate theory could also predict the effect of individual layer ratios on the maximum stress at the tensile surface. Total laminate thickness was held constant at 2 mm. One additional layer was held constant while the thicknesses of the remaining two layers were varied. Stresses were plotted versus the ratio of the two varied layers.

With the middle HA layer thickness held constant at 800  $\mu\text{m}$ , the thicknesses of the outer HA and PSu layers were tested over a range of 0 – 600  $\mu\text{m}$ . Layer thicknesses were varied according to the equation  $(2 \times \text{Outer HA thickness}) + (2 \times \text{PSu layer thickness}) = 1200 \mu\text{m}$ . The resulting plot, Figure 4.10, showed the greatest stress values for the thinnest HA layers with stress values decreasing towards an asymptotic value of 0.32 MPa. 0.32 MPa value represents the stress from a 1 N load applied to a 2.0 mm monolithic HA specimen. This plot will be compared with experimental data in the next chapter to show the predictive capabilities of the laminate theory.

If the PSu layer is given a constant thickness of 200  $\mu\text{m}$ , and the thickness of the HA layers varied according to the equation  $(2 \times \text{Outer HA thickness}) + \text{Middle HA thickness} = 1600 \mu\text{m}$ . The thickness of the outer HA layer ranged from 0 – 800  $\mu\text{m}$  corresponding to the middle HA layer thickness of 1600 – 0  $\mu\text{m}$ . A plot of the outer HA thickness to middle HA thickness ratio versus stress, Figure 4.11, shows decreasing stress values towards the asymptotic value of 0.32 MPa. This plot will also be compared with experimental data in the next chapter.

Finally, the outer HA layer was held constant at 400  $\mu\text{m}$ , and the thickness of the middle HA layer and the PSu layer were varied according to the equation  $(2 \times \text{PSu thickness}) + \text{Middle HA thickness} = 1200 \mu\text{m}$ . The thickness of the PSu layer ranged

from 0 – 600  $\mu\text{m}$  corresponding to middle HA layer thickness of 1200 – 0  $\mu\text{m}$ . The plot of PSu:Middle HA ratio versus tensile stress, Figure 4.12, showed an initial increase from the monolithic HA stress value of 0.32 to constant value of 0.41 MPa. This plot will also be compared to experimental values in the next chapter.

The ratio comparison show that contribution of the PSu layer to mechanical properties is dependent upon the thickness of the outer HA layer. When the HA layer was held constant at 400  $\mu\text{m}$  there is only a 9% difference in the maximum tensile stress

Table 4.5 Maximum stresses on the tensile surface of each layer for all laminate geometries experimentally tested in this study.

Laminate Geometry	Outer HA Layer - Tensile Side	PSu Layer - Tensile Side	Middle HA Layer - Tensile Side	Middle HA Layer - Compression Side	PSu Layer - Compression Side	Outer HA Layer - Compression Side
400-200-800	0.38	0.01	0.15	-0.15	-0.01	-0.38
400-50-800	0.47	0.01	0.22	-0.22	-0.01	-0.47
400-100-800	0.44	0.01	0.19	-0.19	-0.01	-0.44
100-200-800	1.14	0.06	0.65	-0.65	-0.06	-1.14
200-200-800	0.70	0.03	0.35	-0.35	-0.03	-0.70
100-100-1600	0.41	0.02	0.33	-0.33	-0.02	-0.41
100-200-1400	0.51	0.03	0.36	-0.36	-0.03	-0.51
200-100-1400	0.39	0.02	0.27	-0.27	-0.02	-0.39
200-200-1200	0.56	0.02	0.31	-0.31	-0.02	-0.56
400-400-800	0.30	0.01	0.10	-0.10	-0.01	-0.30
350-400-800	0.43	0.02	0.11	-0.11	-0.02	-0.43
200-400-800	0.56	0.03	0.22	-0.22	-0.03	-0.56

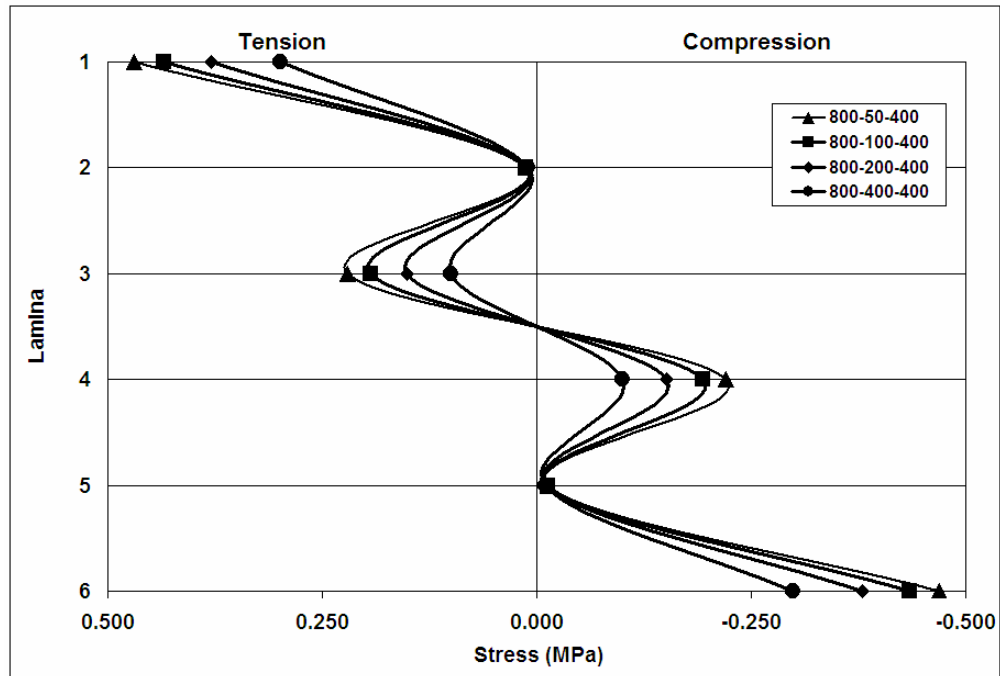


Figure 4.6 Maximum stress curves for laminates as a function of varying polymer layer thickness.

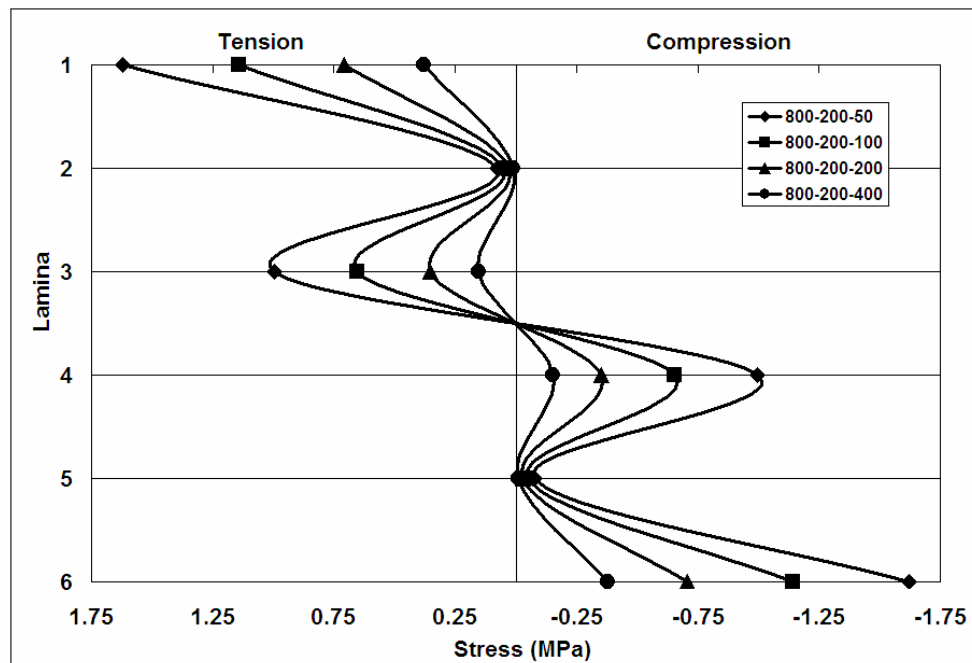


Figure 4.7 Maximum stress curves for laminates as a function of varying outer HA layer thickness.

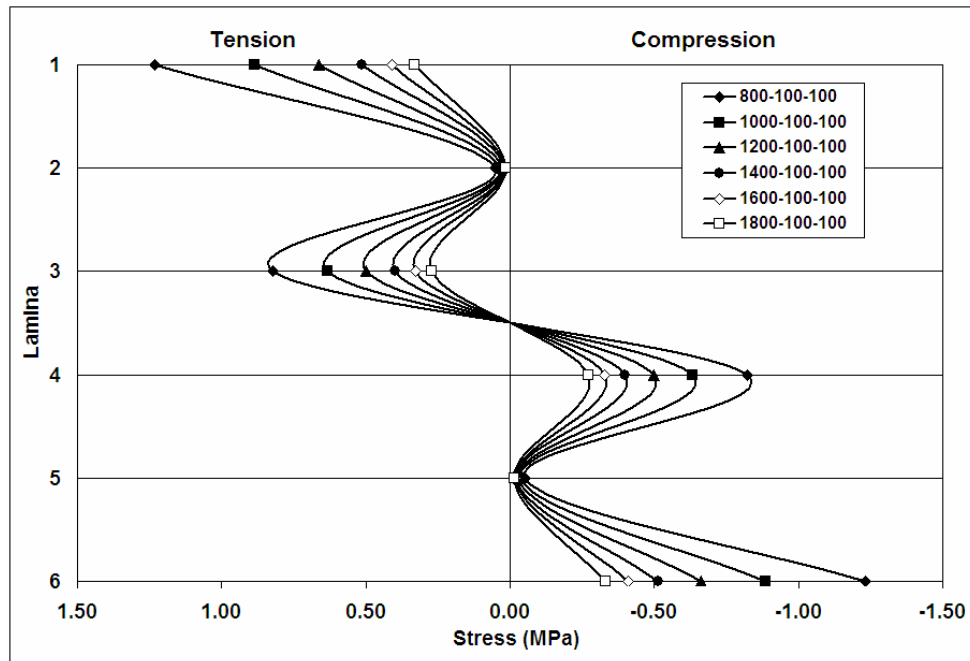


Figure 4.8 Maximum stress curves for laminates as a function of varying middle HA layer thickness.

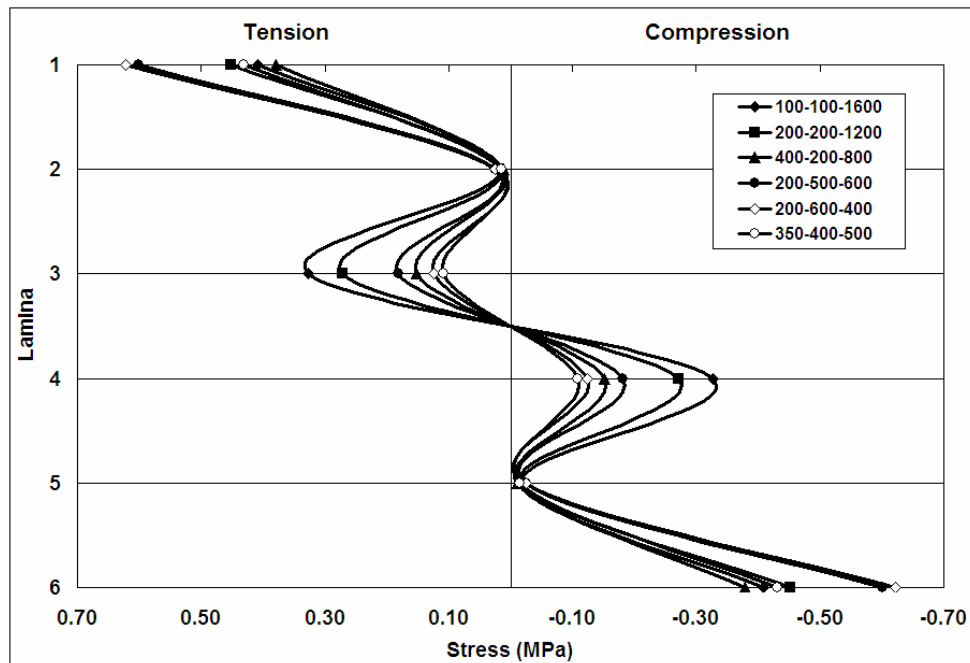


Figure 4.9 Maximum stress curves for various laminate geometries having a total laminate thickness of 2.0 mm.

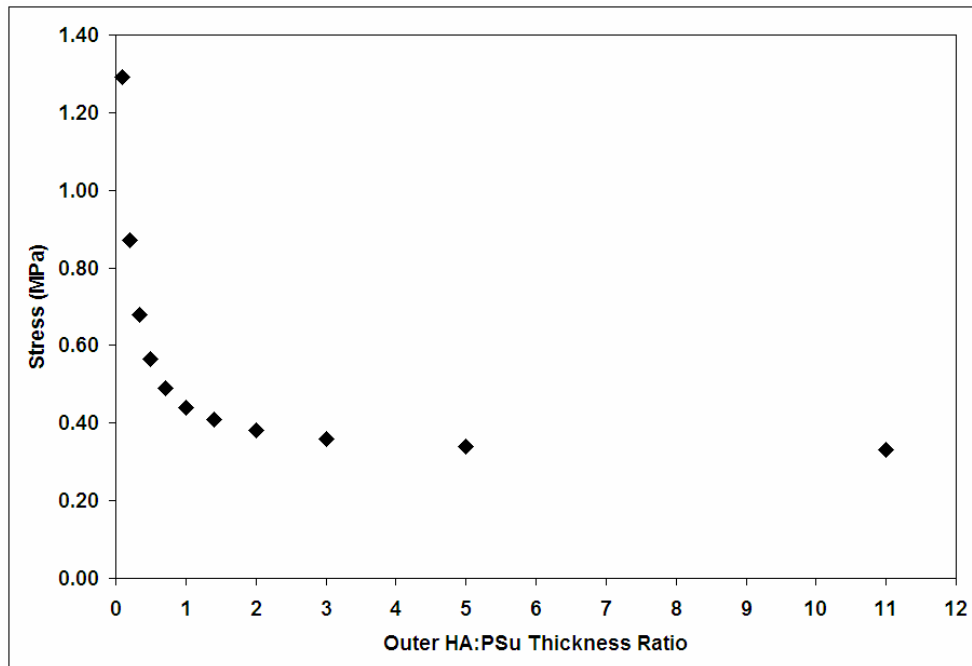


Figure 4.10 A plot of maximum tensile stress values versus the ratio between the thicknesses of the outer HA and PSu layers.

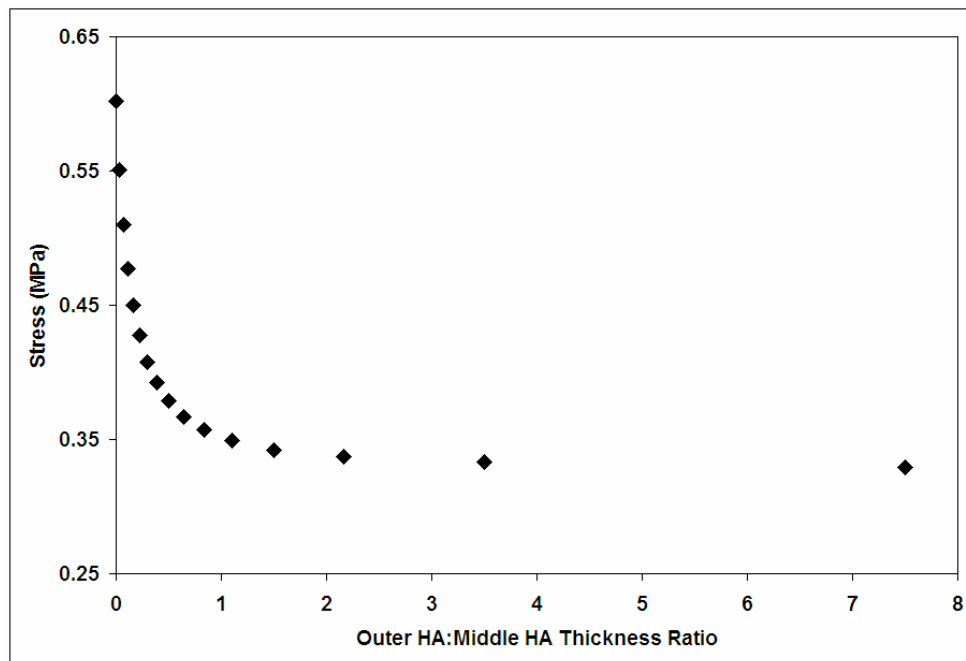


Figure 4.11 A plot of maximum tensile stress versus the ratio of thicknesses between the PSu and middle HA layers.

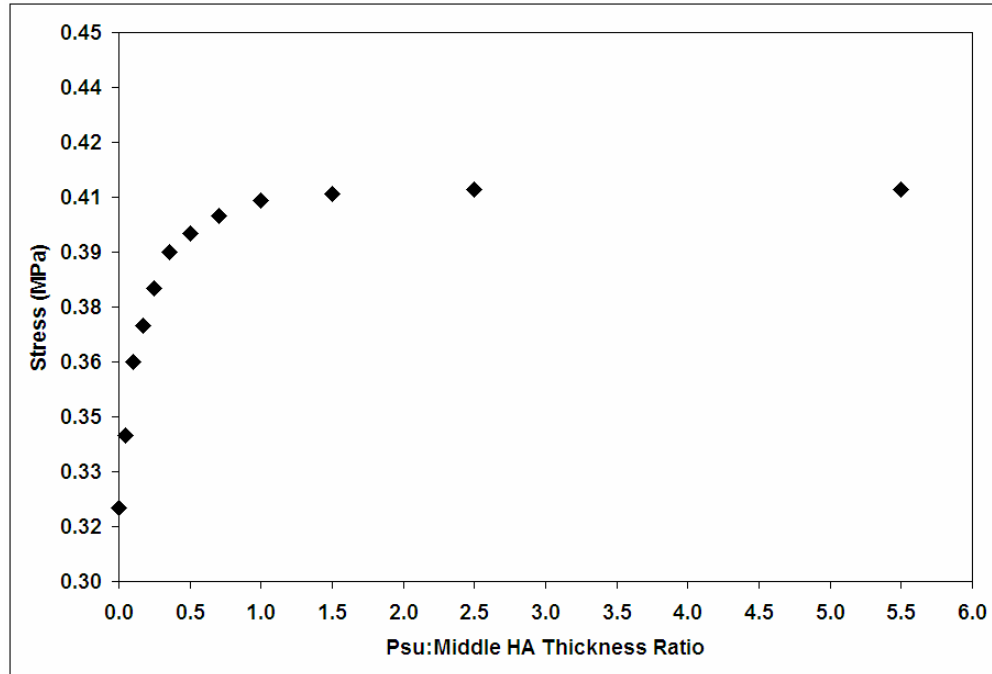


Figure 4.12 A plot of maximum tensile stress versus the ratio of thickness between the outer and middle HA layers.

value for the most extreme PSu layer thicknesses. However, when the outer HA layer to PSu layer ratio is  $< 2$  the PSu layer has a significant impact on the maximum tensile stress value. An impact becomes increasingly meaningful as this ratio is decreased further. Thus, the ratio analysis reveals that there is a finite range over which the PSu will have the most significant impact on mechanical behavior

## CHAPTER 5 LAMINATE BEHAVIOR

### Methods

#### Mechanical Testing and Characterization of Laminates

##### Indentation

As with the monolithic HA specimens, laminates were indented with Vickers indents prior to loading. The Vickers indent impressions were measured for calculating hardness values using equation 2.8. Hardness values similar to the monolithic HA would indicate good mechanical stability of the laminate, as there would be no deflection of the outer HA layer due to the lower modulus polymer below. For laminates with very thin outer HA layers, larger Vickers impressions were expected as indentation was effectively taking place on the low modulus PSu.

##### Biaxial Flexure

All laminate specimens were loaded to failure using the piston-on-three ball biaxial flexure fixture described previously in the Methods section of Chapter 2. The failure stress,  $\sigma_f$ , for the laminates was determined using the equation:

$$\sigma_f = P \times \sigma_{LT}$$

where P is applied load in Newtons measured experimentally, and  $\sigma_{LT}$  is the maximum principal stress (MPa/N) calculated using laminate theory. Since the laminate theory solution calculates both the stresses and strains for the laminates, stress-strain curves were generated from the applied loads measured during biaxial flexure tests.

### **Work of Fracture**

Work of fracture for the laminates was calculated using Equation 2.11. This same process was used for calculating the work of fracture for the monolithic HA samples. Projected fracture surface areas were calculated assuming rectangular cross-section, and depended on the number fracture pieces generated as described in Chapter 2. The work of fracture has units of  $J/m^2$ .

### **Toughness**

Toughness calculated from the areas under the stress-strain curves, and Equation 2.10, could be called the absorbed energy at fracture. In order for this value not to be confused with fracture toughness, the toughness calculated from the area under the stress-strain curve will be referred to as the absorbed energy at failure. The stress-strain curves used were generated from the experimentally measured applied loads through the laminate theory solution that has been developed. This is the same calculation used for the monolithic HA specimens. Absorbed energy at fracture has units of  $J/m^3$ .

### **Laminate Testing Variables**

#### **Testing Rationale**

After an initial comparison of mechanical properties between 400-200-800 laminates and monolithic HA, a number of different laminate geometries and design variables were tested to aid in explaining the mechanical behavior of the laminates.

#### **Loading Parameters**

Except where it is specified to the contrary, laminates were indented with the same Vickers indent load prior to loading in biaxial flexure. The indent load used was 3.35 kg. Except for the loading rate testing, all biaxial flexure loading was performed at a crosshead displacement rate of 2.5 mm/min.

**Initial Flaw Size**

The effect of the initial flaw size of the outer HA layer was tested by indenting four groups of laminates with a range of indent loads prior to loading in biaxial flexure. Laminates used for these testing groups had geometry of 400-200-800, with testing groups consisting of 6-7 laminates. The four Vickers indent loads selected were 0, 1.35, 3.35, and 9.35 kg. Laminates were tested in biaxial flexure at a crosshead displacement rate of 2.5 mm/min.

**Loading Rate**

The effect of the viscoelastic PSu layers on laminate behavior was tested by loading groups of laminates at different crosshead displacement rates. All laminates were indented using a 3.35 kg Vickers indent load prior to loading in biaxial flexure. Four groups consisting of 5-7 laminates were tested at crosshead displacement rates of 0.025, 0.25, 2.5 and 25 mm/min. Laminates had a geometry of 400-200-800.

**Polysulfone Layer Thickness**

The effect of the PSu layer on the strength and toughness of the laminates was tested by fabricating laminates with a range of PSu layer thicknesses. The outer and middle HA layers were fabricated to constant thicknesses of 400 and 800  $\mu\text{m}$  respectively. Laminate groups were fabricated with four different PSu layer thicknesses. The selected thicknesses of the PSu layers were 50, 100, 200, and 400  $\mu\text{m}$ .

**Outer HA Layer Thickness**

The effect of the outer HA layer thickness on the mechanical behavior of the laminates was tested by fabricating laminate groups with three different outer HA layer thicknesses. The PSu and middle HA layers were fabricated with constant thicknesses of

200 and 800  $\mu\text{m}$  respectively. The three outer HA layer thicknesses tested were 100, 200, and 400  $\mu\text{m}$ .

### **Middle Layer Thickness**

The effect of middle HA layer thickness on the mechanical behavior of the laminates was tested by fabricating four laminate groups with varying middle layer thicknesses. The total thickness of the laminates was held constant at 2.0 mm. The geometries of the four laminate groups were 100-100-1600, 200-200-1200, 200-100-1400, and 100-200-1400.

### **Highest Predicted Failure Load Specimens**

Two additional laminate groups were fabricated and tested. These laminate groups had geometries of 350-400-500, and 200-400-800. These geometries represented the laminate groups that were predicted to have the highest failure loads by the laminate theory model and the maximum stress curves for laminates with a total thickness of 2.0 mm, see Figure 4.8. The prediction is based on the assumption that crack propagation through the outer HA layer will be arrested at the HA/PSu interface. The loads required to reinitiate crack propagation through the middle HA layer is predicted by the stress/N load at the tensile surface of the middle HA layer calculated using laminate theory. The lesser the stress/N value the greater the applied load must be to produce stresses large enough to initiate crack propagation.

## **Results and Discussion**

### **Comparison of Laminates to Monoliths**

Initial testing of laminate behavior was performed on a group of seven laminates with geometry of 400-200-800. The mechanical properties of these laminates are

compared to monolithic HA specimens of the same thickness (see Chapter 2). All indentation and biaxial flexure testing were performed using the same parameters for the laminates as were used for the monoliths.

The hardness of the laminates was calculated at  $1.32 \pm 0.17$  GPa. Statistical analysis ( $\alpha = 0.05$ ) showed this value to be significantly lower than the hardness value of the monolithic HA. The lower hardness value is the result of indenting on top of the lower modulus PSu layers. This is the same phenomenon, which produced large holes when indenting laminates made through the matching halves technique, see Chapter 3. The difference here is that PSu provide greater support than air, but still allowed for increased deflection at the HA surface being indented, and thus larger impressions are made leading to lower hardness values.

A comparison of load displacement curves for the laminate and the monolithic HA, Figure 5.1, shows the dramatic increase in load bearing capacity of the laminate over the monolithic HA. Hardness values were the only mechanical property measured in this study that decreased for the laminates compared with the monolithic HA. The values for failure loads, failure stresses, work of fracture, and toughness all dramatically increased for the laminates, see Figure 5.2. The percentage increase of each of these properties for the 400-200-800 laminates over the monolithic HA are shown in Table 5.1.

Apparent fracture toughness,  $K_{app}$ , value of  $7.2 \text{ MPa}\cdot\text{m}^{1/2}$  was calculated from the average work of fracture value for the laminates shown in Table 5.1 and equation 2.15. This represented a 620% increase from the  $K_{app}$  value of  $1.0 \text{ MPa}\cdot\text{m}^{1/2}$  for the monolithic HA.  $K_{app}$  for the laminates is well within the  $2\text{-}12 \text{ MPa}\cdot\text{m}^{1/2}$  range, which is reported for bone.

The presence of the PSu resulted in an increase in strength and toughness of the HA. The toughening mechanisms responsible for these increases are characterized through fractography, and will be discussed in detail later in this chapter.

Table 5.1 Comparison of the average mechanical property values for the monolithic HA versus the 400-200-800 laminates.

	Failure Load	Failure Stress	Work of Fracture	Absorbed Energy at Failure
Monolithic HA - Indented	63 N	22 MPa	11 J/m <sup>2</sup>	5 kJ/m <sup>3</sup>
400-200-800 Laminates	150 N	56 MPa	620 J/m <sup>2</sup>	60 kJ/m <sup>3</sup>
Percent Increase	140%	154%	5500%	1100%

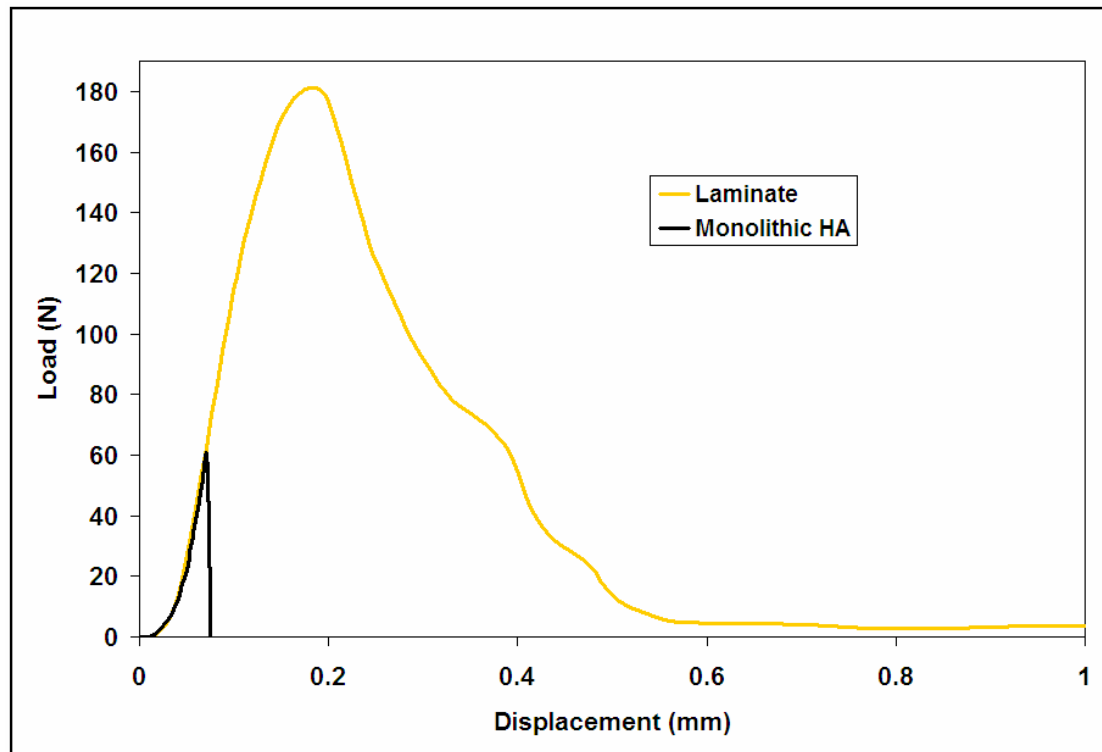


Figure 5.1 Comparison of load displacement curves for the 400-200-800 laminates compared with monolithic HA.

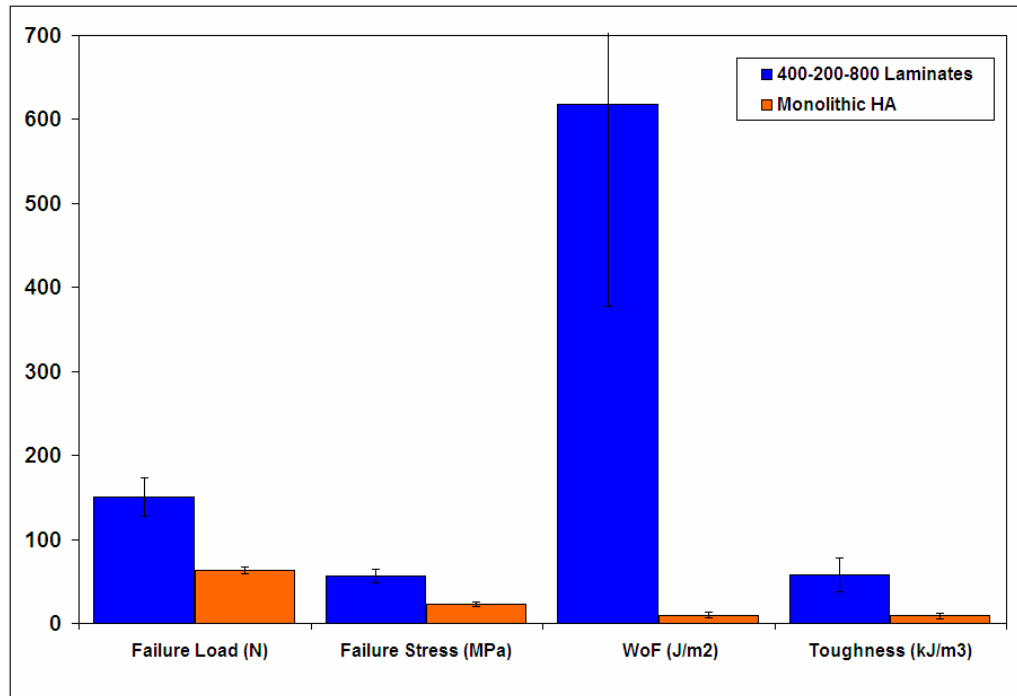


Figure 5.2 Comparison of mechanical properties measured for monolithic HA as the 400-200-800 laminates. The units of the ordinate axis vary for each property listed with units designated in the column headings.

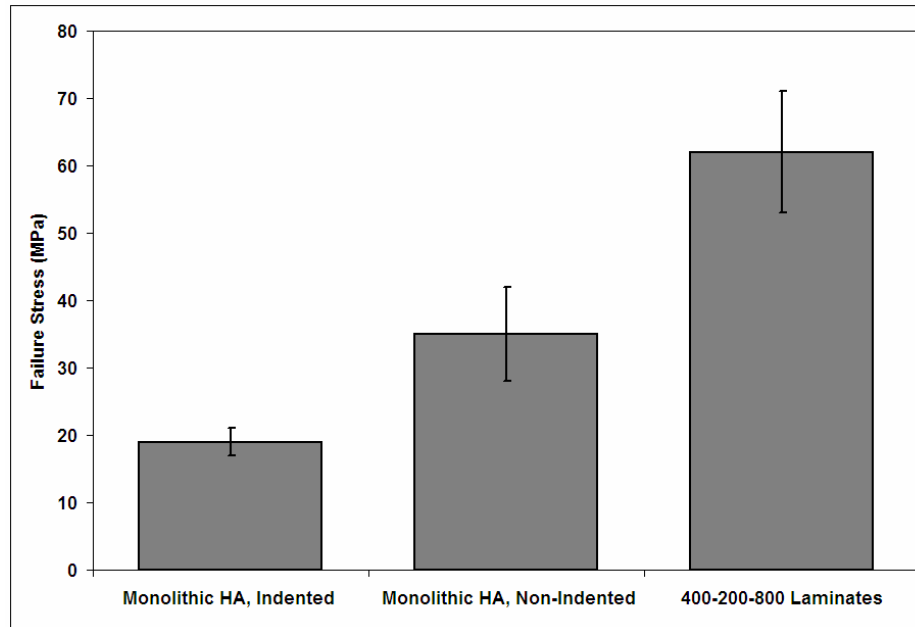


Figure 5.3 Comparison of failure stress for 400-200-800 laminates versus both indented and non-indented monolithic HA specimens.

## Testing of Laminate Parameters

### Initial Flaw Size Effect

Four groups of 400-200-800 laminates were tested with a range of initial flaw size produced using indentation. Larger indent loads produced larger impressions, which become fracture origins upon loading in biaxial flexure. Usually the length of radial cracks emanating from the corners of the indent would be measured to show that larger flaws were introduced into the material. However, due to the porous nature of the HA radial cracks were not visible through optical microscopy prior to loading in biaxial flexure. Diagonal lengths and hardness values calculated for the indented groups are shown in Table 5.2. Statistical analysis ( $\alpha=0.05$ ) showed that there was no significant difference in the hardness values between the three indent loads, but that the hardness values were all statistically different from the hardness value of the monolithic HA. While the 9.35 kg indents showed the same hardness values as the smaller indent loads, there was significant lateral cracking associated with this largest indent load, Figure 5.4.

Table 5.2 Hardness data for initial flaw size laminates.

Indent Load (kg)	Diagonal length ( $\mu\text{m}$ )	Hardness (GPa)
1.35	$130 \pm 10$	$1.4 \pm 0.2$
3.35	$213 \pm 14$	$1.3 \pm 0.2$
9.35	$377 \pm 29$	$1.2 \pm 0.2$

It was hypothesized that the magnitude of failure loads for these four groups of laminates would be controlled by the initial flaw size of the outer HA. Therefore, the non-indented group would fail at the greatest loads, while the laminates with the largest initial flaws, the 9.35 kg group, would fail at the lowest loads. Mechanical data for the four different flaw size groups is found in Table 5.3. Statistical analysis ( $p = 0.05$ )

showed that there was no difference between failure loads, failure stresses, work of fracture, or toughness for any of the four initial flaw sizes. These results show that laminate strength was not controlled by the initial flaw size of the outer HA surface as was hypothesized, and that the mechanical behavior of the laminates is dependent on other factors, that were explained through further laminate testing and analysis, which will be discussed later in this chapter. These results will show that for laminate with the 400-200-800 geometry the strength of the laminate is determined by the flaw size of the middle HA layer.

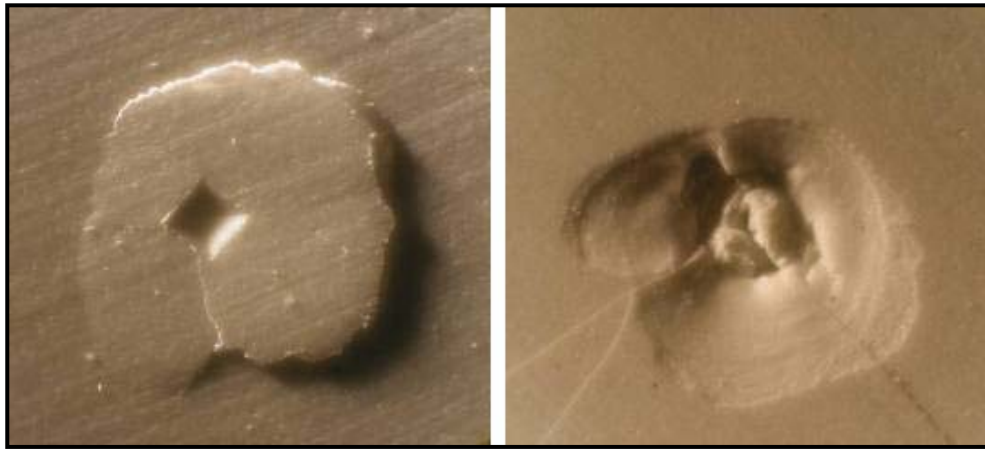


Figure 5.4 Lateral cracking seen during indentation using a 9.35 kg load (left), and the resulting chip-out that occurs during loading (right).

Table 5.3 Mechanical property data versus indent loads

Indent Load	Failure Loads (N)	Failure Stress (MPa)	Work of Fracture ( $\text{J/m}^2$ )	Absorbed Energy at Failure ( $\text{kJ/m}^3$ )	Kapp ( $\text{MPa}\cdot\text{m}^{1/2}$ )
NI	$134 \pm 33$	$50 \pm 13$	$586 \pm 99$	$52 \pm 21$	7.0
1.35	$165 \pm 22$	$62 \pm 8$	$672 \pm 377$	$68 \pm 26$	7.5
3.35	$150 \pm 23$	$57 \pm 9$	$618 \pm 240$	$60 \pm 21$	7.2
9.35	$152 \pm 17$	$58 \pm 6$	$609 \pm 142$	$56 \pm 19$	7.2

NI = Nonindented Laminates

### **Loading Rate Effect**

Four groups of 400-200-800 laminates were tested at four different loading rates to test what effect the viscoelastic polymer had on laminate behavior. Failure loads were statistically equivalent ( $\alpha=0.05$ ) for each of the four loading rates. The failure stress (Figure 5.5) and absorbed energy at failure (Figure 5.6) versus loading rate curves best demonstrate how the viscoelastic nature of PSu affects laminate behavior. Statistical analysis ( $\alpha=0.05$ ) shows that there is no statistical difference between the failure loads for the four loading rates. There is a statistical difference between the toughness values for the different loading rates. However, there is no statistical difference between the failure loads of the 2 fastest loading rates of 2.5 and 25 mm/min.

The results show that the viscoelastic nature of the PSu does not directly influence the failure strength of the laminates, but does affect the toughness. The toughness increase is a function of the viscoelastic nature of the PSu. PSu is a viscoelastic material, and as such, behavior is time dependent. The behavior of the PSu depends of the relaxation time of the polymer. The relaxation time is dependent upon the viscosity and elastic modulus of the PSu and reflects how the polymer deals with applied loads at a molecular level.

### **Polysulfone Layer Thickness Effect on Laminate Behavior**

Since the viscoelastic nature of PSu was shown to influence the toughness of laminates, it was hypothesized that the amount of viscoelastic material compared to HA would have a significant effect on laminate behavior. This was the rationale for testing laminates fabricated with different PSu layer thicknesses.

Laminate geometries and hardness values are shown in Table 5.4. As with the previous two testing parameters, the hardness values were not statistically different

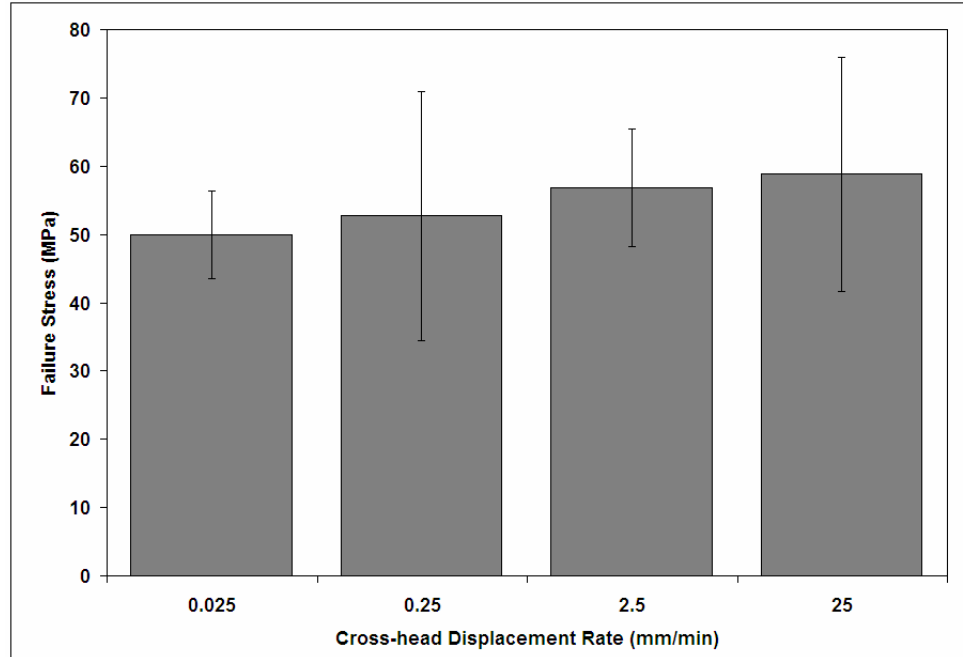


Figure 5.5 A plot of failure stress versus loading rate.

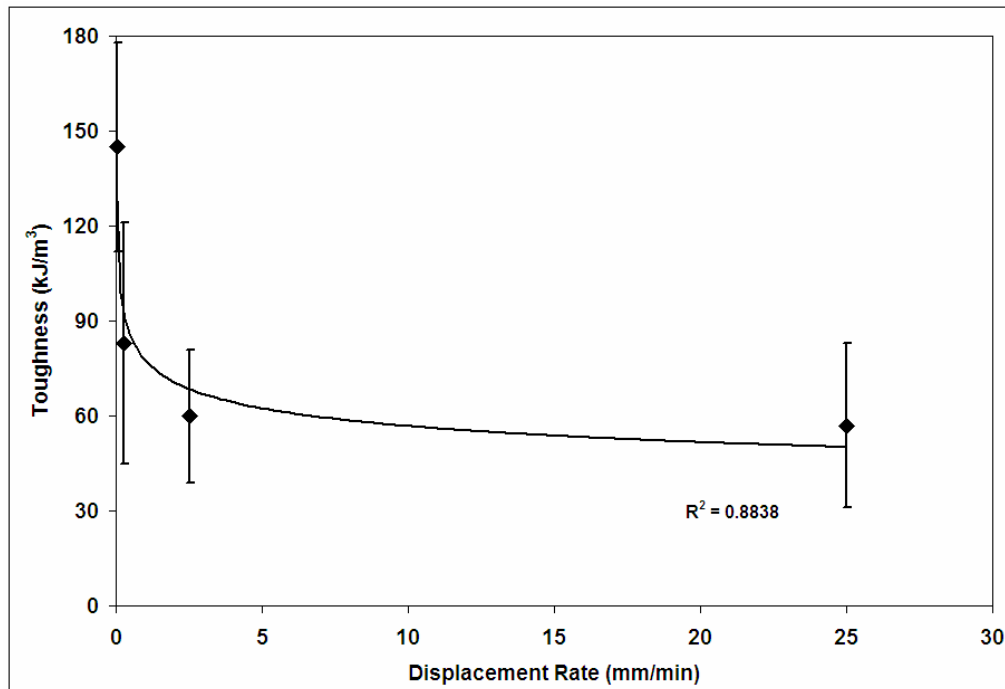


Figure 5.6 A plot of absorbed energy at failure (toughness) versus loading rate for 400-200-800 laminates.

( $\alpha=0.05$ ) for the four laminate geometries, but were statistically lower than the hardness of the monolithic HA due to increased deflection resulting from the presence of the lower modulus PSu.

The failure loads, Figure 5.7, increased with increasing polymer thickness, which would be expected since the thickness also increases as the PSu layer thickness was increased. However, the 50  $\mu\text{m}$  PSu laminates 1.7 mm thick failed at the same loads as the monolithic HA specimens, which were 2.0 mm thick. This demonstrates an increased load bearing capacity of a laminate over the monolithic material. Since stresses are proportional to  $P/t^2$ , where P is the load and t is the thickness the thinner laminates fail at a greater stress than the thicker monoliths, Figure 5.8. The 400-100-800 laminates with a thickness of 1.8 mm have even greater failure loads and stresses compared to the monoliths. These results were the first demonstration of the potential of the laminate system, as a thinner material could be used in place of the thicker monolith and have the same load-bearing capacity.

Table 5.4 Hardness data for the laminates with different PSu layer thicknesses.

Laminate Geometry	n	Total Thickness (mm)	Hardness (GPa)
400-50-800	4	1.7	$1.04 \pm 0.51$
400-100-800	6	1.8	$1.11 \pm 0.36$
400-200-800	7	2.0	$1.30 \pm 0.16$
400-400-800	6	2.4	$1.24 \pm 0.19$

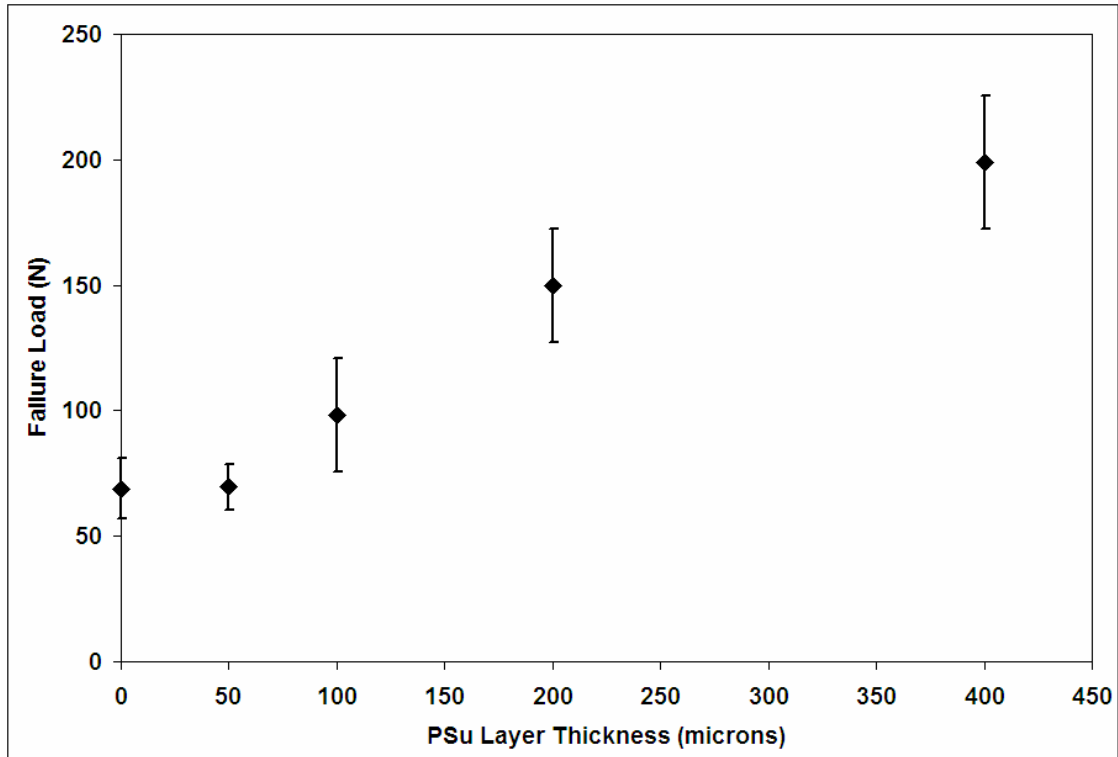


Figure 5.7 A plot of failure loads versus PSu layer thickness. Monolithic HA failure load is plotted as a PSu layer thickness of 0.

The stress values were also plotted versus the ratio of the outer HA layer thickness to the PSu layer thickness, Figure 5.9, for comparison to same plot generated using laminate theory, Figure 4.9. The laminate theory stress/N values were multiplied by an arbitrary 100N load to get the stress values shown on Figure 5.9. This adjustment was made in order to compare the trend curves on the same scale. The actual stress/N values are  $< 1$  MPa and the predicted curve could not be seen on the scale of the experimental values. Comparison of the predicted curve versus the statistical trend for experimental data shows that the laminate theory can be used to predict failure stresses for laminates with decent accuracy.

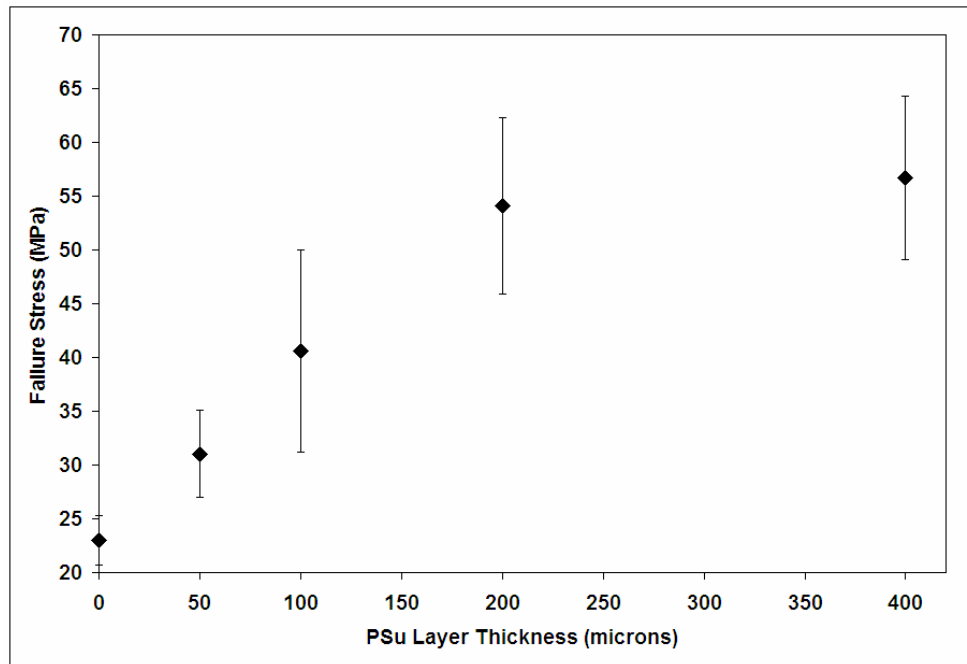


Figure 5.8 A plot of failure stress vs. PSu layer thickness. Monolithic HA is plotted as a PSu thickness of 0.

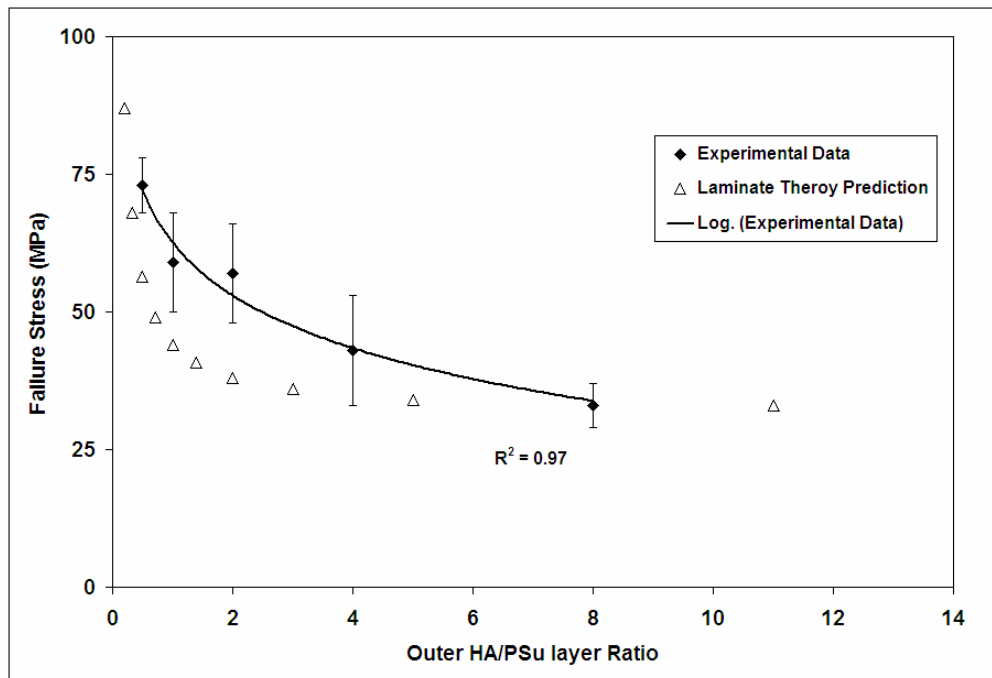


Figure 5.9 A plot of stress vs. outer HA/PSu layer thickness ratio for a comparison of experimental values to laminate theory predictions.

Additionally, the work of fracture (Figure 5.10) and absorbed energy at failure (Figure 5.11) increase as the PSu layer thickness increases.  $K_{app}$  also increased as the PSu layer thickness is increased, Table 5.5. However, the absorbed energy at failure values are statistically ( $p=0.05$ ) equivalent for the two thickest PSu layers. This is a result of a different failure mechanism for the 400-400-800 laminates, which will be described later in this chapter.

Table 5.5 Apparent toughness values versus increasing PSu layer thicknesses

Laminate Geometry	$K_{app}$ (MPa-m <sup>1/2</sup> )
Monolithic HA	1.0
400-50-800	3.7
400-100-800	5.4
400-200-800	7.2
400-400-800	7.2

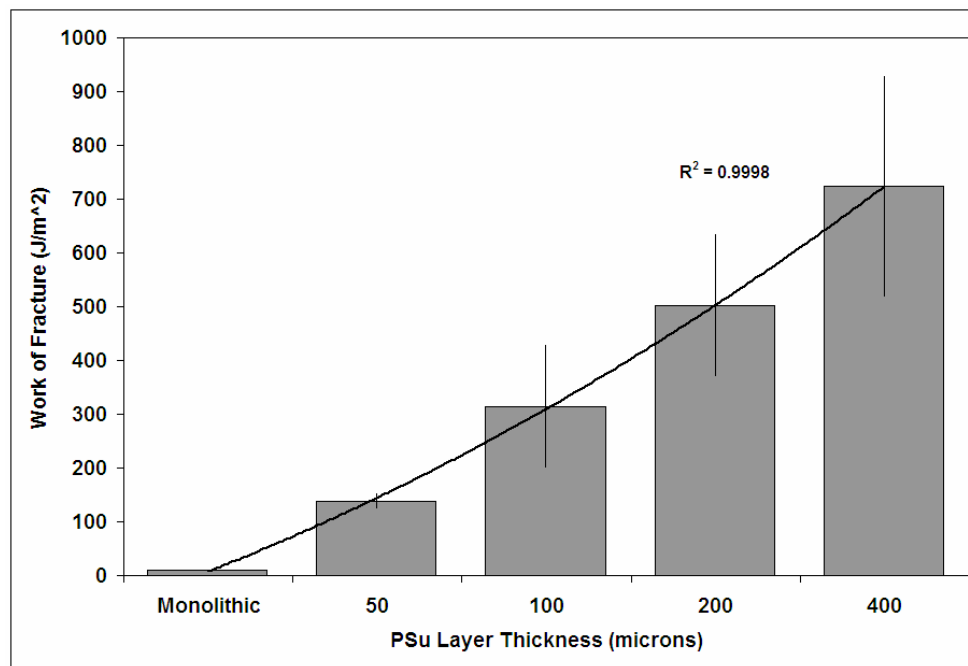


Figure 5.10 A plot of work of fracture vs. PSu layer thickness

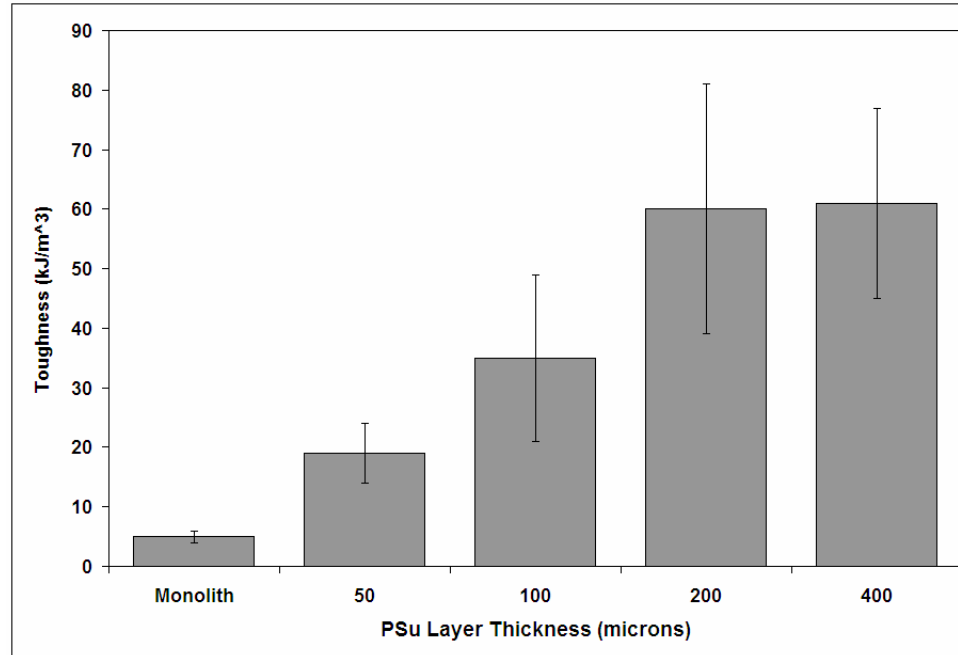


Figure 5.11 A plot of absorbed energy at fracture (toughness) vs. PSu layer thickness

### Outer HA Layer Thickness Effect on Laminate Behavior

Testing of laminates with the same outer layer thickness indented with different indent loads showed no difference in the failure loads, failure stress, work of fracture, or toughness. The mechanical properties measured were independent of the crack size placed in the outer layer; however, the outer layer was thicker than the initial flaw size produced by the selected indent loads. Therefore, laminates with outer HA layers  $< 400 \mu\text{m}$  were proposed to study the effect when the outer flaw size produced by indentation is larger than the thickness of the outer HA layer. Laminates were produced with outer layer thicknesses of 400, 200, and 100  $\mu\text{m}$ . 100  $\mu\text{m}$  represents the thinnest outer HA layer that could be produced through hand polishing.

The hardness values for the specimens built with thinner outer HA layers showed a significant effect of the PSu layers. Laminate geometries and hardness values are shown in Table 5.6. The hardness values are not statistically different ( $\alpha=0.05$ ) for the

100 and 200  $\mu\text{m}$  outer HA layers, but are statistically different from the 400  $\mu\text{m}$  thickness. The impression showed visible plastic deformation around the edges of the indents indicating that contact stresses were penetrating to depths greater than the thickness of the outer HA layer. A discussion of laminate failure mechanisms later in this chapter will show that indentation of outer HA layer  $< 400 \mu\text{m}$  causes the laminates to fail by a different mechanism than laminates with outer HA layers 400  $\mu\text{m}$  thick.

Table 5.6 Hardness data for laminates with different outer HA layer thicknesses.

Laminate Geometry	n	Total Thickness (mm)	Diagonal Length (mm)	Hardness (GPa)
100-200-800	6	1.4	$459 \pm 135$	$0.33 \pm 0.16$
200-200-800	6	1.6	$397 \pm 179$	$0.57 \pm 0.36$
400-200-800	7	2.0	$213 \pm 14$	$1.32 \pm 0.17$

Thinner outer HA layer had a significant effect on the mechanical behavior of the laminates. The failure loads for these laminates are shown in Figure 5.12. The failure loads for the 100-200-800 laminate geometry, which have a total thickness of 1.4 mm, is a 200% improvement over monolithic HA specimens of a comparable 1.5 mm thickness, and a 60% improvement over monolithic HA specimens having a greater thickness of 2.0mm.

Failure stresses for the outer HA layer specimens are shown in Figure 5.13. The stress value for the 100-200-800 laminates is the highest of all laminates tested in this study. The reason for this, as will be described in greater detail in this chapter, is that the indentation damage zone is larger than the outer HA layer thickness, and proceeds to make one large flaw that penetrates the two outer layers and into the middle HA layer of the laminate. The net effect, as will be shown, is a small flaw within the middle HA layer being bridge by PSu, which affectively increases the fracture toughness of the area

around the critical flaw, with the result being greater than failure loads and thus the greatest calculated stress values. The result is an almost 400% improvement over the failure stress of the monolithic HA

Along with the high strength values, the thinner outer HA laminates have the greatest toughness values compared to other laminate geometries. While the work of fracture values, Figure 5.14, are not statistically different for the three outer HA thicknesses tested, the absorbed energy at failure (toughness) values increase with decreasing outer HA layer thickness, Figure 5.15. This is the result of the increased toughness around the crack tip produced by the indentation damage zone, and the resulting PSu bridging of the initial flaw.

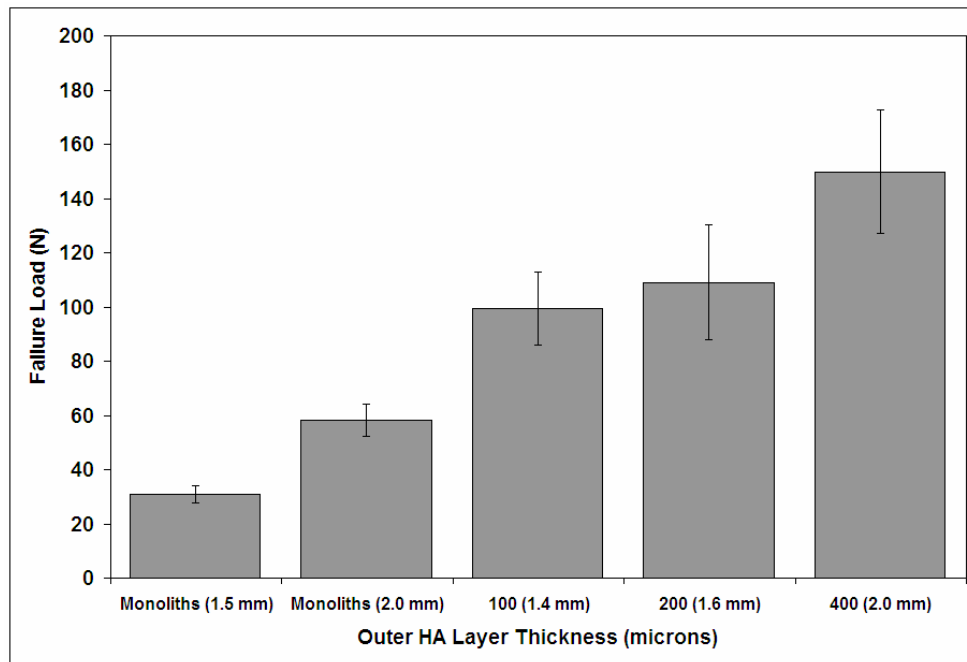


Figure 5.12 A plot of failure loads versus outer HA layer thickness. The total thickness of the specimens is shown in parenthesis.

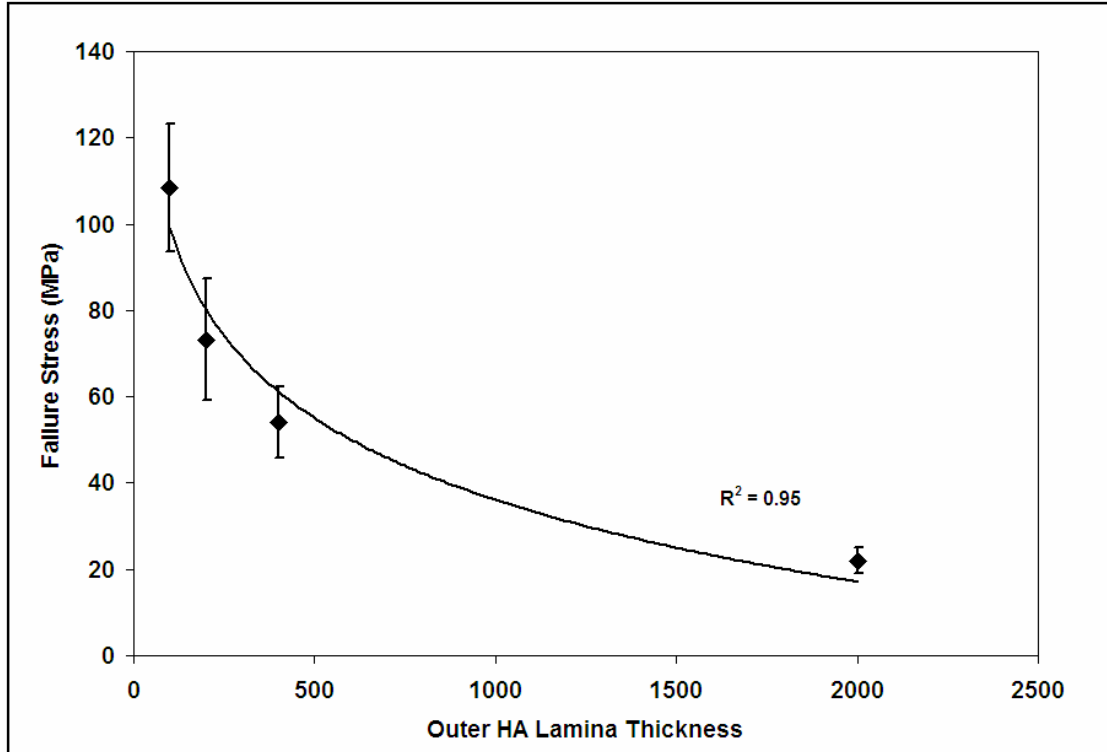


Figure 5.13 A plot of failure stresses versus outer HA layer thickness. Monolithic HA is plotted as a 2000  $\mu\text{m}$  thick HA layer.

Even though the thinner outer HA specimens had the greatest toughness calculated from the area under the stress-strain curve, apparent fracture toughness values do not follow the same trend, see Table 5.7. The reason for the difference in trends is that the apparent fracture toughness is calculated from the work of fracture, and takes into account the composite elastic modulus, see Equation 2.15. Since the laminates with different outer HA layers had comparable work of fracture values, it follows that the lowest modulus material would have the lowest apparent toughness value.

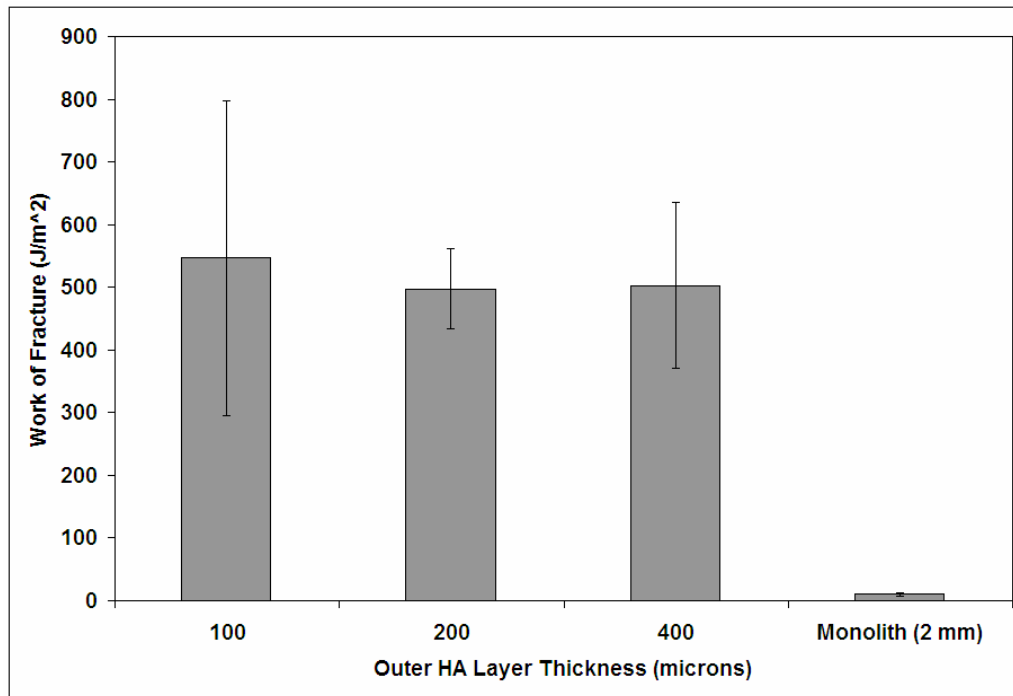


Figure 5.14 A plot of work of fracture versus outer HA layer thickness.

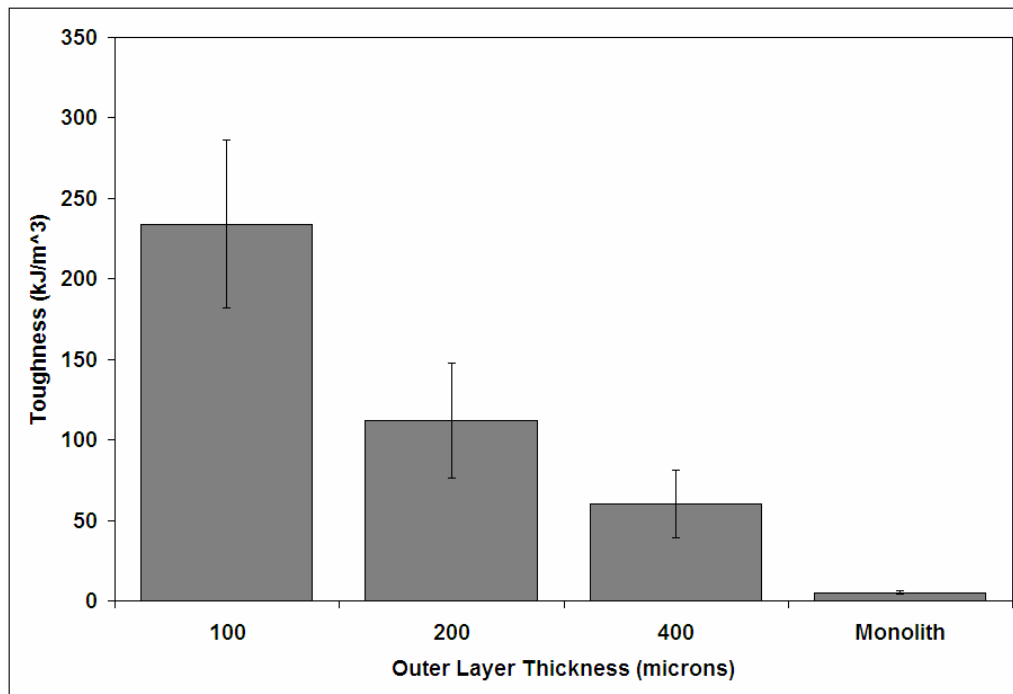


Figure 5.15 A plot of toughness versus outer HA thickness.

Table 5.7 Apparent fracture toughness comparison for different outer HA layers.

Laminate Geometry	$E_c$ (GPa)	$K_{app}$ (MPa-m <sup>1/2</sup> )
Monolithic HA	52	1.0
100-200-800	37	6.4
200-200-800	40	6.3
400-200-800	42	7.2

### Thick Middle Layer Effect on Laminate Behavior

The results from the study of the thin outer HA layers showed that the greatest stress was obtained with thin layers. Thus, laminates with thin outer layers and thick middle layers should result in increased strength and increased load-bearing capacity. The principle is that if laminates with 100  $\mu\text{m}$  outer HA layers failed at the same high stress levels, thicker middle layers would increase the load because stress is proportional to  $P/t^2$ .

Four laminate geometries with thicker middle layers were built. These geometries, along with hardness values calculated for each group are shown in Table 5.8.

Table 5.8 Hardness data for the four laminate groups prepared with thicker middle HA layers.

Laminate Geometry	n	Diagonal Length (mm)	Hardness (GPa)
200-200-1200	6	250 $\pm$ 29	0.98 $\pm$ 0.21
100-200-1400	6	292 $\pm$ 127	0.89 $\pm$ 0.60
200-100-1400	6	388 $\pm$ 72	0.43 $\pm$ 0.17
100-100-1600	6	267 $\pm$ 125	0.97 $\pm$ 0.47

The mechanical property data for the thicker middle layer specimens show that no advantage was gained by increasing the thickness of the middle HA layer. The failure loads for the thicker middle HA layer laminate, Figure 5.16, were surprisingly lower than

expected. The laminate theory model predicted that the 100-100-1600 group should fail have one of the highest failure loads. However, the experimental failure loads are equivalent to the failure loads of the non-indented monoliths, and to the 200-200-800 laminates from the prior section, which are thinner and therefore should have smaller loads. The poor failure loads of the 100-100-1600 specimens are the first direct indication that the ultimate failure loads are not controlled by the outer HA layer.

Failure stresses for the thicker middle layer laminates were dependent upon the thickness of the PSu layers. In the cases of the 100-100-1600, and the 200-100-1400 laminate groups there was no significant difference between the failure stresses of the laminates versus the failure stress of non-indented monolithic HA. However, there is a significant increase in the failure stress of the 100-200-1400 laminates over the 200-100-1400 laminates. This fact demonstrates the effect that laminate geometry has on the mechanical behavior of the laminate system, and shows that the designed placement of the PSu layer is a critical component that influence the behavior of the laminates.

While the 100-100-1600 has the lowest stress/load value calculated using laminate theory at the outer tensile surface it has the smallest difference between this stress values at the outer HA layer and the stress values calculated at the tensile surface of the middle HA layer. For the calculated values, see Table 4.5. The difference is only 0.08 MPa between the two values. What this signifies is that only a small energy increase in the form of increased loading is necessary to reinitiate crack propagation through the middle layer. The 400-200-800 laminate from previous sections had higher failure loads of 150 N with the same total thickness. The difference between the outer and middle stress values for the 400-200-800 specimens is 0.22 MPa. This signifies that

it will require a greater increase in load to reinitiate crack propagation through the middle HA layer for the 400-200-800 laminates then for the 100-100-1600 laminates.

### **Idealized Laminate**

Having already shown the greatest stress values for the laminates can be obtained by reducing the thickness of outer HA layer, the goal became to design the laminate geometry that would produce the greatest failure load. The total thickness for the laminate would be held constant at 2.0 mm. However, an improved load bearing capacity through a change in laminate geometry was desired. The principle developed from the middle layer testing showed that the greater the difference between the predicted tensile stress of outer and middle HA layers the greater the load has to be to reinitiate crack propagation through the middle HA layer. A number of theoretical laminate geometries were modeled using the laminate theory, Figure 4.9. With these criteria in mind, the 350-400-500 geometry was selected. The difference in outer and middle layer stresses for this geometry was 0.32 MPa.

Figure 5.18 is a plot of the failure loads gained for the 350-400-500 laminates versus other laminates having a total thickness of 2.0 mm. While there was not a dramatic increase in failure loads as expected, the 350-400-500 group statistically ( $p=0.05$ ) yields the greatest failure loads of any of the laminates fabricated to a thickness of 2.0 mm. The 171 N average is a 175% increase in the load-bearing capacity for these laminates over indented monoliths, and a 110% increase over the non-indented monoliths. This is another demonstration of the predictive abilities of the laminate theory as the 350-400-500 laminate geometry was selected solely on laminate theory calculations.

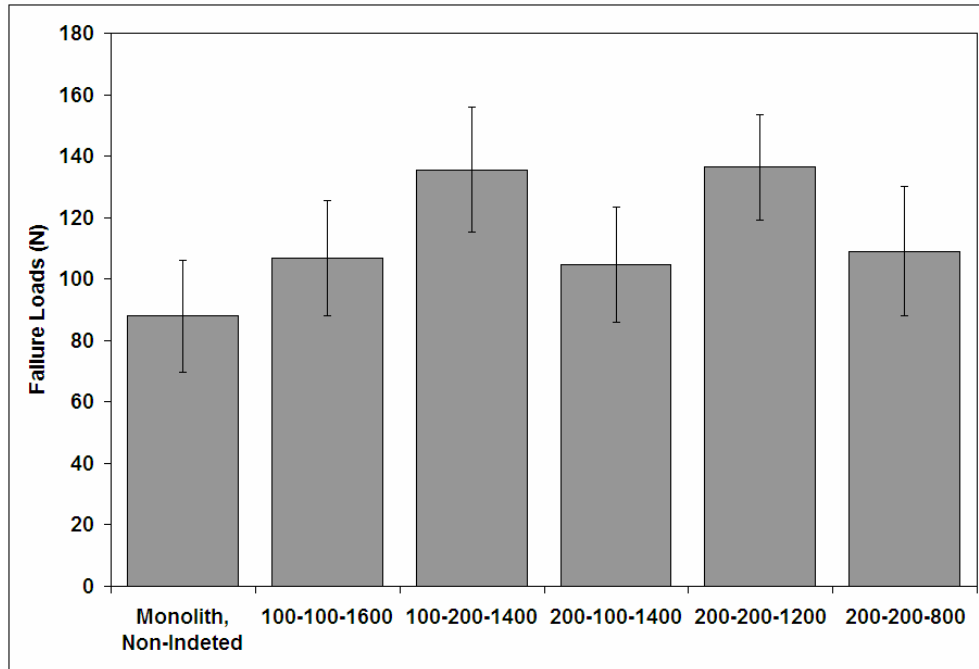


Figure 5.16 Failure loads for laminates with thicker middle HA layers.

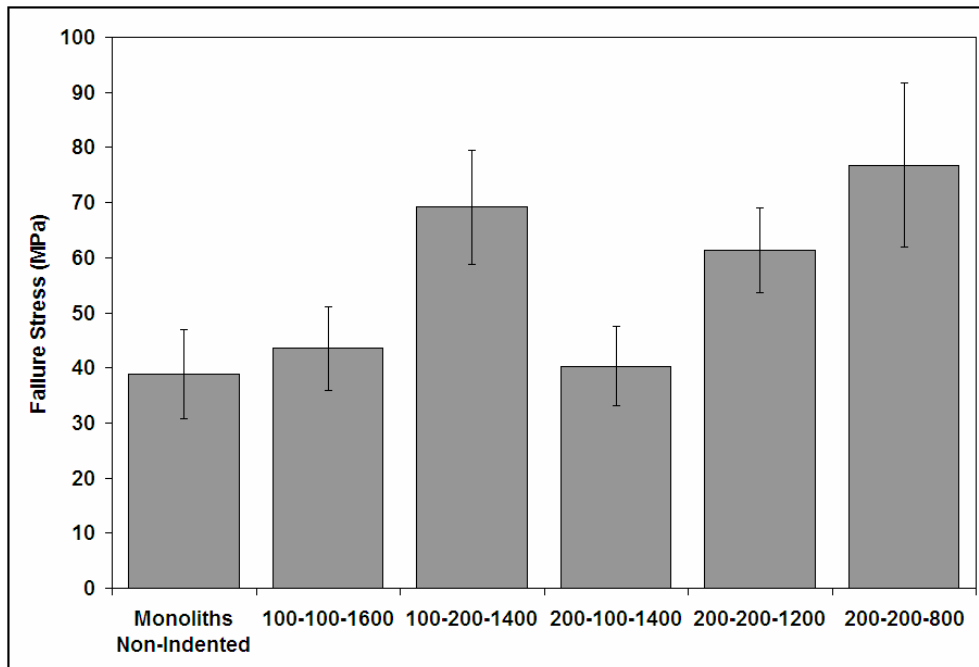


Figure 5.17 Failure stresses for laminates with thicker middle layers

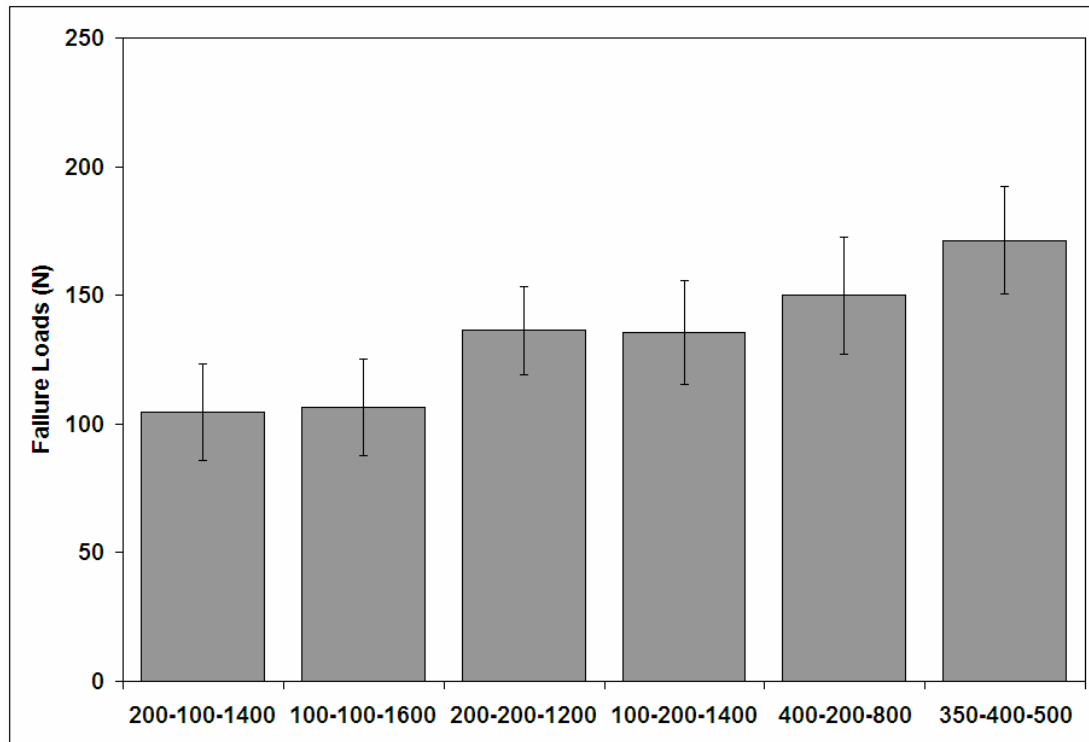


Figure 5.18 Experimental failure loads for all the laminate geometries having a total laminate thickness of 2.0 mm

### Determination of Failure Mechanisms

Through mechanical testing the laminates were shown to have superior mechanical properties. It now becomes important to explain why the properties are achieved and through what mechanisms. The goal is to use the laminate theory to improve design and predict actual failure loads. This requires a better understanding of the failure mechanisms.

### Laminate Failure Modes

Loading in biaxial flexure produced three laminate failure modes. The most common failure mode was complete separation of all five layers due to the bending. The

result was that laminates fractured into two or three pieces similar to monolithic failures shown in Figure 2.25. Figure 5.19 shows the fracture surface of a 400-200-800 laminate.

The second failure mode is the same as the first except specimens remain in one piece following failure in biaxial flexure. Optical microscopy showed that fracture through both outer and the middle HA layers occurred, but at least one of the PSu layers is still intact for these specimens, Figure 5.20. Loading was automatically stopped by the

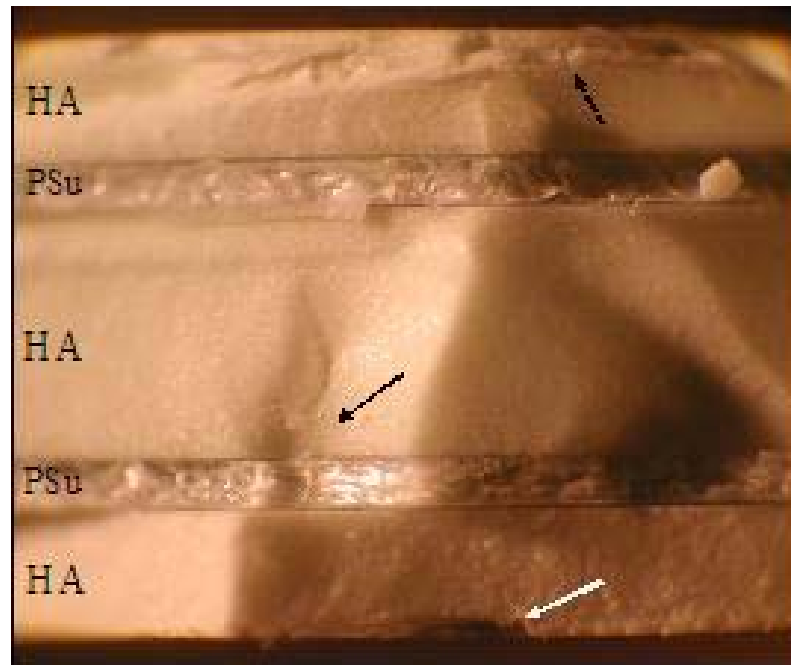


Figure 5.19 An optical micrograph of 400-200-800 laminate fracture surface. The locations of the initial indent flaw (white arrow), middle layer flaw (black arrow), and loading piston contact are all indicated.

testing machine once the applied loads fell below 10 N or if the testing machine reached the maximum displacement allowed by the loading fixture. If loading could be continued, then eventually the PSu layers would have undergone continued deformation until final failure. Intact samples are a result of experimental limitations that arise from

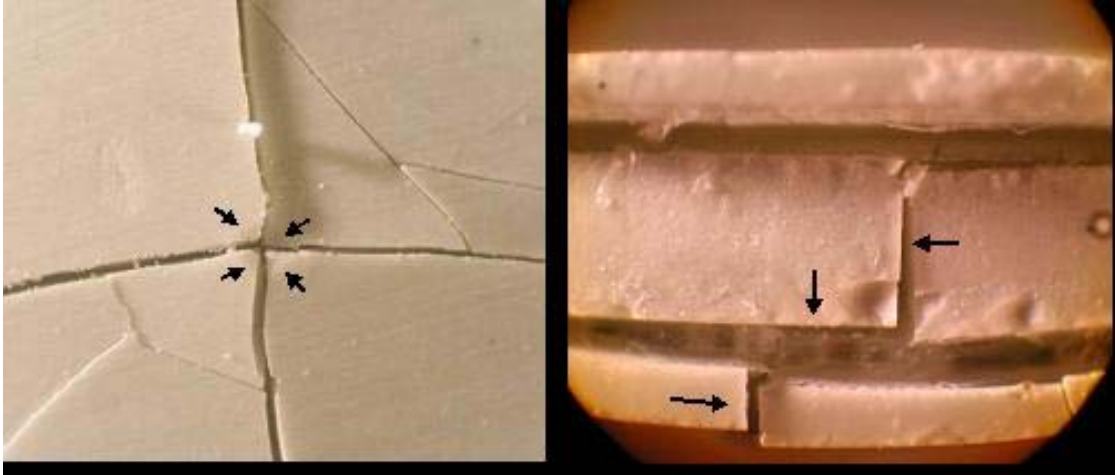


Figure 5.20 Optical micrographs of a laminate still intact after being loaded to failure in biaxial flexure. Left: Failure occurred from the initial indent (indicated by the arrows) in the outer HA surface, Right: Examination of the edge of the specimen shows failure of the outer HA layer, delamination along the interface, and failure of the middle HA layer.

loading ductile materials in a bending test, as there is a finite displacement range that can be tested. Most polymers are loaded in pure tension to allow for large displacements for this reason.

The third failure mode was penetration of the loading piston through the entire thickness of the specimens. This failure mode occurred primarily in the laminates with the thickest PSu layers. Analysis of the fracture surfaces showed that the punch through was a secondary failure as the laminates failed first through bending in the HA layer before the PSu layers failed; at this point failure loads became sufficient to drive the loading piston through the middle of the laminates. The fractured laminates have a large hole through the center, but are otherwise intact. Figure 5.21 is a picture of a 400-400-800 laminate that failed via the punch through mode. The indented outer HA layer has been shattered and is completely removed from the image, revealing the partially failed PSu layer. The loading piston actually penetrated through all five layers of the laminate.



Figure 5.21 SEM image of punch through failure of a 400-400-800 laminate. The remnants of the indented outer HA layer are indicated by the black arrows, failure of the PSu layer where the loading piston breached all five layers is indicated by the white arrow.

### Fractography of Laminates

Optical microscopy and SEM were used to analyze the fracture surfaces of the laminates. Fractography was used to find fracture origins of the indent side HA layers and of the middle HA layer. These fracture origins were used to calculate the failure stress of each layer through Equation 2.12. The fracture toughness of each HA layer was assumed a constant value of  $0.6 \text{ MPa}\cdot\text{m}^{1/2}$ . This was the fracture toughness calculated from testing of the monolithic HA specimens (see Table 2.4).

Fracture analyses are divided into two categories: analysis of the 400-200-800 laminates and analysis of all other laminate geometries. The reason for this division is

that the 400-200-800 laminates have the only geometry with an outer HA layer thickness greater than the flaw size produced by the 3.35 kg load. The average flaw size for monolithic HA specimens indented with the 3.35 kg load was 313  $\mu\text{m}$ . Analysis of fracture surfaces revealed that laminates with an outer HA layer thickness  $< 313 \mu\text{m}$  showed flaws from indentation that bridged the PSu layer, and therefore will be analyzed differently than the 400-200-800  $\mu\text{m}$  laminates.

### **Fracture Analysis of 400-200-800 Laminates**

#### **Failure of the Outer HA Layer**

Fractography performed on all laminates showed that laminates with indented outer HA layer thicknesses of 400  $\mu\text{m}$  contained slightly larger initial flaw sizes than those of monolithic HA with the same indent loads. Typical flaws within the outer HA layer produced through indentation are shown in Figures 5.22-5.23. These larger initial flaws are consistent with the results of hardness measurements, which showed that a 3.35 kg load produced larger indents in the laminates than in the monoliths, Table 5.9, most likely due to the presence of the less stiff polymer layers.

Table 5.9 Comparison of flaw sizes for monolithic HA and the outer HA layer for 400-200-800 laminates.

	Non-Indented Flaw Size ( $\mu\text{m}$ )	Flaw Size From 3.35 kg Indent ( $\mu\text{m}$ )
Monolithic HA	$98 \pm 43$	$313 \pm 39$
Outer HA Layer of Laminates	$125 \pm 37$	$374 \pm 75$

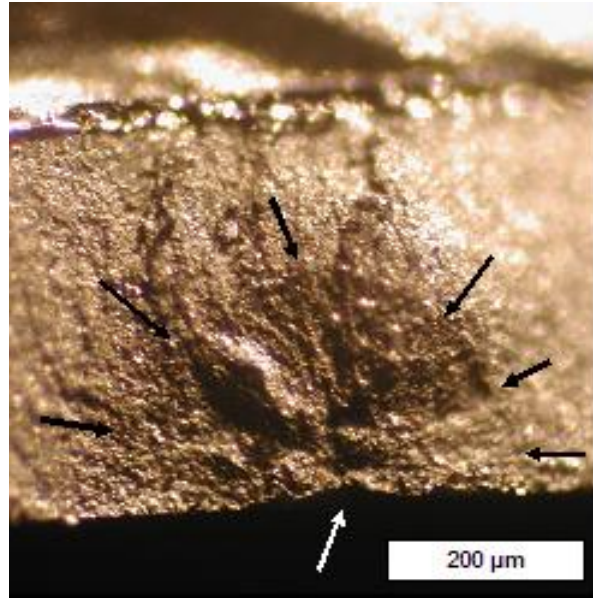


Figure 5.22 Optical micrograph of the initial flaw size (black arrows) produced by a 3.35 kg indent (white arrow) in a 400-50-800 laminate.

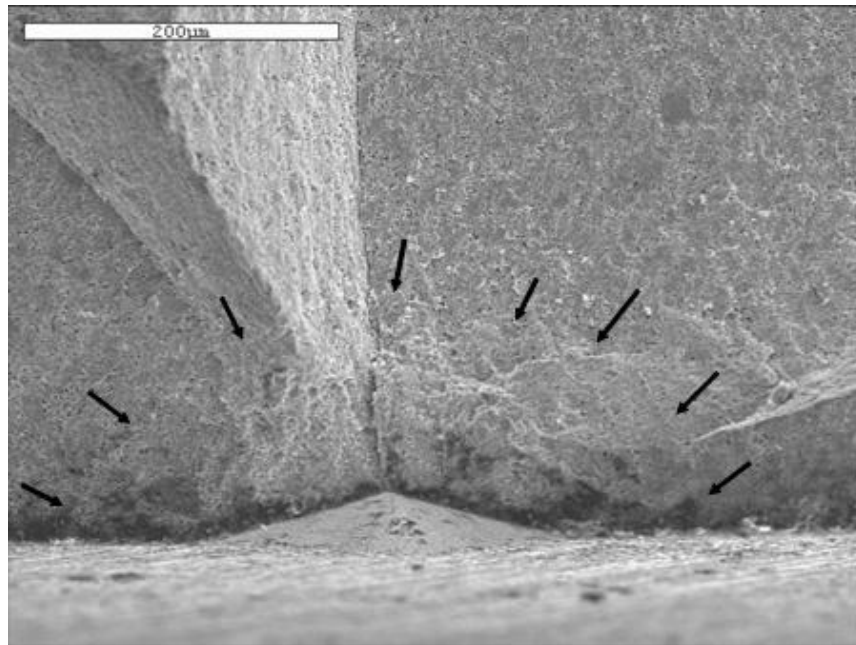


Figure 5.23 SEM image of the initial flaw produced in a 400-100-800 laminate produced by a 3.35 kg indent load.

Outer layer flaw sizes for the non-indented laminates were not statistically different ( $\alpha=0.05$ ) from the flaw sizes of the non-indented monoliths. With equivalent flaw sizes at the outer tensile surfaces, the failure stress and failure loads should be the same for the monolithic HA specimens and the outer HA layer of the laminates if the outer layer controls failure. Since the ultimate failure loads of the laminates have been shown to result from failure of the middle HA layer, the load at which the outer HA layer fractures had to be estimated from the load displacement curves, Figure 5.24. In some cases there was a measurable drop in loading that occurred when the outer HA layer failed making measurement of the failure load relatively straightforward. However, in most cases the failure load had to be estimated from the slope change of the load displacement curve.

To show that the outer HA layer failed first prior to the middle layer, failure loads and stresses were compared for nonindented laminates, and for the 400-200-800 laminates indented with 1.35 and 3.35 kg loads, Figure 5.25. From Equation 2.13, when fracture toughness is constant, an increased flaw size results in a decreased failure stress. The ultimate failure of the 400-200-800 laminates has been shown to be independent of the initial flaw size, Table 5.3, and therefore the laminates all failed at the same stress.

However, the fact that the failure stress of the outer HA layer is dependent upon initial flaw size indicates that the fracture process begins with the failure of the outer HA layer. The outer HA layer failure stresses were also compared for laminates with different PSu layer thicknesses. As seen in Figure 5.26, outer HA failure stresses are statistically ( $\alpha=0.05$ ) independent of the thickness of the PSu for the laminates with 400  $\mu\text{m}$  outer

layers. This result demonstrates that the initial failure of the laminates is dependent on the flaw size of the outer HA layer, and is not influenced by the PSu layer.

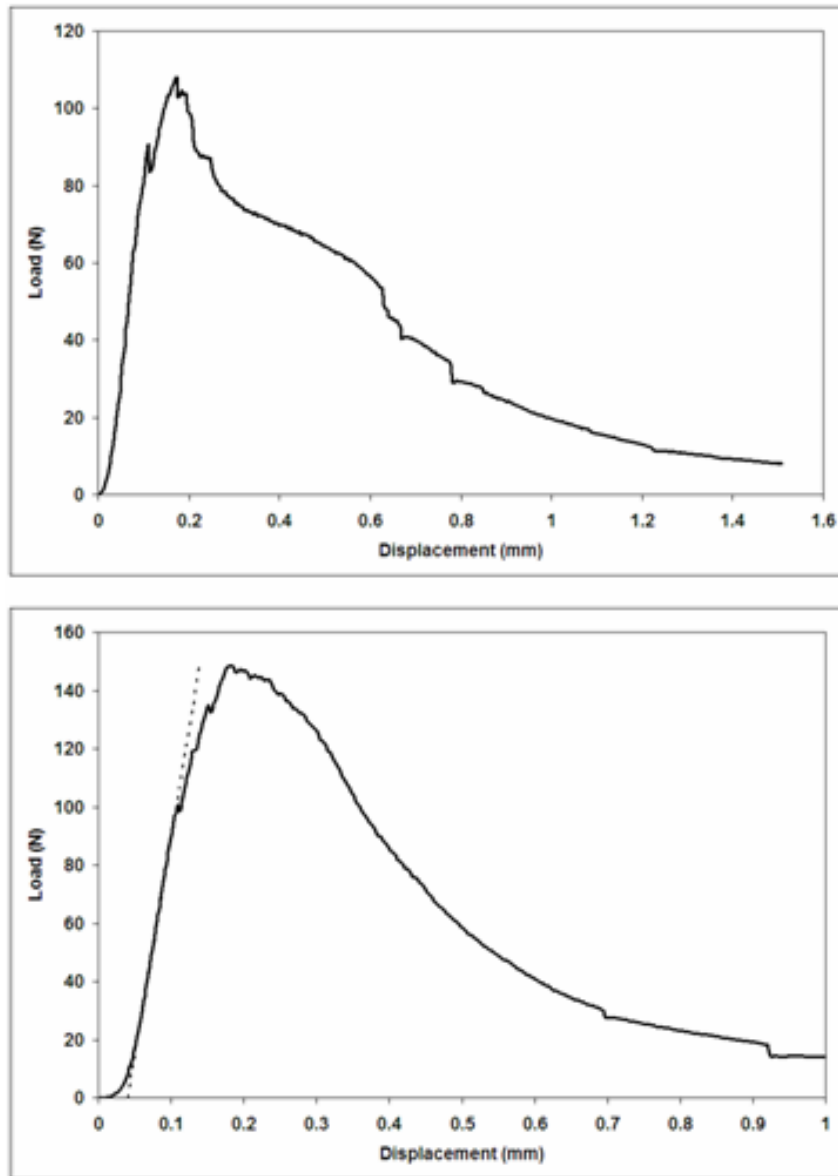


Figure 5.24 Load-displacement curves for two non-indented laminates. Outer HA layer failure loads are calculated either from the initial drop (top) or by extrapolating the initial slope (dashed line) and estimating when the slope change begins (bottom).

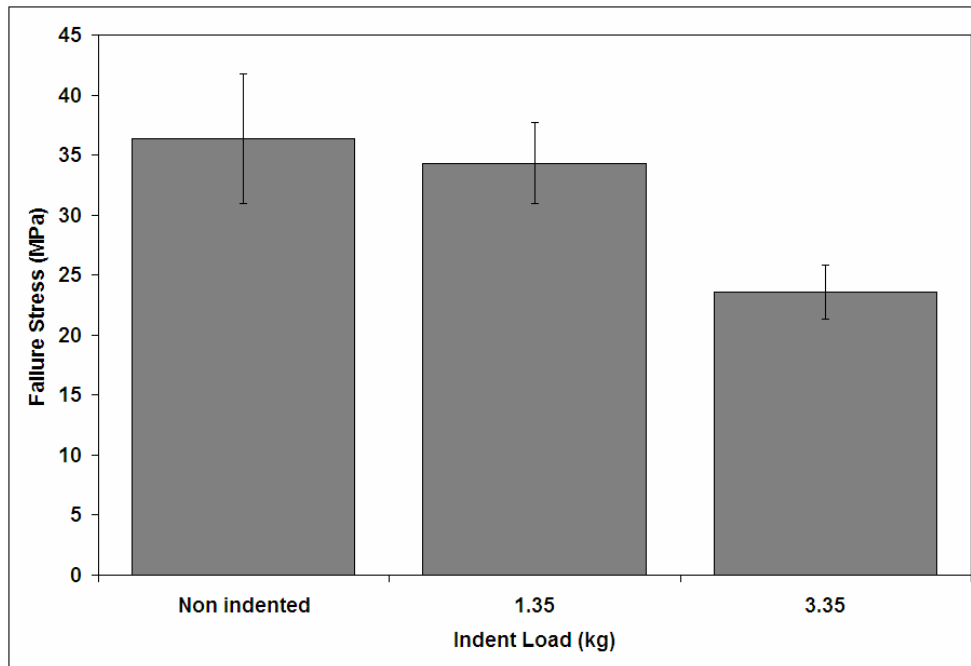


Figure 5.25 Failure stresses of the outer HA layer calculated for three different initial flaw sizes.

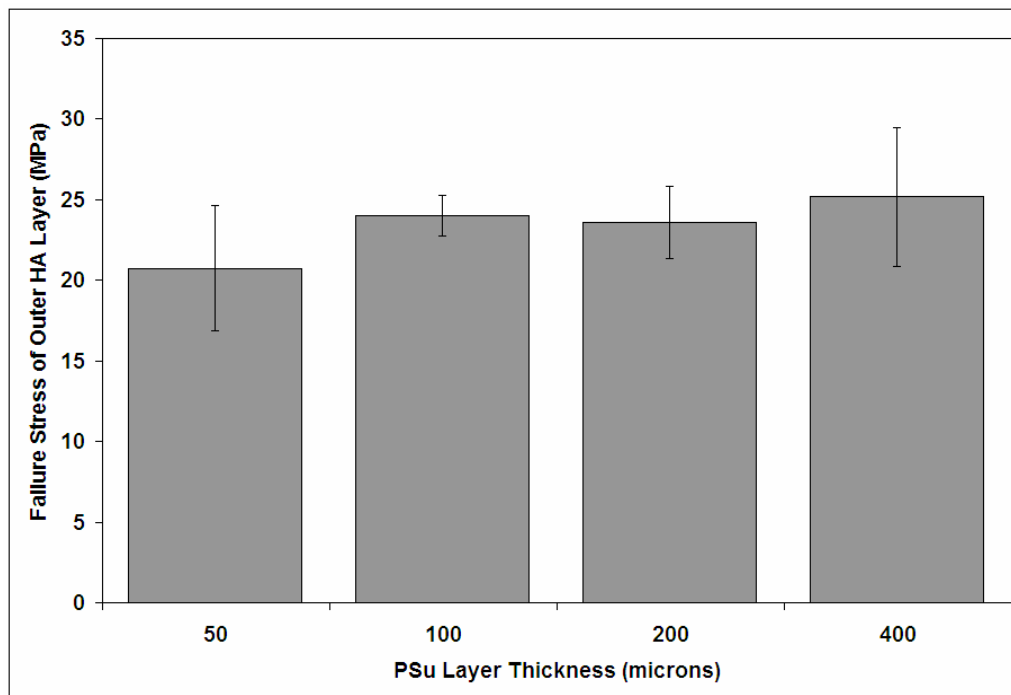


Figure 5.26 Failure stresses of the outer HA a layer for laminates built with different PSu layer thicknesses.

### Failure of the Middle HA Layer

Fracture origins were found and measured for the middle HA layers in order to calculate the stress at which the middle HA layers failed. Figures 5.27 – 5.29 are examples of the fracture origins that were found within the middle HA layers. Failure stresses for the middle HA layers were calculated using Equation 2.12, and assuming the fracture toughness of the middle HA layer to be the same as for the monolithic HA. The failure stress of the middle layer was also calculated by multiplying the experimental failure loads by the stress/1 N load calculated by laminate theory for the tensile surface of the middle HA layer. For the 400-200-800 laminates, the middle HA layer has a stress/1N load of 0.16 MPa. The comparison of these stresses shown in Table 5.10, demonstrates that there is good agreement between the two methods of calculation.

The two stress values are consistent with each other, and indicate that the laminate theory can be used to calculate the failure stress of the middle layer for a laminate structure. The stress/1 N load could also be used to estimate failure loads if the failure stress of the materials is relatively constant. Dividing an average failure stress by the stress/1N calculation produced the predicted failure load for the specimen.

Table 5.10 Middle HA layer failure stress calculations for the 400-200-800 laminates.

Laminate Geometry	n	Experimental Failure Load (N)	Middle Layer Flaw Size ( $\mu\text{m}$ )	FS, Flaw Size Calculation (MPa)	FS, LT Calculation (MPa)
400-200-800	13	155 $\pm$ 22	254 $\pm$ 41	30 $\pm$ 2	28 $\pm$ 6

n = number of tested specimens LT = laminate theory FS = Failure Stress

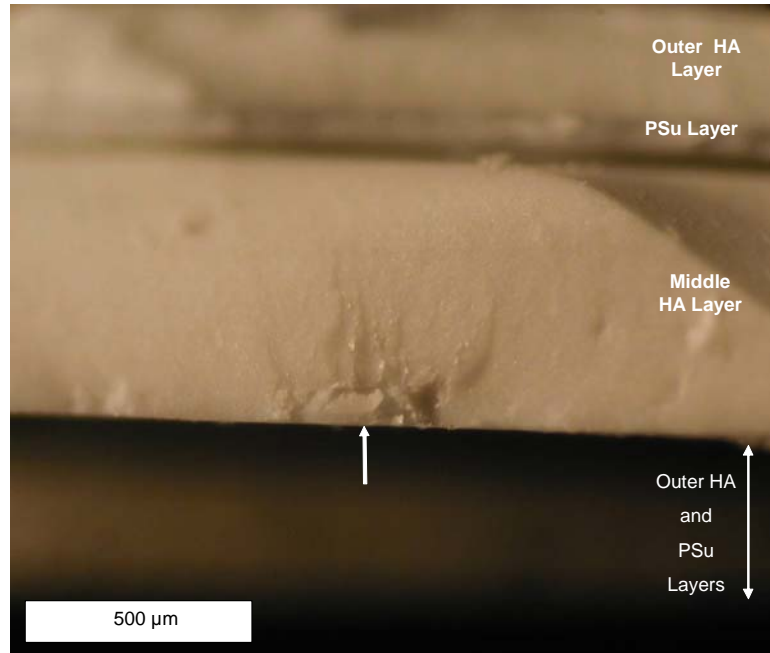


Figure 5.27 Optical micrograph of the fracture origin of a 400-200-800 laminate. The center of the flaw is indicated by the white arrow.

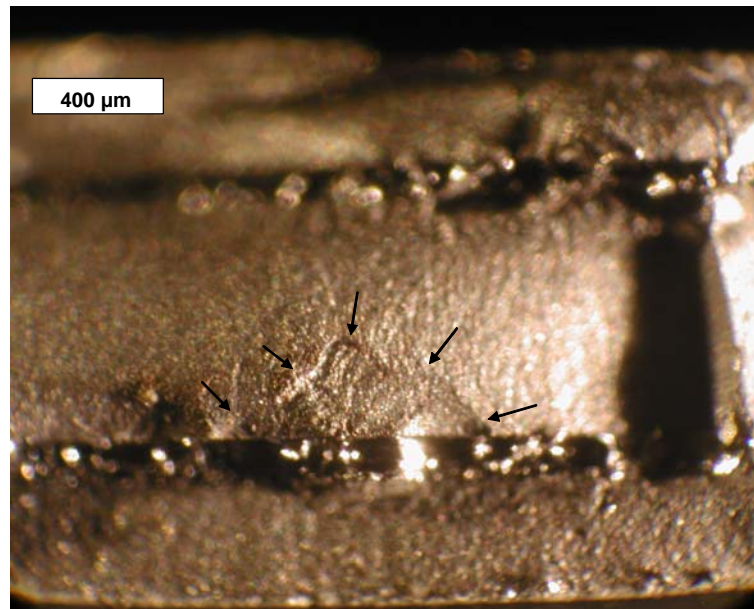


Figure 5.28 Optical micrograph of a middle layer fracture origin in a 400-100-800 laminate. The specimen has been sputter coated to make the surface marking stand out.

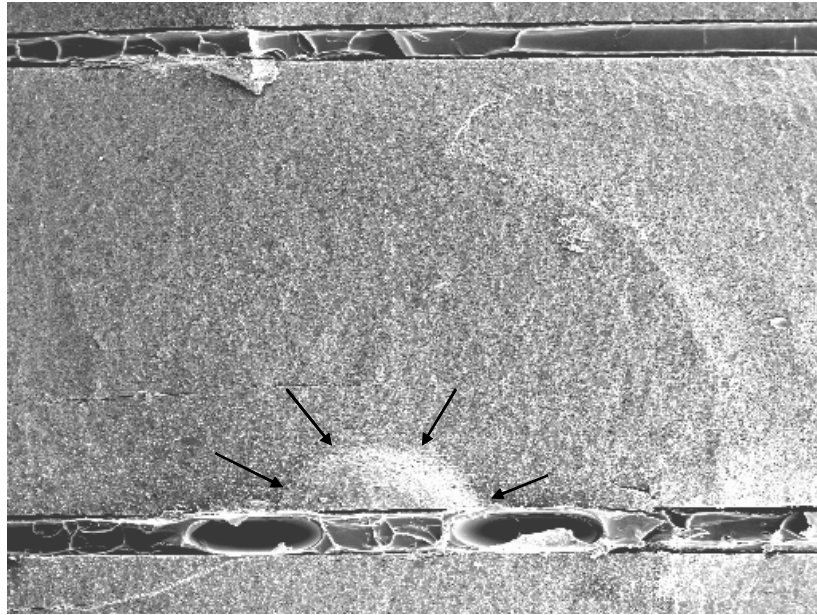


Figure 5.29 SEM image of the middle HA layer fracture origin.

#### **Failure of the Outer HA Layer, Loading Piston Side**

Fracture surface analysis also revealed contact damage resulting from the loading piston. The fracture markings are consistent with contact damage from blunt indenters that produce Hertzian cone cracks [38]. Cone cracks form due to localized tensile stresses located at the edge of the indenter and propagate at an angle of  $22^\circ$  from the surface. Damage from the loading piston was seen in the form of surface damage prior to tensile failure of the laminate in biaxial flexure, Figure 5.30, or as secondary fractures as the piston penetrates the laminate layers once tensile failure has occurred, Figure 5.31, although not all specimens showed damage from the loading piston. Determination of when piston damage had occurred was done by matching fracture markings on either side of cracks, which were produced by the loading piston. If fracture markings on either side of the crack are consistent with each other, as in Figure 5.31, then the loading piston crack occurred after primary failure. However, if fracture markings on either side of the

piston cracks differ in their patterns, as in Figure 5.30, then the piston damage occurred prior to bending failure.

### **Polysulfone Layer Failure**

Examination of the polymer portion of the fracture surface of the 400-200-800 laminates showed that the PSu layers failed in an unusual manner. Figures 5.32 and 5.33 are images of the PSu layer fracture at two different crosshead displacement rates. At first inspection, the images appear to show spherulitic structures that signify a crystalline polymer. However, PSu is known to be an amorphous polymer with little long range order.

Comparison of the PSu layers fractured at different crosshead displacements showed the greater the displacement rate the smaller the features within the PSu layers, indicating that the features seen are a result of failure mechanisms not crystallization during the drying process. Oblique lighting of the PSu layers causes the features to become invisible to the optical microscope when compared to the overhead lighting, Figure 5.34. PSu layers appear to show crazing because of the change in lighting angle; however, the features are much larger than would be expected for typical crazing, and crazing is usually associated with a coalescence of the crazes into one united crack front from which catastrophic failure occurs. The surface features seen in the PSu layer of the laminates occur throughout the entire length of the fracture surfaces, and never coalesce into one crack front.

Closer examination of the features using SEM shows that the features are failing in both brittle, Figure 5.35, and ductile manners Figure 5.36. In some cases, two PS features located side-by-side to one another, Figure 5.37, fail in two different manners.

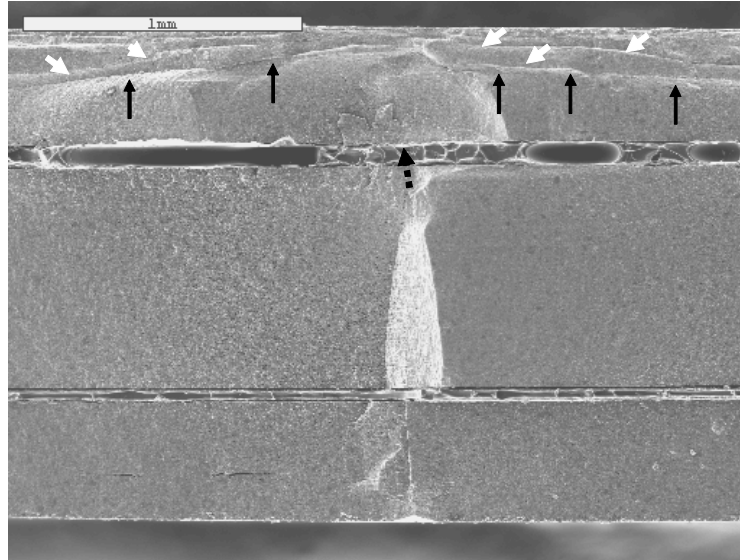


Figure 5.30 SEM image of a 400-100-800 laminate showing contact damage (white arrows) from the loading piston which occurred **prior** to propagation of the primary fracture (black arrows) which was reinitiated near the HA/PSu interface (dashed arrow).

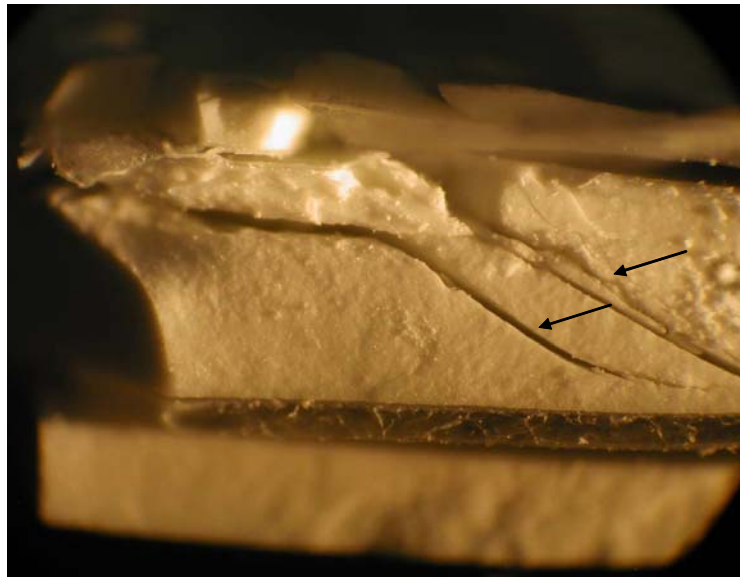


Figure 5.31 Optical micrograph of secondary cracks (arrows) which occurred through punch failure after primary failure from bending.

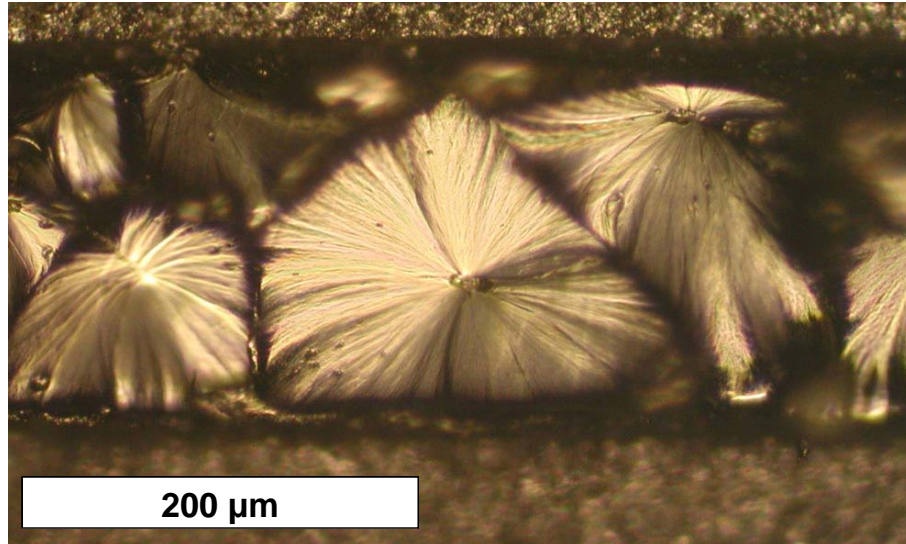


Figure 5.32 Optical micrograph of a PSu layer of a 400-200-800 laminate fractured at a crosshead displacement rate of 0.25 mm/min. The specimen was sputter coated prior to analysis.

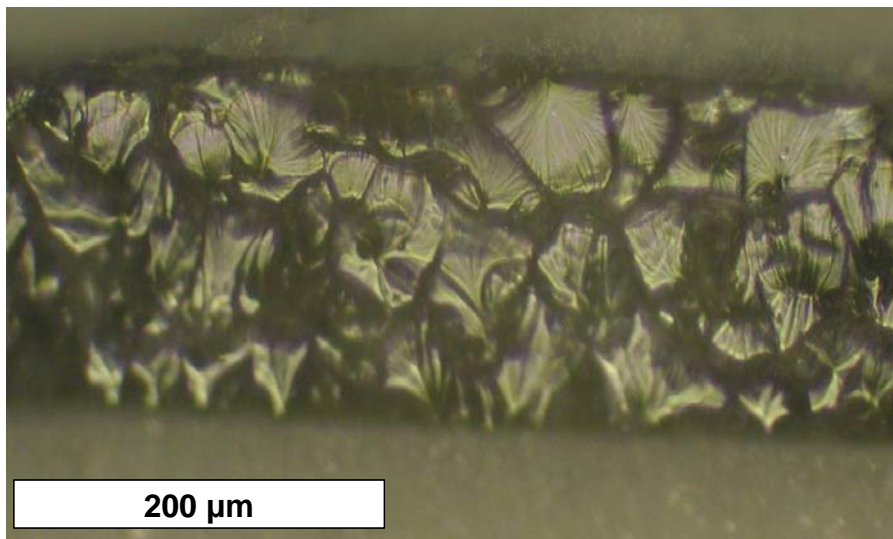


Figure 5.33 Optical micrograph of a PSu layer of a 400-200-800 laminate fractured at a crosshead displacement rate of 25 mm/min.

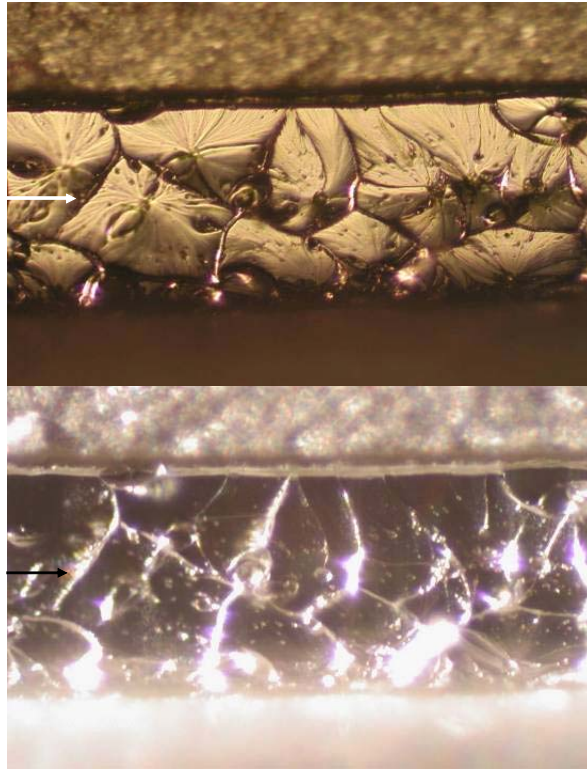


Figure 5.34 Optical micrographs of the PSu layer features through overhead (top) and oblique lighting (bottom).

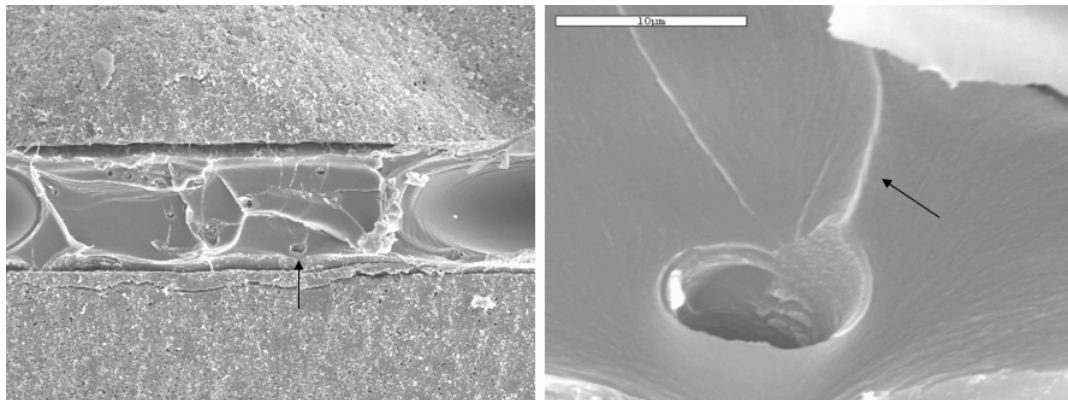


Figure 5.35 SEM images of brittle failure of the PSu layer, the pore (indicated by the arrow in the left image) shows a twist hackle marking (arrow in the right image) characteristic of brittle fracture.

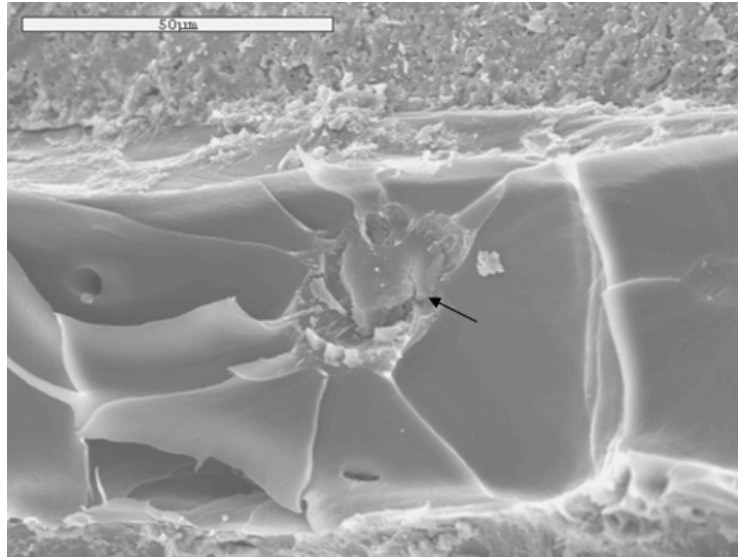


Figure 5.36 SEM image of ductile deformation of the PSu layer prior to failure at the center of the feature (black arrow).

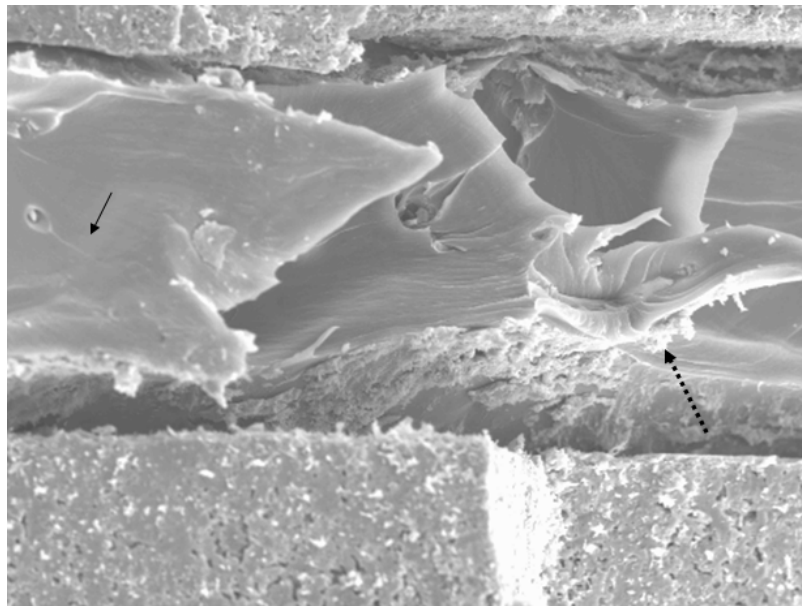


Figure 5.37 SEM image of two side-by-side features within the PSu layer that failed in different manners, a twist hackle marking (solid arrow) indicates the left feature failed in a brittle manner, while the pullout deformation (dashed arrow) of the right feature indicates ductile failure.

Analysis of the PSu fracture surface feature leads to no definitive explanation as to the origin of the features. Microscopic analysis demonstrated that these features are most likely not spherulites, or crazes. However, the size dependence of the features on stressing rate leads to the possibility that the features are the result of phase segregation that occurs during drying of the PSu films

As the TCE solvent begins to evaporate during drying of the PSu layer, the volume of the polymer/solvent mixture decreases. The evaporation process is constant on the macroscopic level, and controlled by a number of factors, which include the conditions the ambient environment, and viscosity of the polymer/solvent system. The rate of evaporation can be significantly affected by altering any of these conditions. The sensitivity of the evaporation process results in a range of evaporation rates at the microscopic level. Therefore, different regions of the drying polymer layer will have different concentrations of solvents, and therefore, different regions will dry at different rates.

While there is a range of solvent concentrations throughout the regions of the drying PSu layer, there is also a range in the size of PSu chains within each of these regions. Since the solubility parameter of the PSu does not change, a reduction in solvent due to evaporation causes the PSu chains to precipitate out of solution. The solubility parameter is dependent upon molecular weight [54], and thus the largest PSu chains precipitate out of solution first, followed by the smaller chains. However, due to chain interactions, and diffusion, when the larger chains precipitate out of solution, some of the smaller chains become entangled with the larger chains and are forced to precipitate out of solution. The net result of this drying process are phase separated

regions, the size of which is dependent on solvent concentration and the molecular weight distributions within specific each region of the drying PSu layer.

When the laminates are loaded in biaxial flexure, the failure of the PSu layers becomes dependent upon at what loading rate that the specimens are tested. At a slower loading rate, the PSu chains have greater time for relaxation processes to occur. This allows for activation of the largest polymer chains within the failure process, and the larger chains will then control failure of the PSu regions. These larger failure regions are seen along the fracture surface shown in Figure 5.32, which is for the slower crosshead displacement rate of 0.25 mm/min.

At increased loading rates, there is insufficient time for chain relaxation prior to ultimate failure. The faster loading rate means activation of only the smaller polymer chains within each phase segregated region since there is only sufficient time for the relaxation and orientation of the shortest PSu chains prior to chain scission occurring. The result is that failure is controlled by the small PSu chains within the phase segregated regions. The fracture surface of laminates tested at a crosshead displacement rate of 25 mm/min, Figure 5.33, shows an increased number of regions that are significantly smaller than the regions seen at the slower loading rate.

### **Interfacial Failure and Toughening Mechanisms**

As was described in Chapter 3 on laminate fabrication, prior to drying, the casting solution infiltrates into the porosity of the HA discs, forming the mechanical bonding that holds the layers together. This penetration can be seen macroscopically as a darkening color change in HA prior to drying. After drying the PSu layer becomes translucent and could not be seen due to light reflection off the white HA layers. However, the

sulfonated-PSu, which was used briefly in this study as described in Chapter 3, has an orange hue to the films when dry and can be seen though optical microscopy, Figure 5.38. Optical microscopy showed that sPSu penetrated to depths between 50 and 100  $\mu\text{m}$ .

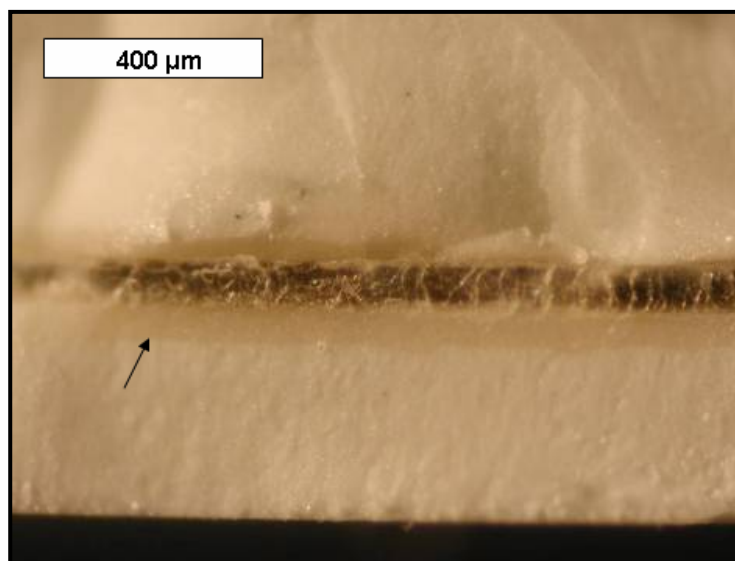


Figure 5.38 Optical micrograph of a sPSu/HA laminate showing the depth of penetration of the casting solution during solvent casting.

SEM revealed the depth of penetration was much deeper than measured through optical microscopy. Figures 5.39-5.42 are SEM micrographs of PSu found at different penetration depths into the HA. Figure 5.39 shows PSu penetration across more than half the thickness of the middle HA layer. Since casting is performed on both surfaces of the middle HA layer, there is a strong probability that PSu penetrates the entire thickness of the middle HA layers. Figure 5.40 show that the PSu bridges cracks that propagate through the HA. Figures 5.41-5.42 shows interfacial bridging that occurs in between the HA and PSu layers.

The ability of the PSu to bridge cracks is only one of the mechanisms that results in the increased toughness of the laminates compared with the monolithic HA.

Delamination causes crack arrest and leads to the required energy increase necessary to reinitiate cracks through the middle HA layer. Evidence of delamination can be seen through pullout of the PSu layers, Figure 5.43, and through PSu failure origins that occur as the crack travels along the HA/PSu interface. Delamination can also be seen in the form of crack deflection, Figure 5.20, as cracks propagate down the interface and then reinitiate into the middle HA layer. Failures of the PSu layers as cracks propagate along the interface are shown in Figures 5.44-5.45.

The combination of these toughening mechanisms leads to the increased failure strength and toughness of the 400-200-800 laminates compared to the monolithic HA.

#### **Failure Mechanism of Laminates with Outer HA Layers < 400 $\mu\text{m}$**

Laminates fabricated with outer HA layers thinner than 400  $\mu\text{m}$  failed via a different mechanism than the 400-200-800 laminates due to the size of the cracks which are produced through indentation of HA with a 3.35 kg load. The average flaw size produced from a 3.35 kg Vickers indent was 313  $\mu\text{m}$  as measured for fracture toughness calculation of the monolithic HA specimens. For the thinner outer HA layer contact stresses from the 3.35 kg indent were sufficient to cause crushing of the outer HA layer, deformation of the PSu layer beneath, and introduce cracks into the middle HA layer, see Figure 5.46. The resulting damage zone acts as the initial flaw from which crack propagation occurs during loading in biaxial flexure.

Flaw size measurements were made on only a small percentage of the tested specimens as the damage from indentation and subsequent loading left little of the outer HA layers intact for flaw size measurements. Average flaw sizes and the failure stresses

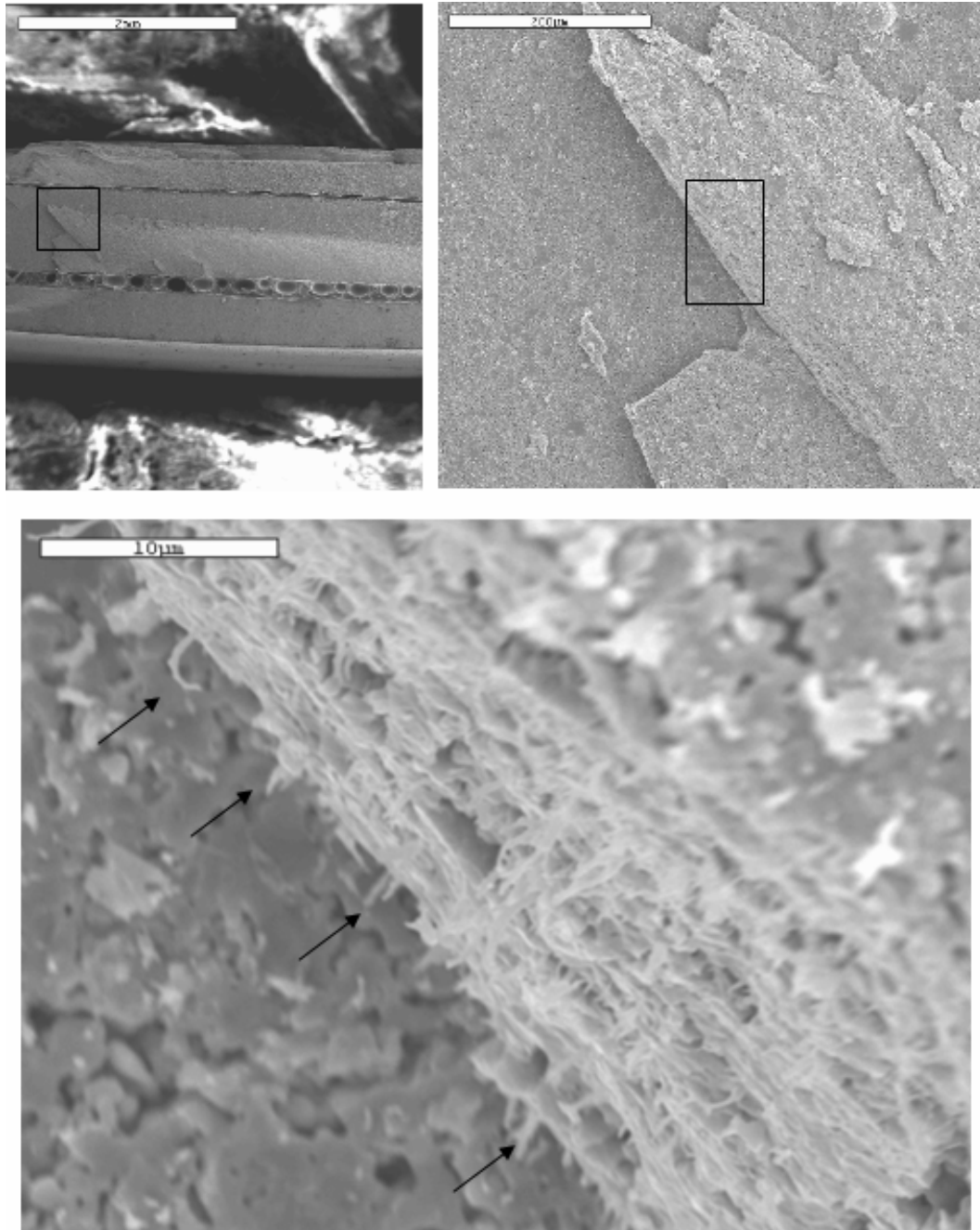


Figure 5.39 SEM images showing the penetration depth of PSu into the middle HA layer. The fracture surface is shown top left, the box indicates the area where the top right picture was taken, the bottom picture showing PSu pullout was taken from the area indicated by the box in the top right image.

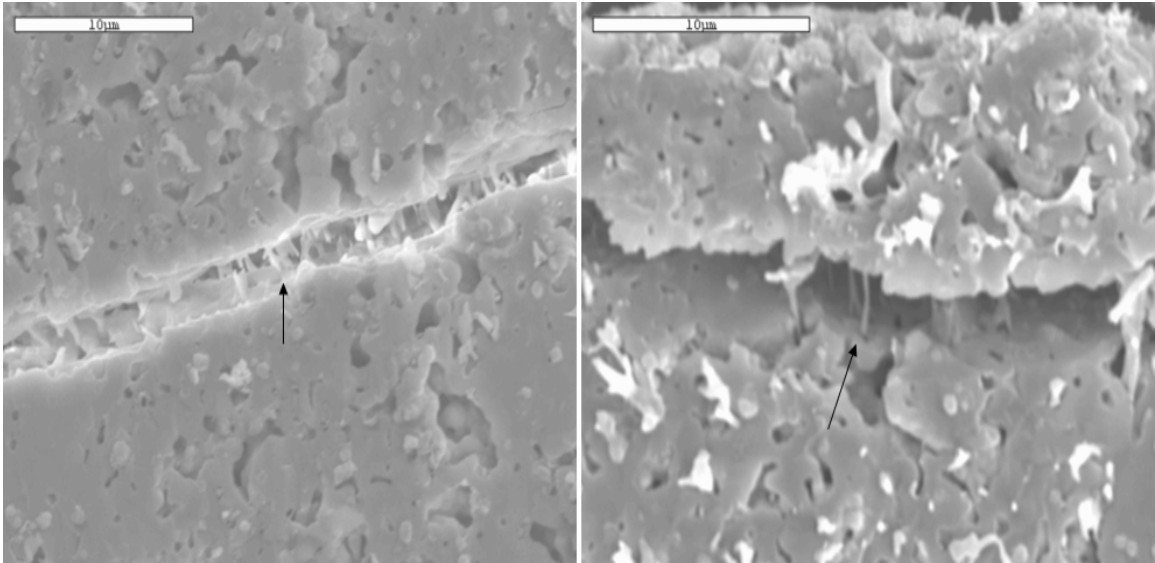


Figure 5.40 SEM images of PSu bridging of small cracks in the HA layers. These images were taken of the secondary interface crack shown in Figure 5.31.

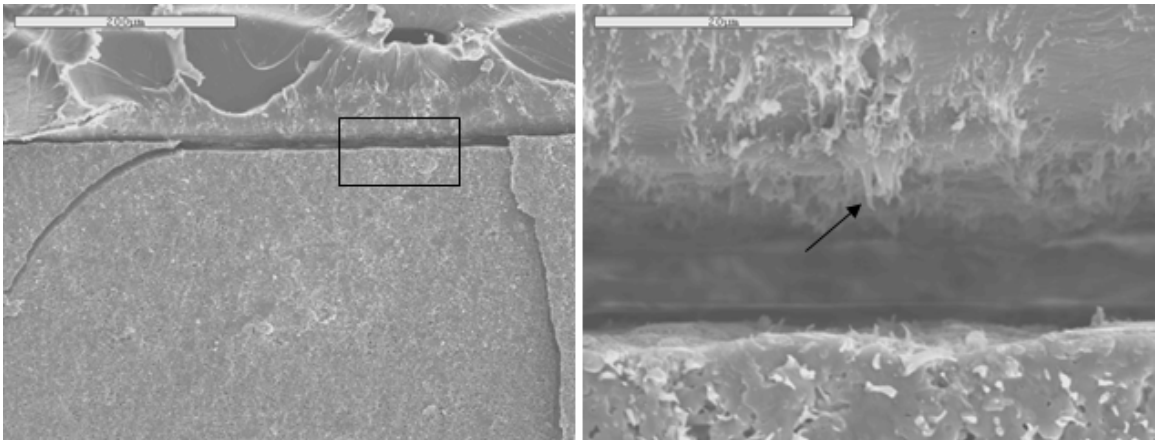


Figure 5.41 SEM images showing PSu bridging of the HA/PSu interface. PSu fibrils are indicated by the arrow.

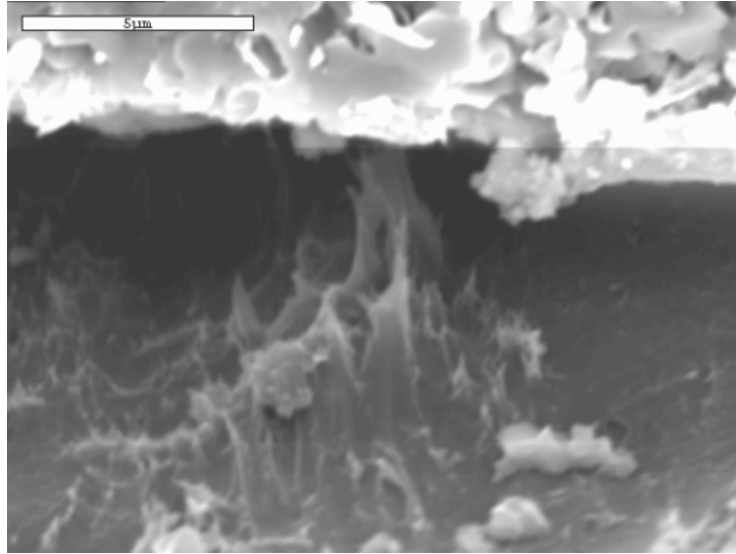


Figure 5.42 SEM image of PSu bridging of the HA/PSu interface

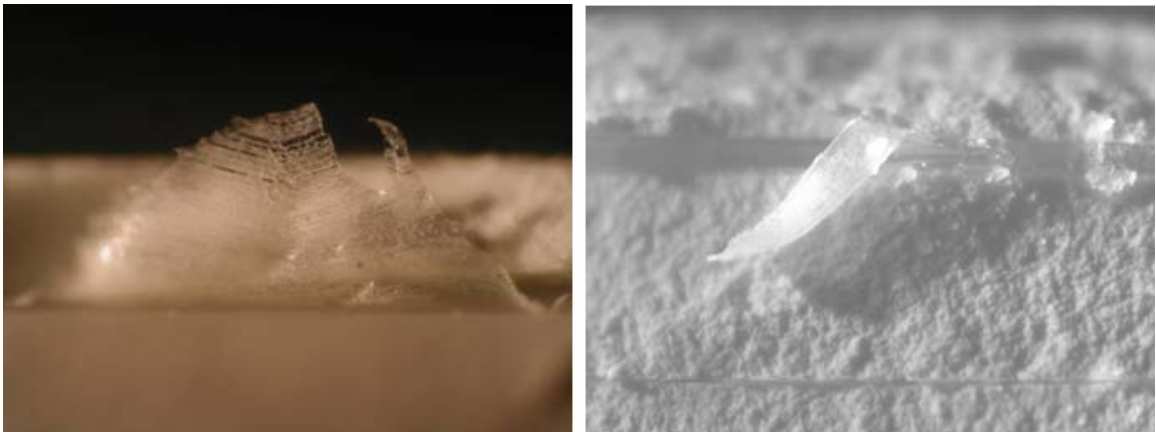


Figure 5.43 Optical micrographs showing the pullout of the PSu layers during fracture of the laminates.

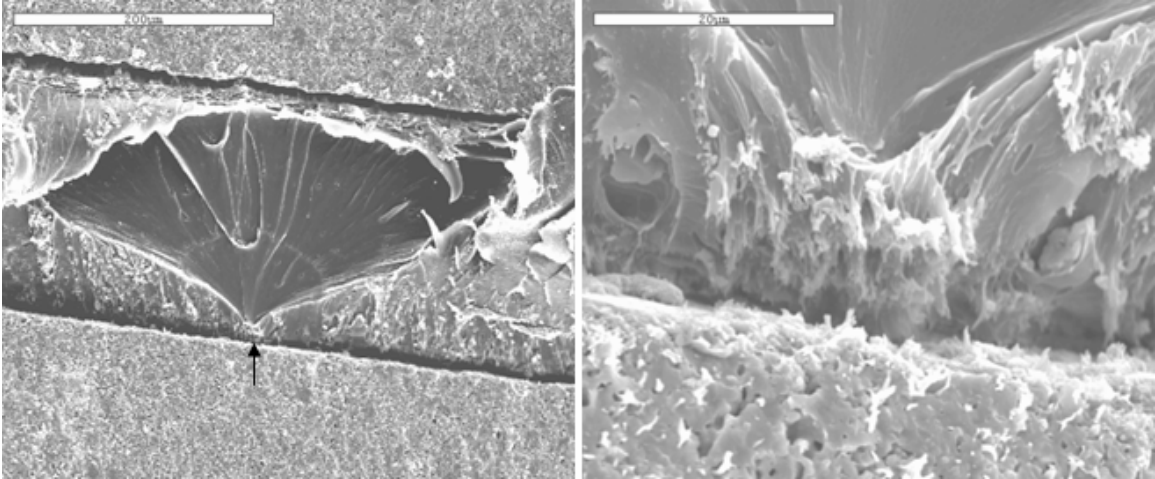


Figure 5.44 SEM images of brittle PSu layer originating from the HA/PSu interface. The arrow indicates the location of the origin.

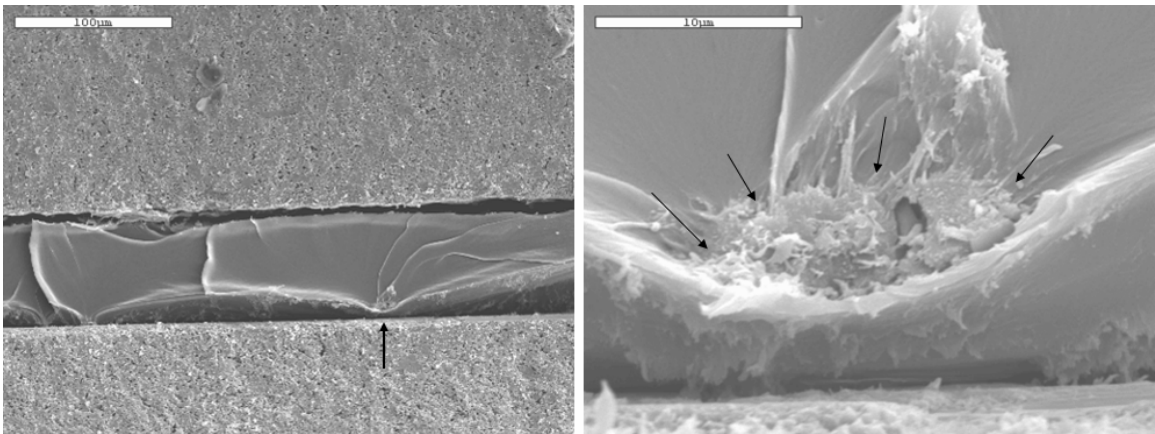


Figure 5.45 SEM images of a PSu layer fracture origin. The location of the origin is indicated by the arrows on both images, failure occurred within the PSu layer and not from the interface.

associated with these flaws are shown in Table 5.11. The predicted failure stress from laminate theory is also shown in Table 5.11.

The failure stress for these laminates was calculated by assuming that the flaws similar to the one shown in Figure 5.34 were only HA, just as with the middle layer failure calculation for the 400-200-800 laminates discussed in the last section. The predicted failure stresses were calculated by multiplying the experimental failure loads by the stress/N values given by the laminate theory for each of the laminate geometries.

Lesser agreement exists between the predicted and measured stress for the laminates with outer HA layers  $< 400 \mu\text{m}$  than for the 400-200-800 laminates. The lack of agreement is the result of the PSu that is present within the flaws of the thinner HA layer laminates. As was shown for the 400-200-800 laminates, PSu has the ability to bridge cracks and interfaces within the laminate system. A phenomenon similar to this is occurring within the initial flaws of the thinner outer HA laminates. The PSu layer bridges the critical flaw effectively increasing the toughness of the material around the flaw. For the same flaw size, an increased toughness results in a greater failure stress according to the fracture mechanics (See Equation 2.12). This toughening mechanism is similar to crack-tip shielding [50] which has been shown to increase the toughness through the deposition of thin films onto indented surfaces prior mechanical testing.

Further evidence of the toughening around the initial flaw is the increased discrepancy between the compared failure stresses in Table 5.11 for the 100-200-800, and the 100-200-1400 laminates. The greater discrepancy for these two laminate groups arises from their having the greatest ratio of PSu layer thickness to outer HA thickness. A 2:1 ratio for these laminates means a greater amount of PSu in the damaged area

compared with the two other laminate groups in Table 5.11 that have a 1:1 ratio of PSu to outer HA thickness. An increased amount of PSu results in a greater toughening effect from PSu bridging, and correspondingly greater than expected failure loads.

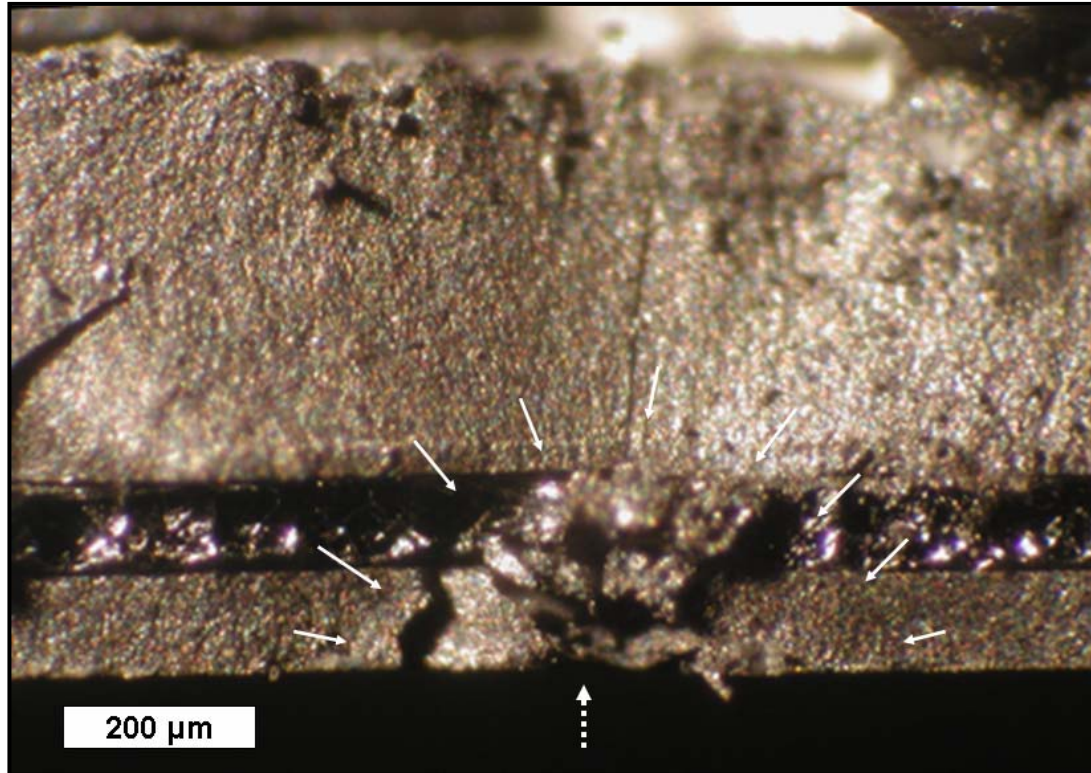


Figure 5.46 Optical micrograph of the fracture origin (solid white arrows) of a 100-100-1600 laminate, the large damaged area is caused by the indent (dashed arrow)

Table 5.11 Failure stress calculations for laminates with outer HA layers < 400  $\mu\text{m}$

Laminate Geometry	n	Experimental Failure Load (N)	Flaw Size ( $\mu\text{m}$ )	Middle Failure Stress, FS (MPa)	Middle Failure Stress, LT (MPa)
100-200-800	1	77	314	27	44
200-200-800	3	112 $\pm$ 18	178 $\pm$ 30	36 $\pm$ 3	39 $\pm$ 6
100-200-1400	2	131 $\pm$ 28	190 $\pm$ 4	35 $\pm$ 0	47 $\pm$ 11
100-100-1600	6	107 $\pm$ 19	289 $\pm$ 81	29 $\pm$ 4	35 $\pm$ 6

FS = calculation from a measurement of flaw size; LT = Laminate Theory

## CHAPTER 6 CONCLUSIONS

### **Primary Conclusion**

The primary goal of this project was to demonstrate that two biocompatible materials, a brittle hydroxyapatite (HA) and a ductile polysulfone (PSu), could be combined into a composite structure with strength and toughness values similar to bone. In order to achieve this goal a novel combination of processing techniques was developed to produce HA/PSu laminate structures. Laminates were shown to have strength values that are 400% greater, and apparent fracture toughness values 1100% greater, than monolithic HA. In Chapter 1, a graph developed by Suchanek and Yoshimura[6] showed the available biomaterials for bone replacement, Figure 1.1. The apparent fracture toughness and composite moduli for each laminate group designed and tested are shown in comparison to bone and other HA composites in Figure 6.1. The data points plotted for the HA/PSu laminates represent the average of the upper and lower bounds of the rule of mixtures. The box represents the range of values covered by the upper and lower bounds of the rule of mixtures. The strength, toughness, and modulus of the laminates fabricated here are closer to the properties of bone than any known composites.

The apparent fracture toughness and elastic modulus of the HA/PSu laminates are greater than the values for existing HA/polymer composites. Apparent fracture toughness of the HA/PSu laminates are within the same range as the HA-based ceramic composites. However, the composite moduli are much more comparable to bone than the all ceramic composites. The net result is an improvement over both types of existing composite

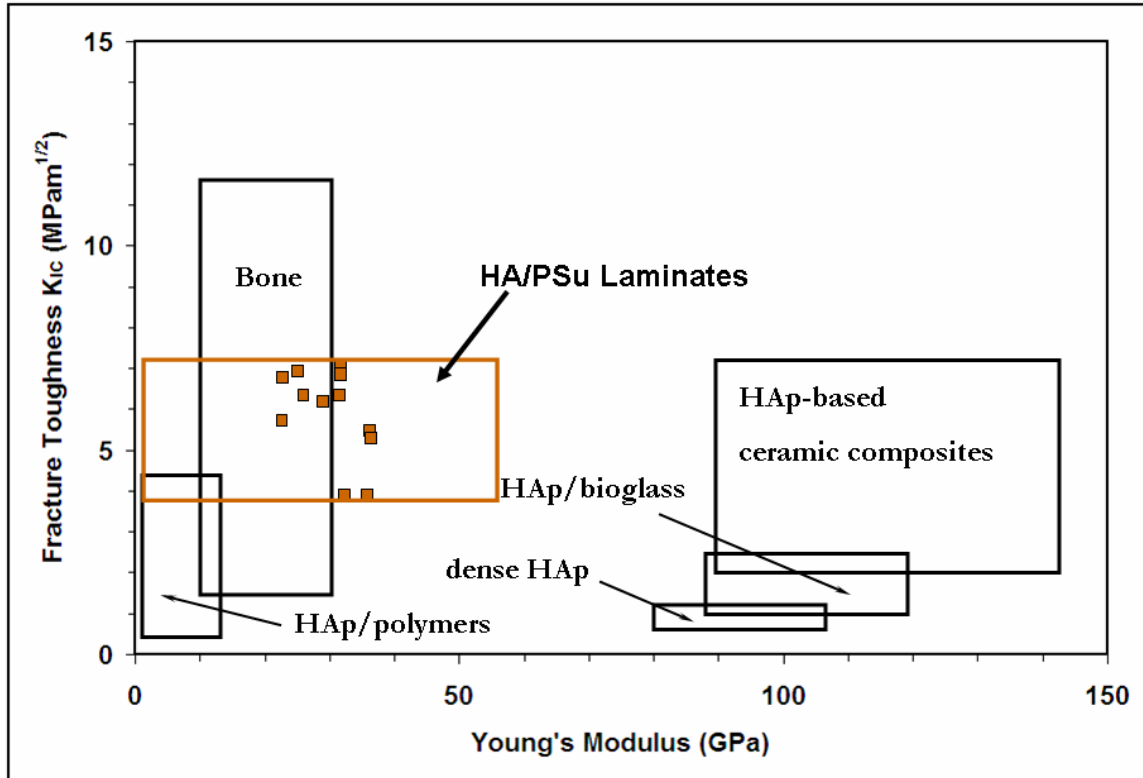


Figure 6.1 Addition of the HA/PSu laminates designed in this study to the graph of available biomaterials for bone replacement developed by Suchanek and Yoshimura [6].

biomaterials. However, the HA/PSu laminate geometries tested in this study still do not cover the entire range reported for bone. Thus, further refinement of the laminate structure is necessary for the HA/PSu laminates to be fully compliant with the full range of elastic modulus and fracture toughness of bone. Future work should focus on fabricating laminates with even thicker PSu layers than the 400  $\mu\text{m}$  tested in this study. It has been shown that the toughness of the laminates increases with increased PSu layer thickness. The resulting HA/PSu laminates would have strength and toughness values covering the entire range of bone.

### Secondary Conclusions

A number of beneficial results were gained through the course of achieving the

primary goal of this project. Porous hydroxyapatite specimens were fabricated through a tape casting process that involved formation of slurries through a one-step addition of constituents instead of a more traditional multi-step approach. The starting hydroxyapatite starting powder having an XRD spectrum, Figure 2.7, showing the presence of secondary calcium phosphate phases was transformed into hydroxyapatite with an XRD spectrum that is identical to naturally occurring hydroxyapatite except for one small CaO peak, Figure 2.13. The sintered hydroxyapatite contained 30% porosity and had strength and fracture toughness values consistent with hydroxyapatite prepared through methods that are more complex.

Monolithic HA and PSu were formed into laminate composites through one of three lamination methods developed specifically for this study. Each of the three methods (matching halves, bottom up, and pre-fabricated PSu layer) involved solvent casting, stacking, and drying with all three methods successfully producing laminates. The benefits and limitations associated with each method were examined, and it was determined that for PSu layers  $\leq 200 \mu\text{m}$  the bottom up method works best, and for PSu layers  $> 200$ , the pre-fabricated PSu layer method works best. It was also demonstrated that the strength and toughness of the PSu layers are independent of retained solvent content and drying temperature. This fact allowed for drying of solvent cast PSu films at  $70^\circ\text{C}$ , and created a more time efficient lamination process. Surface finish of the HA discs prior to casting was shown to reduce the strength of the laminates, Figure 3.22. Since bonding between the PSu and HA occurs through a mechanical interlocking, finer polishing of the HA discs prior to lamination reduces the amount of surface area available for the interlocking to take place. The result was delamination along the interface to the

extent that the mechanical stability of the laminates was compromised, and failure occurs at a lower load.

A mathematical model was developed to describe the stress distributions that results when applying load to the HA/PSu laminates. This laminate theory model was derived by combining existing laminate beam theory using bending moments for simply supported circular plates. The validity of the theory was confirmed through a comparison with finite element analysis of the HA/PSu laminates. A comparison, Table 4.3, showed agreement of the two models to within 3%. This agreement validated the use of the laminate theory model to calculate stress distributions from experimental loads. The laminate theory model was used to predict which laminate geometry with a total thickness of 2.0 mm would produce the greatest failure loads in biaxial flexure tests, Figure 4.9. Design optimization led to the fabrication and testing of laminates with a 350-400-500 geometry. A comparison of the failure loads of the 350-400-500 laminate geometry versus other laminates having the same 2.0 mm total thickness, Figure 5.18, showed that the 350-400-500 geometry did indeed have the greatest experimental failure loads. Thus, the laminate theory can be used for predicting failure strengths for different laminate geometries.

The failure mechanisms of the laminates were characterized to gain a better understanding of the toughening mechanism. Initial testing of 400-200-800 laminates showed a drastic improvement of strength and toughness over monolithic HA, Figures 5.1 – 5.2. In order to identify the design parameters that most influenced laminate behavior, laminates were tested with flaw sizes both smaller and larger than the thickness of the outer HA layer. When the initial flaw size is smaller than the outer HA layer,

crack propagation was shown to begin at the tensile surface of the outer HA layer, cracks propagation is arrested at the HA/PSu interface, and then reinitiated into the middle HA layer. The critical flaw size of the middle HA layer is what ultimately determines the failure strength of the laminate. Middle HA layers have a fracture toughness equivalent to that of monolithic HA, and therefore they fail at approximately the same stress assuming similar flaw sizes. However, the presence of the PSu layers shields the tensile surface of the middle HA layer for direct loading. Thus, greater failure loads are seen for the laminates even though the middle HA layer and the monolithic HA specimens fail at approximately the same stress. Flaw sizes and middle layer failure stresses were determined using fractography, and compared to the failure stress of the middle HA layer predicted by the laminate theory solution, Table 5.10.

When the initial indentation flaws are larger than the thickness of the outer HA layer the result is a bridging of the critical flaw by the PSu layer and a greater fracture toughness of the area around the critical flaw. Instead of crack propagation starting at the outer HA layer, arresting at the interface, and reinitiating into the middle HA, the entire damage area formed through indentation acts as the initial flaw. Failure of the entire laminate occurs once the stress reaches a magnitude sufficient to propagate a crack for the initial flaw despite the additional toughness gained from PSu bridging. The result of this toughening mechanism was the greatest failure stresses calculated for any of the laminates tested in this study, Figure 5.13. The real benefit of this mechanism was shown through a comparison of failure loads for laminates with thin outer HA layers to monolithic HA, Figure 5.12. The 100-200-800 laminate, which has a total thickness of 1.4 mm, failed at loads that were 200% greater than monoliths of a comparable thickness,

and 60% greater than monoliths that were 2.0 mm thick. These results show that a thinner laminate has greater load bearing ability than a thicker monolithic specimen. Thus, less material could be used to fulfill the same load-bearing requirements.

## LIST OF REFERENCES

1. Hench L., Bioceramics: From Concept to Clinic. *Journal of the American Ceramic Society* 74 [7]: 1487-1510 (1991)
2. Hench L., Bioceramics. *Journal of the American Ceramic Society*, 81(7): 1705-1728 (1998)
3. Hench L., Wilson J., *An Introduction to Bioceramics*. Advanced Series in Ceramics. Vol. 1. 1993, Singapore: World Scientific.
4. Wang M., Porter D., Bonfield W., Processing, characterization, and evaluation of hydroxyapatite reinforced polyethylene composites. *British Ceramic Transactions*, 93: 91-95 (1994)
5. Rho J., Kuhn-Spearing L., Zioupos P., Mechanical properties and hierarchical structure of bone. *Medical Engineering and Physics*, 20: 92-102 (1998)
6. Suchanek W., Yashimura M., Processing and properties of hydroxyapatite-based biomaterials for use as hard tissue replacement implants. *Journal of Materials Research*, 13 [1]: 94-117 (1998)
7. Doremus R.H., *Review: Bioceramics*. *Journal of Materials Science*, 27: 285-297 (1992)
8. Ratner B.D, Hoffman A.S., Schoen F.J., Lemons J.E., *Biomaterials Science: An introduction to Materials in Medicine*. 2nd ed. 2004, San Diego: Elsevier Academic Press.
9. Wang M., Developing bioactive composite materials for tissue replacement. *Biomaterials*, 24: 2133-2151 (2003)
10. Puajindanetr S., Best S.M., Bonfield W., Characterization and sintering of precipitated hydroxyapatite. *British Ceramic Transactions*, 93 [3]: 96-99 (1993)
11. Verbeeck R.M.H., deMaeyer E.A.P., Driessens F.C.M., Stoichiometry of potassium-containing and carbonate-containing apatites synthesized by solid-state reactions. *Inorganic Chemistry*, 34 [8]: 2084 (1995)
12. Carotenuto G., Spangnuolo G., Ambrosio L., Nicolais L., Macroporous hydroxyapatite as alloplastic materials for dental applications. *Journal of Materials Science: Materials in Medicine*, 10: 671-676 (1999)

13. Ruys A.J., Wei M., Sorrell C.C., Dickson M.R., Brandwood A., Milthorpe B.K., Sintering effects on the strength of hydroxyapatite. *Biomaterials*, 16: 409-415 (1995)
14. Knowles J.C., Talal S., Santos J.D., Sintering effects in a glass reinforced hydroxyapatite. *Biomaterials*, 17: 1437-1442 (1996)
15. Suchanek W., Yashimura M., Kakihana M., Yoshimura M., Processing and mechanical properties of hydroxyapatite reinforced with hydroxyapatite whiskers. *Biomaterials*, 17: 1715-1723 (1996)
16. Tanner K., Downes R., Bonfield W., Clinical applications of hydroxyapatite reinforced materials. *British Ceramic Transactions*: 93 [3]: 104-107 (1994)
17. Wang M., Bonfield W., Chemically coupled hydroxyapatite-polyethylene composite: structure and properties. *Biomaterials*, 22: 1311-1320 (2001)
18. Wang M., Joseph R., Bonfield W., Hydroxyapatite-polyethylene composites for bone substitution: effects of ceramic particle size and morphology. *Biomaterials*, 19: 2357-2366 (1998)
19. Kamat S.K., Ballarini R., Heuer A., Structural basis for the fracture toughness of the shell of the conch *Strombus gigas*. *Nature*, 405: 1036-1040 (2000)
20. Vincent J., *Structural Biomaterials*. Revised ed. 1990, Princeton, NJ: Princeton University Press.
21. Zhou B.L., Some progress in the biomimetic study of composite materials. *Materials Chemistry and Physics*, 45: 114-119 (1996)
22. Clupper D.C., *Tape Cast Bioactive Metal-Ceramic Laminates For Structural Application*, in *Materials Science and Engineering*. Ph.D. Dissertation, University of Florida (1999)
23. Hwu K.I., Derby B., Fracture of Metal/Ceramic Laminates-II. Crack Growth Resistance and Toughness. *Acta Materialia*, 47 [2]: 545-563 (1999)
24. Chen Z., Mecholsky Jr. J.J., Toughening by Metallic Lamina in Nickel/Alumina Composites. *Journal of the American Ceramic Society*, 76 [5]: 1258-1264 (1993)
25. Chen Z., Mecholsky Jr. J.J., Control of strength and toughness of ceramic/metal laminates using interface design. *Journal of Materials Research*, 8 [9]: 2362-2369 (1993)

26. Yun N.G., Won Y.G., Kim S.C., Toughening of carbon fiber/epoxy composite by inserting polysulfone film to form morphology spectrum. *Polymer*, 45: 6953-6958 (2004)
27. Marcolongo M., Ducheyne P., Garino J., Schepers E., Bioactive glass fiber/polymeric composites bond to bone tissue. *Journal of Biomedical Materials Research*, 39: 161-170 (1998)
28. Wijmans J.G., Baaij J.P.B., Smolders C.A., The mechanism of formation of microporous or skinned membranes produced by immersion precipitation. *Journal of Membrane Science*, 14: 263-274 (1983)
29. Arita I.H., Wilkinson D.S., Mondragon M.A., Castano V.M., Chemistry and sintering behavior of thin hydroxyapatite ceramics with controlled porosity. *Biomaterials*, 16: 403-408 (1995)
30. Hoepfner T.P., Case E.D., The influence of the microstructure on the hardness of sintered hydroxyapatite. *Ceramics International*, 29: 699-706 (2003)
31. Ramay H.R., Zhang M., Preparation of porous hydroxyapatite scaffolds by combination of the gel-casting and polymer sponge methods. *Biomaterials*, 24: 3293-3302 (2003)
32. Murtagh M., Graham E., Pantano C., Elastic Moduli of Silica Gels Prepared with Tetraethoxysilane. *Journal of the American Ceramic Society*, 69 [11]: 775-779 (1986)
33. ASTM C1327, Standard Test Method for Vickers Indentation Hardness of Advanced Ceramics. *ASTM C1327-99*: 480-487 (1999)
34. Wachtman J.B., Capps W., Mandel J., Biaxial Flexure Tests of Ceramic Substrates. *Journal of Materials*, 7 [2]: 188-194 (1972)
35. Callister, W.D., *Materials Science and Engineering An Introduction*. 5th ed. 2000, New York: John Wiley & Sons, Inc.
36. Karger-Kocsis J., Barany T., Moskala E.J., Plane stress fracture toughness of physically aged plasticized PETG as assessed by the essential work of fracture (EWF) method. *Polymer*, 44: 5691-5699 (2003)
37. Aksel C., Warren P.D., Work of fracture and fracture surface energy of magnesia-spinel composites. *Composites Science and Technology*, 63: 1433-1440 (2003)
38. Lawn B., *Fracture of Brittle Solids*. 2nd ed. Cambridge Solid State Science Series. 1993, Cambridge: Cambridge University Press.

39. Chantikul P., Anstis G.R., Lawn B.R., Marshall D.B., A Critical Evaluation of Indentation Techniques for Measuring Fracture Toughness: II, Strength Method. *Journal of the American Ceramic Society*, 64 [9]: 539-543 (1981)
40. Anstis G.R., Chantikul P., Lawn B.R., Marshall D.B., A Critical Evaluation of Indentation Techniques for Measuring Fracture Toughness: I, Direct Crack Measurements. *Journal of the American Ceramic Society*, 64 [9]: 533-538 (1981)
41. Muralithran G., Ramesh S., The effects of sintering temperature on the properties of hydroxyapatite. *Ceramics International*, 26: 221-230 (2000)
42. Case E.D., Smith I.O., Baumann M.J., Microcracking and porosity in calcium phosphates and the implications for bone tissue engineering. *Materials Science and Engineering A-Structural Materials Properties Microstructure and Processing*, 390 [1-2]: 246-254 (2005)
43. Thangamani N., Chinnakali K., Gnanam F.D., The effect of powder processing on densification, microstructure and mechanical properties of hydroxyapatite. *Ceramics International*, 28: 355-362 (2002)
44. Allcock H.R, Lampe F.W., *Contemporary Polymer Chemistry*. 1990, Englewood Cliffs, New Jersey: Prentice-Hall Inc.
45. Fan C.F., Hsu S.L., Application of the Molecular Simulation Technique to Generate the Structure of an Aromatic Polysulfone System. *Macromolecules*, 24: 6244-6249 (1991)
46. Bennison S.J., Jagota A., Smith C.A., Fracture of Glass/Poly(vinyl butyral) (Butacite(R)) Laminate is Biaxial Flexure. *Journal of the American Ceramic Society*, 82 [7]: 1761-1770 (1999)
47. Wu H., Yan X., Interlaminar stress modeling of composite laminates with finite element method. *Journal of Reinforced Plastics and Composites*, 24 [3]: 235-258 (2005)
48. Mallick P.K., *Fiber-Reinforced Composites: Materials, Manufacturing, and Design*. 2nd ed. 1993, New York: Marcel Dekker, Inc.
49. Timoshenko S., Woinowsky-Krieger S., *Theory of Plates and Shells*. 2nd ed. 1959, London: McGraw-Hill, Inc.
50. Gruninger M., L.B., Farabaugh E., Wachtman Jr. J., Measurement of Residual Stress in Coatings on Brittle Substrates by Indentation Fracture. *Journal of the American Ceramic Society*, 70 [5]: 344-348 (1987)

51. Ivanova T.I., Frank-Kamenetskaya O.V., Kol'tsov A.B., Ugolkov V.L. "Crystal Structure of Calcium-Deficient Carbonated Hydroxyapatite Thermal Decomposition." *Journal of Solid State Chemistry*, 160: 340-349 (2001)
52. Wenz L.M., Merritt K., Brown S.A., Moet A., Steffee A.D., In vitro biocompatibility of polyetherketone and polysulfone composites. *Journal of Biomedical Materials Research*, 24 [2], 207-215 (1990)
53. Mecholsky J.J., Gonzales A.C., Frieman S.W., Fractographic analysis of delayed failure in soda lime glass, *Journal of the American Ceramic Society*, 62 [11-12]: 577-580 (1979)
54. Sperling L.H., *Introduction to Physical Polymer Science*, 3rd ed. 2001, New York: John Wiley & Sons, Inc.

## BIOGRAPHICAL SKETCH

Prior to entering graduate school at the University of Florida, Clifford A Wilson II did his undergraduate studies at the College of William and Mary in Williamsburg, VA, earning a bachelor's degree in chemistry from the in 2000. While at William and Mary he was letter winner for the Tribe baseball team.

After graduation, he decided to further his education and began graduate studies at the University of Florida. He joined the research group of Dr. John Echolike Jr. Cliff was inducted into Keramos, the ceramic honor society, during the spring semester 2002. In May of 2003, Cliff received a Master of Science degree in Materials Science and Engineering. Cliff was awarded the Robert C. Pittman Fellowship in August 2003. Cliff successfully defended his doctoral dissertation on June 23, 2005, and received his doctorate during commencement ceremonies in August 2005.

Cliff is married to Leslie Hoipkemeier Wilson, who also received her doctorate in August 2005.